

LOW-EMITTANCE TUNING AT CESR TA

A Dissertation

Presented to the Faculty of the Graduate School
of Cornell University

in Partial Fulfillment of the Requirements for the Degree of
Doctor of Philosophy

by

James Shanks

August 2013

© 2013 James Shanks
ALL RIGHTS RESERVED

LOW-EMITTANCE TUNING AT CESRTA

James Shanks, Ph.D.

Cornell University 2013

The International Linear Collider (ILC) is a proposed 500GeV center-of-mass electron/positron collider. In order to meet luminosity requirements, low-emittance beams must be provided at the start of the two 15-km main linacs. These low-emittance beams will be provided by damping rings, whose optics must be well-corrected in order to minimize dilution of the vertical emittance.

In 2008 the Cornell Electron/Positron Storage Ring (CESR) was reconfigured from an electron/positron collider to the CESR Test Accelerator (CesrTA), to serve as a testbed for the ILC damping rings. One of the primary research objectives of the CesrTA project is to explore beam-based optics correction techniques for application at the ILC damping rings. The geometric vertical emittance target for CesrTA is < 10 pm at 2.085 GeV.

This dissertation discusses the tuning methods used at CesrTA to achieve low-emittance conditions. Simulations modeling the effects of magnet misalignments, systematic and random multipoles, BPM errors, and emittance correction algorithm have been developed, and suggest the residual vertical emittance measured at the conclusion of the tuning procedure is dominated by sources unaffected by optics correction. The same characterization methods leading to this diagnosis have been applied to the proposed International Linear Collider (ILC) damping rings to evaluate misalignment and multipole tolerances. Dynamic aperture studies for the ILC damping rings are discussed.

BIOGRAPHICAL SKETCH

James Patrick Shanks was born December 2, 1984 in Hartford, CT to Kurt and Penny Shanks, joining brother Jonathon. Shortly after, they moved to Rochester, MI, where he attended school through second grade. In third grade the family relocated to Clarkston, MI, where they stayed for the remainder of Jim's grade school education. He graduated from Clarkston High School in 2003.

In the fall of 2003 he attended Michigan State University to study physics and mathematics. It was also during his undergraduate career that Jim was first exposed to accelerator physics, through a summer Research Experience for Undergraduates (REU) program at Cornell University in 2006 under Mark Palmer. Jim graduated from Michigan State with a B.S. in Honors Physics and Mathematics in 2007. He began work at Cornell University in accelerator physics that summer under the guidance of David Rubin, working on beam-based correction techniques for CEsrTA.

Jim completed his Ph.D. in the summer of 2013.

*My woman-soldier, gallant Kate,
As pure and true as blades of steel*

-Alfred, Lord Tennyson

To my gallant Kate.

ACKNOWLEDGEMENTS

So many people have influenced my journey, it's difficult to know where to begin.

First and foremost, I wish to thank my parents for their love, support, and encouragement. Between my mother, heavily involved in the PTA and who insisted we have "educational summers" rather than rotting our brains in front of the TV, and my father, who helped to shape the school district throughout my time in grade school, it was inevitable that the importance of education would be instilled in me. It is interesting to observe that, when my father handed me my high school diploma as I crossed the stage, I was barely half-way through my formal education.

My brother, Jon, has always had a passion for science and knowledge which has inspired my own. Although we've had our moments, he has been and continues to be a role model.

I would also like to thank my grandparents, who have never stopped believing in me. During the first few years of grad school when I felt like throwing in the towel, I would remember their unwavering support, and push on.

Many teachers throughout my education share some responsibility for my choice to pursue a doctorate. Don Gilmore and Ned Burdick taught my first courses in physics, and their passion for teaching influenced my trajectory into college. At Michigan State, Joey Huston and Wayne Repko, among many others, provided much support and encouragement.

I would never have come to Cornell for graduate school if it weren't for Mark Palmer's mentorship during my REU project at Cornell in 2006. I thank him for his dedication and passion in guiding the first four years of the CesrTA project. From him I have learned many things, in physics, leadership, and project man-

agement.

I would not be the person I am today without my friends. Mike Youngs deserves special recognition, for he has had more influence on me than almost anyone not directly related to me, and for that he should at least be acknowledged. I would never have understood physics nearly as well if it weren't for his complimentary intuition. Thanks also goes to the rest of the MSU Physics graduates of 2007, I have rarely encountered such a tight-knit group of bright, dedicated individuals. I would also like to thank my good friends Laura Boon and Kent Wootton, who have provided support and suggestions over the years since the Linear Collider school in 2010.

At Cornell, Joe Calvey, Mike Ehrlichman, Colwyn Gulliford and I all started the accelerator physics program at the same time, and now it looks like we will all finish within four months of each other. I would like to thank them all for their continual support, conversation, entertainment, and banter over the past six years. Thanks also goes to my officemates and fellow graduate students Kelvin Blaser, Steven Full, Siddharth Karkare, Hyeri Lee, and Jared Maxson, and to Suntao Wang, Avi Chatterjee, and Walter Hartung, for bouncing ideas and providing necessary distractions.

There are too many people in Wilson Lab who have helped me over the years to thank them all individually. Thanks to David Sagan for his patience in enduring far too many user errors, in addition to his dedication to squashing bugs in `Bmad`. Without his support my simulation code would have amounted to nothing.

Mike Billing has been an indispensable resource for all things CESR, and has helped guide my intuition for accelerator operations. His ability to see the bigger picture is something I continue to strive for.

Thanks to Jim Sexton and to all of the operators for providing a well-surveyed machine, well-tuned linac and synch beam, innumerable replaced choppers, controllers, and interface cards, and for countless hours of entertaining conversation.

Nate Rider and Dan Peterson have put in far too many hours in order to provide functioning x-ray beam size monitors, and their efforts do not go unnoticed. I also thank Brian Heltsley for his help in interpreting the xBSM results. I had no idea a pinhole camera could be so complicated.

Thanks to John Barley, Laurel Bartnick, Jerry Codner, Mike Forster, Dave Kreinick, Don Hartill, Yulin Li, Bob Meller, Stu Peck, Matt Rendina, Dave Rice, John Sikora, Kiran Sonnad, Matthew Stedinger, Charlie Strohman, and Peter Quigley for making the CEsrTA project a success.

The CEsrTA project owes much of its success to its collaborators. In particular, I would like to thank John Flanagan, Yannis Papaphilippou, and Andy Wolski for their support, input, and suggestions.

Of course, my project would have gone nowhere without the guidance of my advisor, Dave Rubin. His support and encouragement have been indispensable over the past six years, and it has been a pleasure working under his supervision.

Finally, I would like to thank Kate for her patience and understanding when I had to pull 25-hour shifts during the CEsrTA runs, disappear for three weeks at a time for conferences and schools, and work late into the night while writing. My achievements would not have been possible without her love and support.

This research was funded by the National Science Foundation (NSF) and the Department of Energy (DOE).

TABLE OF CONTENTS

Biographical Sketch	iii
Dedication	iv
Acknowledgements	v
Table of Contents	viii
List of Tables	xii
List of Figures	xiii
1 Introduction	1
1.1 Outline	3
1.2 Motivation for Low-Emittance Tuning	4
1.2.1 Storage Ring Light Sources	5
1.2.2 Circular Colliders	6
1.2.3 Damping Rings for Linear Colliders	8
1.2.4 Toward Lower Transverse Emittance	9
1.3 The International Linear Collider	10
1.3.1 Damping Rings for ILC	12
1.4 CesrTA	13
2 The Physics of Electron Storage Rings	15
2.1 Co-Propagating Coordinate System	15
2.2 Magnets in Accelerators	17
2.3 Transverse Beam Motion	20
2.3.1 Drift	22
2.3.2 Dipole	22
2.3.3 Quadrupole	24
2.3.4 One-Turn Matrix	25
2.4 Twiss Parameters and Emittance	25
2.5 Closed Orbit	29
2.6 Energy Dependence: Dispersion and Chromaticity	29
2.7 Coupled Motion	30
2.8 Radiation Integrals	34
2.9 Radiation Damping and Quantum Excitation	35
2.9.1 Damping	35
2.9.2 Excitation	37
2.10 Equilibrium Transverse Emittance	38
2.10.1 Damping Wigglers	40
2.11 Longitudinal Beam Dynamics	41
2.12 Vertical Emittance Dilution from Lattice Errors	43
2.12.1 Orbitry Errors	43
2.12.2 Beta Errors	44
2.12.3 Vertical Dispersion Errors	45
2.12.4 Coupling Errors	46

2.13	Vertical Emittance Dilution from Time-Varying Sources	47
2.13.1	Kick Modulation	48
2.13.2	RF Modulation	48
2.14	Dynamic Aperture	49
3	CesrTA - Overview	50
3.1	CESR Overview	50
3.2	CesrTA Objectives	54
3.3	CesrTA Lattice Design	56
3.4	Survey and Alignment at CesrTA	58
4	Instrumentation	62
4.1	BPM System	62
4.2	Tune Trackers	64
4.2.1	System Overview	65
4.3	X-Ray Beam Size Monitor	66
4.3.1	System Overview	68
4.3.2	Reference Orbit and Source Point	69
5	Measurement Techniques	72
5.1	Closed Orbit	72
5.2	Dispersion	73
5.3	Betatron Phase and Coupling	74
5.4	Turn-by-Turn Data	75
6	Beam Position Monitor Calibrations	76
6.1	Button-by-Button Timing	76
6.2	Button-to-Button Relative Gains	77
6.3	Electronic Centering	78
6.4	Tilt Calibration	79
6.4.1	Method I: In-Phase Coupling	80
6.4.2	Method II: Turn-By-Turn Trajectory Data	81
7	Low-Emittance Tuning Techniques	82
7.1	Response Matrix Analysis (RMA)	83
7.2	Combined Coupling and Dispersion Correction	85
7.3	Calculating Emittance and its Uncertainties	88
7.4	Results of Emittance Tuning at CesrTA	92
7.5	Alternative Emittance Tuning Methods at CesrTA	93
8	Emittance Correction Simulations	94
8.1	ring_ma2	94
8.1.1	Model Lattice with Errors	96
8.1.2	Simulated Measurements	96
8.1.3	BPM Errors	97

8.2	Simulation Results for CesrTA	100
8.3	Discussion of Simulation Results	101
9	Diagnosis of Emittance Dilution	103
9.1	Emittance Dilution from Feedback Modulators	103
9.1.1	Estimate of Effect of Feedback Noise	109
9.2	Remaining Sources of Beam Jitter	111
9.2.1	Energy Dependence	112
9.2.2	Eliminating Time-Varying Elements	115
9.3	Other Candidates for Residual Emittance Dilution	118
9.3.1	Errors Omitted from ring_ma2	118
9.3.2	Sources in CESR	119
9.3.3	Residual Gas Scattering	120
9.3.4	Collective Effects	121
9.4	Toward the Quantum Limit	123
9.5	Conclusions	128
10	ILC Damping Rings	129
10.1	ILC - Overview	129
10.2	DTC04 Lattice	130
10.3	Characterization Method	132
10.3.1	Misalignment and Correction	134
10.3.2	Dynamic Aperture	135
10.4	Error Tolerance of DTC04	136
10.4.1	Nominal Lattice and Errors	137
10.4.2	Reduced BPM Scheme	138
10.4.3	Increased Multipoles	140
10.5	Summary	141
11	Summary and Future Work	143
11.1	Summary	143
11.2	Future Work	144
A	Propagating Tune Tracker Phase	146
B	xBSM Source Point Calculations	148
B.1	Calculation Method	148
B.2	Results - December 2012 xBSM Reference Orbits	149
B.3	Effect of Reference Orbit	150
B.4	Sensitivity to Errors	152
C	Processing of Phase Data	153
D	Effects of BPM Tilt on Betatron Phase and Coupling Measurements	157

E	Errors for ring_ma2 Simulations	162
E.1	CesrTA	162
E.2	ILC Damping Ring	162
F	Energy Dependence of the Vertical Emittance	167
F.1	Energy Dependence of Radiation Integrals in Wigglers	167
F.2	Contributions to the Emittance	171
F.3	Energy Dependence of α_b	172
F.4	“Opening Angle” Term	173
F.5	“Quantum Excitation” Term	174
F.6	“Time-Varying” Terms	175
F.6.1	RF Voltage Jitter	176
F.6.2	Time-Varying Dipole Kick	176
	Bibliography	178

LIST OF TABLES

1.1	Horizontal and vertical emittances achieved at other light sources	10
2.1	Summary of magnet classes	19
3.1	Parameters of the CESR electron/positron storage ring.	51
3.2	Parameters of the CESR damping wigglers	53
3.3	Parameters of the CesrTA lattice.	57
4.1	Magnification for C- and D-lines	71
7.1	Typical levels of correction for CesrTA after emittance tuning. . .	87
7.2	Parameters for uncertainty in ϵ_y at 2.085 GeV	91
7.3	Emittance corrections achieved at CesrTA	91
8.1	Simulated measurements for ideal CesrTA lattice	97
8.2	<code>ring_ma2</code> results for CesrTA lattice	100
9.1	Constants C_i for energy dependence of ϵ_y	114
9.2	Summary of beam stability tests at CesrTA	117
9.3	<code>ring_ma2</code> CesrTA studies toward the ILC-DR emittance	125
9.4	<code>ring_ma2</code> CesrTA studies: reducing BPM errors	126
9.5	<code>ring_ma2</code> CesrTA studies toward the quantum limit	127
10.1	Summary of the DTC04 lattice parameters.	131
10.2	Summary of elements in the DTC04 lattice.	131
B.1	Surveyed locations for C- and D-line xBSMs	148
B.2	xBSM source points and DOF	150
B.3	Magnification for C- and D-lines	150
B.4	C-line magnification with orbitry	150
B.5	D-line magnification with orbitry	152
B.6	D-line - effect of various errors on the magnification	152
E.1	CesrTA misalignments and errors for <code>ring_ma2</code>	163
E.2	CesrTA BPM errors for <code>ring_ma2</code>	164
E.3	Multipoles used in <code>ring_ma2</code> studies of CesrTA lattice	164
E.4	Errors used in ILC-DR studies	165
E.5	ILC-DR multipoles for simulation	166
F.1	Contributions to radiation integrals for CesrTA	169
F.2	Energy dependence of radiation integrals for CesrTA	170

LIST OF FIGURES

2.1	Coordinate system	16
2.2	Physical interpretation of Twiss parameters	27
2.3	Physical interpretation of \bar{C}	33
2.4	Illustration of radiation damping	36
3.1	CesrTA layout	58
3.2	CesrTA optics	59
3.3	CesrTA survey and alignment results	60
3.4	CESR parameters without beam-based corrections at CesrTA	61
4.1	Cross-section of a CESR BPM	63
4.2	Conceptual illustration of the tune trackers used at CESR	66
4.3	Diagram illustrating xBSM setup	69
4.4	xBSM reference orbit for D-line	70
8.1	<code>ring_ma2</code> results for CesrTA	101
9.1	Bunch centroid motion	105
9.2	FFT of bunch centroid motion	106
9.3	TBT vertical beam size	107
9.4	FFT of vertical beam size	108
9.5	Vertical emittance as a function of energy	114
9.6	Vertical emittance as a function of bunch current	123
10.1	Layout of DTC04 lattice.	132
10.2	ILC-DR optics functions	132
10.3	DTC04 arc cell.	133
10.4	<code>ring_ma2</code> results for DTC04, nominal	137
10.5	Dynamic aperture for DTC04, nominal	138
10.6	<code>ring_ma2</code> results for DTC04, reduce BPMs	139
10.7	Dynamic aperture results for DTC04, reduced BPMs	140
10.8	<code>ring_ma2</code> results for DTC04, increased multipoles	141
10.9	Dynamic aperture for DTC04, increased multipoles	142
A.1	Encoding the tune tracker phases with BPM clock	147
B.1	C-line geometry	151
B.2	D-line geometry	151

CHAPTER 1

INTRODUCTION

Emittance is roughly the area of the beam in phase space, and is often used as a measure of beam quality. A low-emittance beam can be focused to have small physical beam size and low divergence. The demand by x-ray scientists and particle physicists for higher-intensity beams have motivated a push for smaller horizontal and vertical emittance.

The horizontal emittance in circular accelerators is a well-defined equilibrium determined primarily by the arrangement and strengths of the guide field magnets (also called the “lattice” or “optics”). For a fixed arrangement of guide field magnets, different magnet strengths will yield different horizontal emittances, while the minimum achievable horizontal emittance depends the exact arrangement of the magnets. By comparison, the vertical emittance is fundamentally limited only by the finite opening angle of radiation emitted by the stored beam, leading to an asymmetry where the lower bound on the vertical emittance is typically 10,000 times smaller than the lower bound of the horizontal emittance. The vertical emittance is therefore significantly more sensitive to errors in the optics. Left uncorrected, magnet misalignments and guide field errors will typically increase or “dilute” the equilibrium vertical emittance by several orders of magnitude. Corrections to the guide field are necessary in order to compensate. This process is referred to as “optics correction,” or “emittance tuning.”

The guide field is characterized by optics functions which determine beam properties throughout the accelerator. The beam’s response to the optics functions can be measured at a fixed location in the ring using four electrode pick-

ups, collectively called a beam position monitor (BPM). Storage rings typically have tens to a few hundred BPMs, semi-uniformly distributed, sampling the motion of the beam position around the ring to infer properties of the stored beam. Corrections to the optics functions are computed by fitting a model of the accelerator to the measured data from all BPMs simultaneously. Corrector magnets are then powered to compensate for lattice errors and thus minimize the vertical emittance.

As will be discussed in Section 1.2, minimization of the vertical emittance has only become of interest to storage rings over the last ten years or so. As such, vertical emittance correction is a relatively new field. Methods have been demonstrated at small- to medium-sized rings to correct the vertical emittance due to misalignments and errors to within a factor of 10 of the fundamental limit. However, data acquisition times for these methods scale linearly with the number of components in the ring, and analysis time scales roughly with the number of components cubed. For large rings which are also densely populated with BPMs and guide field magnets, such as the 3.2 km damping rings for the proposed International Linear Collider (ILC) [1], this becomes impractical and new methods must be developed.

In 2008 the Cornell Electron/Positron Storage Ring (CESR) was reconfigured from an electron/positron collider to the CESR Test Accelerator (CesrTA) [2–5], a testbed for the ILC damping rings. One of the primary goals of the CesrTA project is to demonstrate the efficacy of optics correction techniques which scale well to larger rings, in order to achieve near-ILC-specification beam conditions. This dissertation will detail the experimental and simulation efforts at CesrTA for vertical emittance correction.

A method for fast optics measurement and correction has been developed for CEsrTA, based on turn-by-turn BPM measurements while resonantly exciting the beam. This method is extremely fast, on the order of 15 minutes for a full correction, compared to the most common methods which may take several hours on a small- to medium-sized ring, and is now in regular use during CEsrTA operations.

To better understand the effectiveness of the emittance correction methods developed at CEsrTA, a software package has been developed to simulate the full measurement and correction procedure. The simulation includes magnet misalignments and manufacturing tolerances, beam detector measurement errors, and correction method. Among other things, results from the simulation have led to the conclusion that the vertical emittance at CEsrTA is dominated by sources which are unaffected by optics correction.

The agreement between the measured and simulated optics functions for the CEsrTA lattice demonstrates that the model is accurate. The characterization method is therefore not limited to existing lattices, and has also been applied to the ILC damping rings lattice to predict the efficacy of corrections on a ring which is not yet built.

1.1 Outline

Motivation for emittance tuning will be developed in the remainder of Chapter 1. Chapter 2 will then discuss the analytic formalism of electron/positron storage rings necessary to understand how misalignments and errors affect the vertical emittance.

Chapter 3 will cover the requirements and optics design for the CesrTA lattice, and demonstrate the necessity for a beam-based optics correction technique. Chapters 4-6 elaborate on the instrumentation required at CesrTA for beam-based measurements relevant to emittance tuning, and the specific types of optics measurements used.

Chapter 7 will describe how to combine these optics measurements into the emittance correction algorithm developed for CesrTA, and the effectiveness of that tuning procedure. The simulation method used to diagnose limitations to the correction methodology and its results for the CesrTA lattice are described in Chapter 8. Chapter 9 will tie together what was developed in Chapters 7-8 to demonstrate how the simulations of emittance correction led to the discovery of sources of emittance dilution other than static misalignments and optical errors.

In Chapter 10, the simulation methods are applied to the International Linear Collider damping rings. A characterization of the dynamic aperture with multipoles and full wiggler nonlinearities is also presented. These simulations provide a basis on which the damping ring lattice can be evaluated for the likelihood of achieving the vertical emittance required by the ILC.

Finally, a summary and suggestions for future work are presented in Chapter 11.

1.2 Motivation for Low-Emittance Tuning

In a storage ring, the equilibrium distribution of particles is Gaussian. The phase space in each dimension (horizontal, vertical, and longitudinal) is described as

an ellipse:

$$\gamma_u u^2 + 2\alpha_u u u' + \beta_u u'^2 = \pi\epsilon_u \quad (1.1)$$

where $u = x, y, \text{ or } z$, and $\gamma_u, \alpha_u, \beta_u$ are optics functions determined by the guide field magnets and accelerating structures, as will be discussed in Chapter 2. The phase space ellipse has area $\pi\epsilon_u$, where ϵ_u is the emittance. The beam size and spread in momenta of a beam are both proportional to $\sqrt{\epsilon}$.

Storage rings are most widely used for three purposes: as a light source, a circular collider, or a damping ring for a linear collider. In all three scenarios, users demand a small beam size and small spread in transverse momentum. In other words, users demand small transverse emittance (horizontal and vertical), though in each of the three scenarios the motivation is different.

1.2.1 Storage Ring Light Sources

When a charged particle travels through a transversely-deflecting magnetic field it emits synchrotron radiation. This radiation can be harnessed at beam lines where users expose samples for various forms of imaging. Storage rings built explicitly for this use are called light sources.

Light source users are interested in increasing the brightness, defined as

$$\mathcal{B} = \frac{\text{Flux}}{4\pi^2 \Sigma_H \Sigma_V \Sigma_{H'} \Sigma_{V'}} \quad (1.2)$$

where $\Sigma_u = \sqrt{\sigma_u^2 + \sigma_\gamma^2}$ and $\Sigma_{u'} = \sqrt{\sigma_{u'}^2 + \sigma_{\gamma'}^2}$ are the source size and divergence, respectively, accounting for both the bunch ($\sigma_u, \sigma_{u'}$, for $u = H, V$) and the phase space occupied by radiated photons ($\sigma_\gamma, \sigma_{\gamma'}$). The brightness is therefore inversely proportional to the product of horizontal and vertical beam emittance.

It is only within the last ten years that light sources have begun moving toward smaller emittances. From the accelerator operations standpoint, small emittance will increase the number of hard-scattering events within the beam, some of which will change a particle's energy sufficiently to lose the particle (Touschek scattering). This results in an exponential decay of the beam, and variation in the intensity of synchrotron radiation over the duration of user experiments.

Recent developments in user experiments and synchrotron light detectors have enabled new classes of experiments such as microcrystallography [6] which require small beam emittance with constant flux. Light sources have found that by replenishing lost beam in frequent, small injections which have minimal impact on users, the beam current can be kept constant at the 0.5% level for days at a time. In top-up operation a short beam lifetime becomes tolerable, and lower emittance can be accommodated in order to increase brightness and reduce spot size for users.

1.2.2 Circular Colliders

In colliders, the event rate is characterized by the luminosity \mathcal{L} :

$$\mathcal{L} = \frac{N^2 f_c}{4\pi \sigma_x \sigma_y} \quad (1.3)$$

where N is the number of particles per bunch, f_c is the frequency of bunch collisions, and $\sigma_{x,y}$ are the horizontal and vertical beam sizes at the interaction point (IP), respectively, which scale as $\propto \sqrt{\epsilon_{x,y}}$. For circular colliders, \mathcal{L} scales as:

$$\mathcal{L} \propto \left(1 + \frac{\sigma_y}{\sigma_x}\right) \xi_y \quad (1.4)$$

ξ_y is the beam-beam tuneshift, where electromagnetic fields within the beam cause a significant focusing effect on the opposing beam. Smaller beam sizes result in a higher density of particles, and therefore higher luminosity, at the cost of increasing the beam-beam tuneshift. If the tuneshift becomes too large, particles will cross resonances and the emittance will increase, reducing luminosity. Therefore, there is a balance between minimizing the beam size while maintaining the beam-beam tuneshift within acceptable bounds. In practice the beam-beam tuneshift has been the most significant determining factor of the luminosity at nearly every modern storage ring collider.

The beam-beam tuneshift is proportional to $\frac{1}{\sigma_y(\sigma_x + \sigma_y)}$, where $\sigma_i \approx \sqrt{\beta_i \epsilon_i}$ and β_y is the “beam envelope” function representing the focusing at a given point in the machine (discussed in Section 2.4). Near the interaction point, β_y varies along the direction of bunch propagation s as $\beta_y(s) = \frac{s^2}{\beta_y^{min}} + \beta_y^{min}$, where β_y^{min} is located at the center of the interaction point. If β_y^{min} were lowered in an attempt to decrease the beam-beam tuneshift, then β_y along the length of the bunch will rapidly increase, actually worsening the beam-beam tuneshift.

However, if a large crossing angle is introduced between the colliding bunches, then the collisions would only occur within a small distance along s , where β_y^{min} (and therefore the beam-beam tuneshift) can be minimized. The decrease in β_y would also correspond to a decrease in vertical beamsizes, which would then increase the luminosity. The SuperKEKB collider proposal utilizes this method to achieve a predicted increase in luminosity through use of a large crossing angle, strong focusing, and small emittances [7]. The next generation of circular colliders using this method will therefore demand small emittance to achieve their luminosity goals.

1.2.3 Damping Rings for Linear Colliders

In circular electron/positron machines particle motion is cooled through a combination of synchrotron radiation emission in transversely-deflecting magnets and re-acceleration through radio-frequency (RF) cavities. This process of radiation damping will be discussed in more detail in Chapter 2. In a linear accelerator the only transverse deflections are due to misalignments and corrector magnets, and as a consequence there is very little synchrotron radiation, and no damping. The emittance in a linear collider can only increase along its length, therefore the beam must have low emittance prior to acceleration.

It is difficult to produce electron bunches with the requisite charge, low emittance, spin polarization, and repetition rate for a linear collider directly from a source; it is not possible for positrons with present technology. As such, bunches from the electron and positron sources must be cooled before they are transferred to the main linacs for final acceleration and collision. This is accom-

plished by storing the bunches in damping rings, one for each species, prior to transferring to the main linacs. The damping rings accept a large, “hot” bunch from the electron or positron source and rapidly cool the bunch through radiation damping to achieve the emittances required at the entrance to the main linac, with a damping time compatible with the required bunch train repetition rate. As with circular colliders and light sources, the optics in damping rings must be well-corrected in order to achieve low emittance.

1.2.4 Toward Lower Transverse Emittance

It is evident that emittance minimization and preservation are crucial for modern and next-generation storage rings. For both brightness and luminosity, small vertical and horizontal emittance is desirable.

The horizontal emittance is nearly entirely determined by the design optics of a storage ring, whereas the vertical emittance is only limited by the finite opening angle of synchrotron radiation. Typical vertical-to-horizontal emittance ratios in modern light sources are around 0.1-1%, suggesting there is room for improvement in the horizontal emittance. The next generation of storage rings, led by facilities such as MAX-IV [8] and NSLS-II [9], use clever optics design with combined-function magnets, strong focusing magnets, and damping wigglers to reduce the horizontal emittance to below 1 nm. Table 1.1 summarizes the emittances achieved at state-of-the-art modern and near-future light sources.

As will be discussed in Chapter 2, the fundamental limit for vertical emittance is only a function of the finite opening angle of synchrotron radiation, and is typically of order 0.2 pm for most storage rings. Imperfections and misalign-

Storage Ring	Circ. [m]	Energy [GeV]	ϵ_x [nm]	ϵ_y [pm]	Date
APS	1100	7.0	3.1	40	2013 [10]
ASLS	216	3.0	10.4	100 (1.2)	2011 [11, 12]
ESRF	844.4	6	4.0	7.0	2012 [13]
MAX-IV	528	3.0	0.3	< 8.0	2016 [8]
NSLS-II	780	3.0	0.9	8.0	2015 [9]
SLS	288	2.4	5.5	(0.9)	2012 [14]
Cornell ERL	2400	5.0	0.013	10.0	2021 [15]

Table 1.1: Horizontal and vertical operating emittances of current or near-future storage ring-based light sources. Values in parentheses indicate lowest measured vertical emittances at that facility.

ments in guide field magnets will dilute the vertical emittance by several orders of magnitude above this minimum. Through use of beam-based optics characterization, sources of vertical emittance can be identified and independently-powered corrector magnets can be adjusted to compensate. Using this strategy, storage rings have corrected vertical emittance to around 10 pm or less. Typical operating values for vertical emittance are also summarized in Table 1.1. Light sources have recently been at the forefront of developing optics correction techniques. In particular, the Australian Synchrotron Light Source (ASLS) [11] and the Swiss Light Source (SLS) [14] have demonstrated vertical emittance around 1 pm, within an order of magnitude of the fundamental lower limit. The methods used to achieve these emittances will be discussed in Chapter 7.

1.3 The International Linear Collider

In experimental high-energy physics, it is common practice to alternate new proposals between hadron and lepton colliders. Both classes of colliders have advantages and disadvantages, and in the end, both are necessary in the push

for further understanding in particle physics.

There are two primary distinctions between hadron and lepton colliders which demonstrate their complementary natures. The first is that the rest mass for electrons is roughly 1/2000 that of protons. This is important in circular accelerators, where power emitted in the form of synchrotron radiation scales as $(E/mc^2)^4$. For the same total energy and bending radius, protons emit less power per turn than electrons, meaning it is easier to store proton beams at very high energy. For this reason, hadron machines are often referred to as “energy frontier” machines. Synchrotron radiation is also necessary for damping to occur, therefore electron/positron rings have significantly more damping compared to hadron rings, allowing for smaller emittance.

The second distinction is that protons are composite particles, comprised of quarks and gluons, whereas electrons are point particles. When protons collide the interaction is not proton-proton, but rather quark-gluon, quark-quark, or gluon-gluon. The energy of each individual particle inside the protons is only a fraction of the total energy of the proton; furthermore, the opportunity cost for achieving a higher center-of-mass energy is that the exact energy of the interacting particles cannot be known. Electron/positron colliders cannot achieve the same center-of-mass energy as hadron colliders, however unlike hadron colliders the total energy of the particle is available at the time of collision, and that energy can be known to a higher degree of certainty. This has led to electron/positron machines being referred to as “precision measurement” machines.

It is evident that both hadron and lepton machines play a role in understanding particle physics. In keeping with this alternating-proposal model, the

International Linear Collider (ILC) is a proposed electron/positron linear collider [1], intended to compliment the presently-operating Large Hadron Collider (LHC) [16].

The proposed beam energy of the ILC is up to 250GeV/beam (500GeV center-of-mass). As will be discussed in Chapter 10, this is sufficiently high-energy to make a circular collider impractical due to energy loss to radiation. Therefore, the proposal is for two opposing linear accelerators (linacs), each approximately 15 km long.

1.3.1 Damping Rings for ILC

As previously mentioned, there is no radiation damping in linacs, and the emittance can only increase along its length; in order to achieve low emittance at the interaction point, bunches must enter the linac with low emittance. Damping rings are required in order to produce low-emittance beams prior to transfer to the main linac. The vertical emittance in a storage ring is limited by the quality of correction to the optics, mandating a well-characterized, well-corrected damping ring in order to maximize luminosity of the collider.

Details of the ILC damping rings will be discussed in Chapter 10. The design calls for rings 3.2 km in circumference, larger than any presently-operating lepton machine. Many modern beam-based characterization techniques are impractical for such a large machine. New techniques for characterization and correction are therefore necessary in order to achieve the luminosity goals of the ILC.

1.4 CesrTA

The Cornell Electron/positron Storage Ring (CESR) is a 768 m electron/positron ring, with an energy reach of 1.5-5.3 GeV. In 2008, CESR was converted to a Test Accelerator (CesrTA) [2–5]. The purpose of the CesrTA program is to investigate the physics of low emittance beams in storage rings, with specific emphasis on the ILC damping rings. Details of the CesrTA conversion and optics will be discussed in Chapter 3.

The primary research goals of the CesrTA program are:

- To develop and demonstrate the efficacy of low-emittance tuning techniques that routinely yield a vertical emittance below 10 pm.
- To characterize electron cloud induced beam dynamics from bunch interactions with the cloud along a train of bunches in low-emittance conditions.
- To characterize electron cloud mitigation techniques, such as beam chamber coatings, clearing electrodes, and chamber grooving.

This dissertation will detail the efforts on the development of emittance correction methods and the achievement of low-emittance conditions at CesrTA. As will be shown, achieving low-emittance conditions is challenging, and relies upon beam-based measurements of the accelerator optics in order to compensate for errors in the lattice. The requirements of the tuning procedure are:

1. The method must have a fast turnaround time, in order to allow iteration of corrections in near-real-time.

2. The method must scale well to large rings such as the ILC damping rings.
3. The method must reproducibly and reliably yield low-emittance conditions with rapid convergence.

A method for optics characterization and correction that meets these requirements has been demonstrated at CEsrTA, and will be detailed in Chapter 7.

CHAPTER 2

THE PHYSICS OF ELECTRON STORAGE RINGS

In particle accelerators magnets act as optical elements for charged particles. The most common magnetic elements (dipoles, quadrupoles, and sextupoles) act to deflect and focus the beam. Misalignments such as offsets and tilts in these magnets contribute to dilution of the vertical emittance. Other factors such as magnet power supply stability and ground motion also contribute to the vertical emittance, however in practice magnet misalignments are the most significant source. In order to understand how misalignments introduce vertical emittance, the formalism of charged particle beam optics must be discussed.

Material will be primarily drawn from [17–20], and the reader is encouraged to reference these texts for the full derivations and further discussion.

2.1 Co-Propagating Coordinate System

The coordinate system used in describing beam motion is a co-propagating system, shown in Figure 2.1.

A particle's coordinates while traveling through an accelerator structure can be written as a vector \vec{r} , which is a function of the longitudinal coordinate s :

$$\vec{r}(s) = (x, p_x, y, p_y, z, p_z) \quad (2.1)$$

where the location $\vec{r} = \vec{0}$ is defined to be the location of the reference particle. s is chosen as the independent variable rather than time t for convenience; for

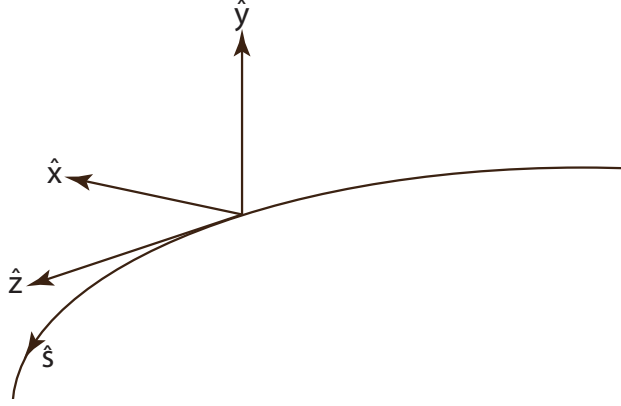


Figure 2.1: Co-propagating coordinate system used when discussing particle dynamics.

highly-relativistic particles, such as electrons in a storage ring, it is safe to assume $s = \beta ct \approx ct$.

We define the unit vectors of the coordinate system to be:

$$\hat{s}(s) = \hat{z}(s) = \frac{d\vec{r}_0}{ds} \quad (2.2)$$

$$\hat{x}(s) = -\rho(s) \frac{d\hat{s}(s)}{ds} \quad (2.3)$$

$$\hat{y}(s) = \hat{s}(s) \times \hat{x}(s) \quad (2.4)$$

with $\rho(s)$ being the bending radius of a horizontal steering magnet in the accelerator. $s = 0$ is defined to be the start of the accelerator structure, or “lattice.” For circular lattices this is an arbitrary choice, and is typically chosen for aesthetics or practicality, often at the injection point or interaction point.

Momenta p_i are defined as normalized quantities:

$$p_x = \frac{P_x}{P_0} \quad (2.5)$$

$$p_y = \frac{P_y}{P_0} \quad (2.6)$$

$$p_z = \frac{P_z - P_0}{P_0} \quad (2.7)$$

where P is the total particle momentum, and P_0 is the total momentum of the on-energy reference particle. In general, $|p_{x,y,z}| \ll 1$.

2.2 Magnets in Accelerators

The effect of electromagnetic fields on a charged particle is given by the Lorentz force law:

$$\frac{d\vec{p}}{dt} = e(\vec{E} + \vec{v} \times \vec{B}) \quad (2.8)$$

Using electromagnets, a magnetic field around $|\vec{B}| \approx 0.2$ T is common in the CESR storage ring. To produce the same $\frac{d\vec{p}}{dt}$ using only an electric field, $|\vec{E}|$ would have to be $|\vec{E}| = c|\vec{B}| \approx 6 \times 10^7$ V/m, which is extremely challenging and costly to achieve compared to the 0.2 T magnetic field. Additionally, for circular colliders it is possible to store counter-rotating beams of electrons and positrons using magnetic fields, whereas an electrostatic field would require the two species to propagate in the same direction. For these reasons, nearly all horizontal and vertical beam steering, focusing, and manipulation in accelerators is done using magnetic fields.

The fields in Eqn. 2.8 must satisfy Maxwell's equations:

$$\nabla \cdot \vec{E} = \frac{\rho}{\epsilon_0} \quad (2.9)$$

$$\nabla \times \vec{E} = -\frac{\partial \vec{B}}{\partial t} \quad (2.10)$$

$$\nabla \cdot \vec{B} = 0 \quad (2.11)$$

$$\nabla \times \vec{B} = \mu_0 \left(\vec{J} + \epsilon_0 \frac{\partial \vec{E}}{\partial t} \right) \quad (2.12)$$

where ϵ_0, μ_0 are the permittivity and permeability of free space, ρ is the charge density (per unit volume), and \vec{J} is the current density (per unit area). The magnetic fields near the center of a guide field magnet are static and charge-free ($\frac{d\vec{B}}{dt} = 0$, $\vec{E} = 0$, and $\vec{J} = 0$). Therefore, both the divergence and curl of the magnetic field are zero.

The simplest representation is a “hard-edge” model, where the magnetic fields have a definite beginning and end, and have no longitudinal dependence. This model is sufficient for much of optics design, and is presented here; readers are referenced to the texts at the beginning of the chapter for more detailed models including fringe fields and longitudinal fields from elements such as solenoids and wigglers. The transverse guide field $\vec{B}(x, y)$ can be expanded in a Taylor series:

$$\frac{qL}{P_0}(B_y + iB_x) = \sum_n (b_n + ia_n)(x + iy)^n \quad (2.13)$$

where n is the multipole order, starting at $n = 0$. Each term in the Taylor expansion also satisfies $\nabla \cdot \vec{B} = \nabla \times \vec{B} = 0$. The terms b_n represent the “normal” field components, and a_n are the “skew” field components.

It is convenient to design magnetic elements to primarily express one term in the multipole expansion. The magnetic fields and conceptual applications for magnets corresponding to the first three terms in the expansion are summarized in Table 2.1.

Order	Name	B_x	B_y	Use
0	Dipole	0	b_0	Steering
1	Quadrupole	$-b_1x$	$-b_1y$	Linear Focusing
2	Sextupole	b_2xy	$\frac{1}{2}b_2(x^2 - y^2)$	Chromatic Focusing

Table 2.1: Summary of magnet classes.

Magnets can also be designed to express multiple terms in the expansion (combined-function magnets), for example a dipole with a quadrupole gradient. However, combined-function magnets severely constrain the optics: the ratio between the different terms is often fixed. This style of magnet is occasionally used in situations where locations to place magnets are at a premium, and flexibility in the optics is not important.

Due to design constraints and manufacturing tolerances, all guide field magnets will have small, higher-order field components. Design constraints (such as finite magnet size) generate systematic multipole errors, and are consistent between magnets of the same design. Manufacturing tolerances will yield random multipole errors which differ between magnets of the same design. Systematic multipole fields can be computed through analytic means, and both systematic and random multipole fields may be directly measured using a field probe.

2.3 Transverse Beam Motion

Three-dimensional beam motion can be decomposed into three orthogonal modes, typically corresponding to motion primarily along the \hat{x} , \hat{y} , \hat{s} axes, each with an associated position and momentum. The \hat{x} , \hat{y} components are the transverse modes, and the \hat{s} component is the longitudinal. Many of the transverse equations will be the same in the horizontal and vertical; in these cases, the equations will be written using u and u' , where $u = x$ or y .

The transverse linear motion in a guide field can be modeled as a harmonic oscillator. The linear equations for transverse motion can therefore be written as:

$$x'' + K_x(s) x = 0, \quad K_x(s) = \frac{1}{\rho^2} \mp K_1(s) \quad (2.14)$$

$$y'' + K_y(s) y = 0, \quad K_y(s) = \pm K_1(s) \quad (2.15)$$

where K is the linear focusing term associated with quadrupoles, and ρ is the bending radius associated with dipoles. The asymmetry in the equations for horizontal and vertical motion arises from the fact that traditionally storage rings are oriented as a closed loop in the horizontal plane, therefore there is no dipole term ρ for vertical motion.

The solution to the equations of motion are a linear map, or transfer matrix. In this formalism the coordinates at the start of an element are mapped to the coordinates at the end of the element. For the full 6-dimensional case (three spatial dimensions and their associated momenta), the generalized transfer matrix can be written as:

$$\begin{pmatrix} x \\ p_x \\ y \\ p_y \\ z \\ p_z \end{pmatrix}^{out} = \begin{pmatrix} m_{11} & m_{12} & m_{13} & m_{14} & m_{15} & m_{16} \\ m_{21} & m_{22} & m_{23} & m_{24} & m_{25} & m_{26} \\ m_{31} & m_{32} & m_{33} & m_{34} & m_{35} & m_{36} \\ m_{41} & m_{42} & m_{43} & m_{44} & m_{45} & m_{46} \\ m_{51} & m_{52} & m_{53} & m_{54} & m_{55} & m_{56} \\ m_{61} & m_{62} & m_{63} & m_{64} & m_{65} & m_{66} \end{pmatrix} \begin{pmatrix} x \\ p_x \\ y \\ p_y \\ z \\ p_z \end{pmatrix}^{in} \quad (2.16)$$

or simply $\mathbf{x}^{out} = \mathbf{M}\mathbf{x}^{in}$. The on-diagonal 2×2 or 4×4 sub-matrices of the 6×6 transfer matrix are often used when longitudinal motion is neglected.

The mapping defined by the equations of motion is a canonical transformation, which is in turn symplectic. For a $2n \times 2n$ transfer matrix \mathbf{M} , the symplectic condition is:

$$\mathbf{M}^T \mathbf{S} \mathbf{M} = \mathbf{S} \quad (2.17)$$

where

$$\mathbf{S} = \begin{pmatrix} \mathbf{0}_n & \mathbf{I}_n \\ -\mathbf{I}_n & \mathbf{0}_n \end{pmatrix} \quad (2.18)$$

and $\mathbf{0}_n$ and \mathbf{I}_n are the $n \times n$ zero-matrix and identity matrix, respectively. Symplectic matrices also share the property that $|\mathbf{M}| = 1$.

Transfer matrices for the three most common elements (drifts, dipoles, and quadrupoles) are now discussed.

2.3.1 Drift

In a drift region there are no fields to affect beam motion, therefore particles will continue in the direction they were traveling when they entered. That is, for a drift of length L ,

$$x^{out} = x^{in} + L \frac{dx}{ds} = x^{in} + p_x^{in} L \quad (2.19)$$

$$p_x^{out} = p_x^{in} \quad (2.20)$$

and similarly for y . For the transverse motion, this can be written as a 4×4 transfer matrix:

$$\mathbf{M}_{drift} = \begin{pmatrix} 1 & L & 0 & 0 \\ 0 & 1 & 0 & 0 \\ 0 & 0 & 1 & L \\ 0 & 0 & 0 & 1 \end{pmatrix} \quad (2.21)$$

Note that this is already an approximation, which assumes the path length is independent of the path taken through the drift.

2.3.2 Dipole

Dipoles deflect the particle trajectory transversely. The deflection angle θ is determined by the magnet length L and bending radius ρ . The bending radius can be calculated from the beam rigidity:

$$\frac{1}{\rho} = \left| \frac{ec}{\beta E} B \right| \quad (2.22)$$

For a highly relativistic electron or positron beam, this simplifies to:

$$E [\text{GeV}] = 0.2998 B \rho [T \cdot m] \quad (2.23)$$

Note that in a dipole, the bending radius ρ for the on-energy particle is taken to be the reference for the co-propagating coordinate system previously defined at the beginning of the chapter.

The two most commonly-used classes of dipoles are sector and rectangular dipoles. In a sector dipole, the reference particle enters the magnet normal to its end face, whereas in a rectangular dipole, the reference particle enters with a non-zero angle. In both cases there is a small amount of focusing, called “edge focusing.” This is a separate effect from “fringe fields.”

The 4×4 transverse transfer matrix for a horizontally-deflecting sector dipole with deflecting angle $\theta = L/\rho$ is:

$$\mathbf{M}_{sector} = \begin{pmatrix} \cos \theta & \rho \sin \theta & 0 & 0 \\ -\frac{1}{\rho} \sin \theta & \cos \theta & 0 & 0 \\ 0 & 0 & 1 & L \\ 0 & 0 & 0 & 1 \end{pmatrix} \quad (2.24)$$

For a horizontally-deflecting rectangular dipole, focusing occurs in the vertical:

$$\mathbf{M}_{rect} = \begin{pmatrix} 1 & \rho \sin \theta & 0 & 0 \\ 0 & 1 & 0 & 0 \\ 0 & 0 & 1 - \frac{L}{f_y} & L \\ 0 & 0 & -\frac{2}{f_y} + \frac{L}{2f_y} & 1 - \frac{L}{f_y} \end{pmatrix} \quad (2.25)$$

where f_y is the effective focal length of the edge focusing.

2.3.3 Quadrupole

Quadrupole magnets act as a lens which focuses the beam. The field must satisfy $\nabla \times \vec{B} = 0$, therefore quadrupoles focus in one plane while simultaneously defocusing in the other. The transfer matrix for the thin quadrupole approximation is:

$$\mathbf{M}_{quad} = \begin{pmatrix} 1 & 0 & 0 & 0 \\ -1/f & 1 & 0 & 0 \\ 0 & 0 & 1 & 0 \\ 0 & 0 & 1/f & 1 \end{pmatrix} \quad (2.26)$$

$$= \begin{pmatrix} \mathbf{M}_F & \mathbf{0}_2 \\ \mathbf{0}_2 & \mathbf{M}_D \end{pmatrix} \quad (2.27)$$

where

$$f = \lim_{L \rightarrow 0} \frac{1}{|K|L} \quad (2.28)$$

with quadrupole strength K defined by $K = \frac{e}{p} b_1$. $\mathbf{M}_{F,D}$ and $\mathbf{0}_2$ are 2×2 submatrices. Although focusing in one plane causes defocusing in the other, it is easily shown that net focusing can be achieved through alternating focusing and defocusing quadrupoles.

2.3.4 One-Turn Matrix

The transport matrix for a series of elements is simply the product of the individual transfer matrices. For elements $1, 2, \dots, N-1, N$:

$$\mathbf{M}_{1 \rightarrow N} = \mathbf{M}_N \mathbf{M}_{N-1} \dots \mathbf{M}_2 \mathbf{M}_1 \quad (2.29)$$

For a circular lattice, a transfer matrix can be constructed which represents one full turn through the accelerating structure, called the “one-turn matrix.” The one-turn matrix is different at each element, however if the one-turn matrix is known at element 1 and the transfer matrix from $1 \rightarrow 2$ is known, then the one-turn matrix at element 2 is given by:

$$\mathbf{M}_2^{one-turn} = \mathbf{M}_{1 \rightarrow 2} \mathbf{M}_1^{one-turn} \mathbf{M}_{1 \rightarrow 2}^{-1} \quad (2.30)$$

2.4 Twiss Parameters and Emittance

The equilibrium phase space occupied by a bunch in a storage ring is typically a 6-dimensional Gaussian. It is useful to parameterize the bunch profile in trans-

verse phase space using the so-called “Twiss parameters” α, β, γ , which are defined by the focusing elements in the lattice, and are distinct in the horizontal and vertical modes. β defines the amplitude of particle oscillations, and is also called the envelope function. α and γ are defined with respect to β :

$$\alpha = -\frac{1}{2} \frac{d\beta}{ds} \quad (2.31)$$

$$\gamma = \frac{1 + \alpha^2}{\beta} \quad (2.32)$$

The Twiss parameters define an ellipse in phase space, of the following form:

$$\pi\epsilon_u = \gamma u^2 + 2\alpha uu' + \beta u'^2 \quad (2.33)$$

where ϵ_u is the emittance, equal to the area of the phase space ellipse within a factor of π . The physical interpretations of the Twiss parameters and emittance as parameters of the phase space ellipse are shown in Figure 2.2.

In addition to the beta functions β , one may also use the betatron phase advance ϕ to describe the focusing between two points in a lattice:

$$\phi_u^{1 \rightarrow 2} = \int_{s_1}^{s_2} \frac{ds}{\beta_u(s)} \quad (2.34)$$

where ϕ has units of radians. The integral of the betatron phase advance across the entire lattice is called the tune ν :

$$\nu_u = \int_{s_0}^{s_0+C} \frac{ds}{\beta_u(s)} \quad (2.35)$$

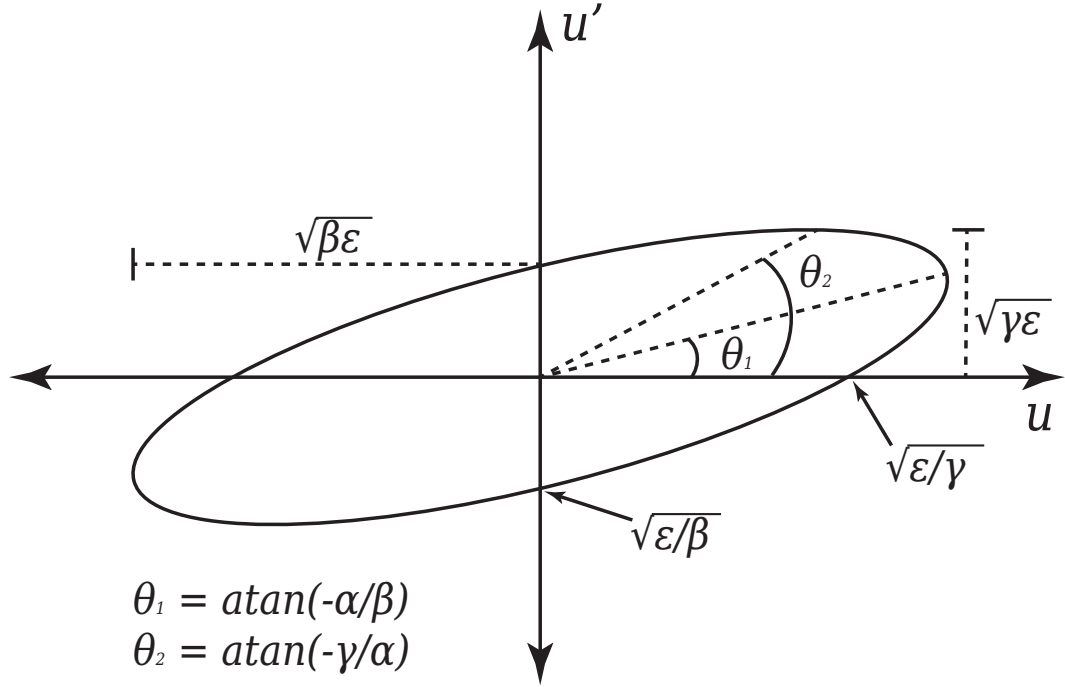


Figure 2.2: Physical interpretation of the Twiss parameters β , α , γ and emittance ϵ in phase space.

It is also convenient to define the tune in cycles rather than radians:

$$Q_u = \frac{\nu_u}{2\pi} \quad (2.36)$$

The tunes Q_u are typically of order 10 in many storage rings, and have a nonzero fractional component in order to avoid resonances occurring when a lattice error is seen by the beam with the same phase advance on multiple turns. When measuring the tunes of a stored beam it is common to use a spectrum analyzer connected to a single electrode, which will then read the tunes as a frequency. Note that when observing at a single location, it is not possible to resolve the integer component of the tunes; therefore, the tunes observed as a frequency are only the fractional component:

$$f_u = \frac{Q_u - \text{int}(Q_u)}{T_0} \quad (2.37)$$

where T_0 is the circulation time. When correcting the lattice optics, the integer part of the tunes are also measured and known. In practice only the fractional part of the tune is varied during operation.

The transfer matrices can be parameterized in terms of the Twiss parameters. For a 2×2 transfer matrix (describing either x or y), propagating from $s_1 \rightarrow s_2$:

$$\mathbf{M} = \begin{pmatrix} \sqrt{\frac{\beta_u(s_2)}{\beta_u(s_1)}} (\cos \Delta\phi + \alpha_u(s_1) \sin \Delta\phi) & \sqrt{\beta_u(s_1)\beta_u(s_2)} \sin \Delta\phi \\ -\frac{1+\alpha_u(s_1)\alpha_u(s_2)}{\sqrt{\beta_u(s_1)\beta_u(s_2)}} \sin \Delta\phi + \frac{\alpha_u(s_1)-\alpha_u(s_2)}{\sqrt{\beta_u(s_1)\beta_u(s_2)}} \cos \Delta\phi & \sqrt{\frac{\beta_u(s_1)}{\beta_u(s_2)}} (\cos \Delta\phi - \alpha_u(s_2) \sin \Delta\phi) \end{pmatrix} \quad (2.38)$$

where $\Delta\phi = \phi_2 - \phi_1$ is the phase advance between the two locations. This can be decomposed into:

$$\mathbf{M} = \begin{pmatrix} \sqrt{\beta_u(s_2)} & 0 \\ -\frac{\alpha_u(s_2)}{\sqrt{\beta_u(s_2)}} & \frac{1}{\sqrt{\beta_u(s_2)}} \end{pmatrix} \begin{pmatrix} \cos \Delta\phi & \sin \Delta\phi \\ -\sin \Delta\phi & \cos \Delta\phi \end{pmatrix} \begin{pmatrix} \frac{1}{\sqrt{\beta_u(s_1)}} & 0 \\ \frac{\alpha_u(s_1)}{\sqrt{\beta_u(s_1)}} & \sqrt{\beta_u(s_1)} \end{pmatrix} \quad (2.39)$$

$$= \mathbf{G}_u^{-1}(s_2) \mathbf{R}(\Delta\phi) \mathbf{G}_u(s_1) \quad (2.40)$$

By using \mathbf{G}_u in this fashion, the transfer matrix is cast in normalized coordinates which are independent of the Twiss parameters.

2.5 Closed Orbit

For a fixed location i , if there exists a vector \mathbf{x}_i such that after one turn through the ring (neglecting synchrotron radiation emission, see Sec. 2.9) the particle will arrive at exactly the same \mathbf{x}_i , the vector \mathbf{x}_i is said to be on the closed orbit. The closed orbit is the set of \mathbf{x}_i 's for every location where the particle trajectory closes on itself after one turn.

When including the effects of radiation damping and excitation, the turn-to-turn trajectory will differ slightly from the closed orbit. However, the turn-averaged trajectory will converge to the closed orbit.

2.6 Energy Dependence: Dispersion and Chromaticity

Through the beam rigidity (Eq. 2.23), it is clear that for a fixed magnetic field B , particles of different energies will experience a different bending radius. The energy dependence of the closed orbit is characterized by the dispersion η :

$$u(s) = u_0(s) + \eta_u(s) \delta \quad (2.41)$$

$$\eta_u(s) = \frac{du(s)}{d\delta} \quad (2.42)$$

where $\delta = (E - E_0)/E_0$ is the energy deviation of the particle with respect to the reference particle. All steering elements will generate dispersion. In particular, dipoles will define a non-zero dispersion in the design horizontal optics. In nearly all accelerators the vertical dispersion is zero in the design, as no steering is required to maintain an on-axis vertical orbit.

Similarly, the focusing effect of quadrupoles depends inversely on energy. The change in focusing from a change in energy δ can be integrated around the ring to find the change in tune ΔQ . This is defined as the chromaticity ξ :

$$\xi_u = \frac{dQ_u}{d\delta} \quad (2.43)$$

The chromaticity affects beam stability in that particles with different energies will have different tunes. Positive chromaticity ($\xi > 0$) stabilizes head-tail motion of the bunch which is driven by resistive wall impedance. Therefore, most machines are designed to operate with slightly positive chromaticity. However, without compensation the natural chromaticity due to dipoles and quadrupoles is nearly always negative, and stronger quadrupole focusing will lead to larger negative chromaticity. Sextupoles are used to raise the chromaticity toward a more neutral value to stabilize beam dynamics. A horizontal offset in a sextupole produces a quadrupole focusing which increases linearly with amplitude. Therefore, by placing sextupoles in regions with finite horizontal dispersion, particles are “sorted” by their energies and thus receive the required energy-dependent focusing. However, sextupoles also introduce non-linear beam dynamics which may limit the stable phase space a particle can inhabit.

2.7 Coupled Motion

In an ideal lattice which is free of errors, the horizontal and vertical motion are independent. However, magnet misalignments such as quadrupole tilts will in-

introduce a correlation, or coupling, between horizontal and vertical motion. In storage rings where the horizontal emittance is much larger than the vertical, this will lead to an increase in the vertical emittance. Many accelerators intentionally introduce coupling to reduce bunch-density-dependent effects. However, in linear colliders the disruption factor H_D is reduced by maintaining a “ribbon” beam with $\sigma_v \ll \sigma_h$, and low coupling is desirable.

In a lattice with coupling, the terms “horizontal-mode” and “vertical-mode” lose meaning, as the x and y motion now contain components of both modes. This ambiguity is averted by using the “normal” modes a and b , referring to the mostly-horizontal and mostly-vertical modes, respectively. When equations are symmetric between the a - and b -modes, subscript v will indicate a or b . Similarly, when coupling exists between all three modes (horizontal, vertical, and longitudinal), the z -mode is deprecated in favor of the “mostly-longitudinal” c -mode.

The formalism used here for describing coupling is outlined in [21]. For a system without coupling, the transverse 4×4 transfer matrix is block-diagonal:

$$\mathbf{T} = \begin{pmatrix} \mathbf{M} & \mathbf{0}_2 \\ \mathbf{0}_2 & \mathbf{N} \end{pmatrix} \quad (2.44)$$

When coupling is introduced, nonzero off-diagonal sub-matrices appear:

$$\mathbf{T} = \begin{pmatrix} \mathbf{M} & \mathbf{m} \\ \mathbf{n} & \mathbf{N} \end{pmatrix} \quad (2.45)$$

This can then be decomposed into a block-diagonal form:

$$\mathbf{T} = \mathbf{VUV}^{-1} \quad (2.46)$$

where

$$\mathbf{U} = \begin{pmatrix} \mathbf{A} & \mathbf{0} \\ \mathbf{0} & \mathbf{B} \end{pmatrix} \quad (2.47)$$

$$\mathbf{V} = \begin{pmatrix} \gamma\mathbf{I} & \mathbf{C} \\ -\mathbf{C}^+ & \gamma\mathbf{I} \end{pmatrix} \quad (2.48)$$

γ is defined by $\gamma^2 + \|\mathbf{C}\| = 1$, and \mathbf{C}^+ is the symplectic conjugate to \mathbf{C} . This allows for the standard, decoupled analysis to be applicable in an arbitrarily-coupled system.

It is useful to normalize out the betatron amplitude oscillations from the coupling matrix in order to simplify analysis. $\bar{\mathbf{C}}$ is the normalized form of \mathbf{C} :

$$\bar{\mathbf{C}} = \mathbf{G}_a \mathbf{C} \mathbf{G}_b^{-1} \quad (2.49)$$

where the matrices $\mathbf{G}_{a,b}$ are defined in Eqns. 2.39–2.40. Three of the four coupling matrix elements are directly measurable. $\bar{C}_{22,11}$ are the in-phase matrix elements, and represent a rotation of the beam in x - y space, as indicated in Figure 2.3. \bar{C}_{22} represents the a -mode which is visible in the vertical response at a BPM, and \bar{C}_{11} represents the b -mode which is visible in the horizontal response.

The out-of-phase component \bar{C}_{12} represents an increase in the girth of the beam in x - y space, as shown in 2.3. \bar{C}_{12} can be observed in two ways: as the

out-of-phase response of either the a -mode in the vertical, or the b -mode in the horizontal.

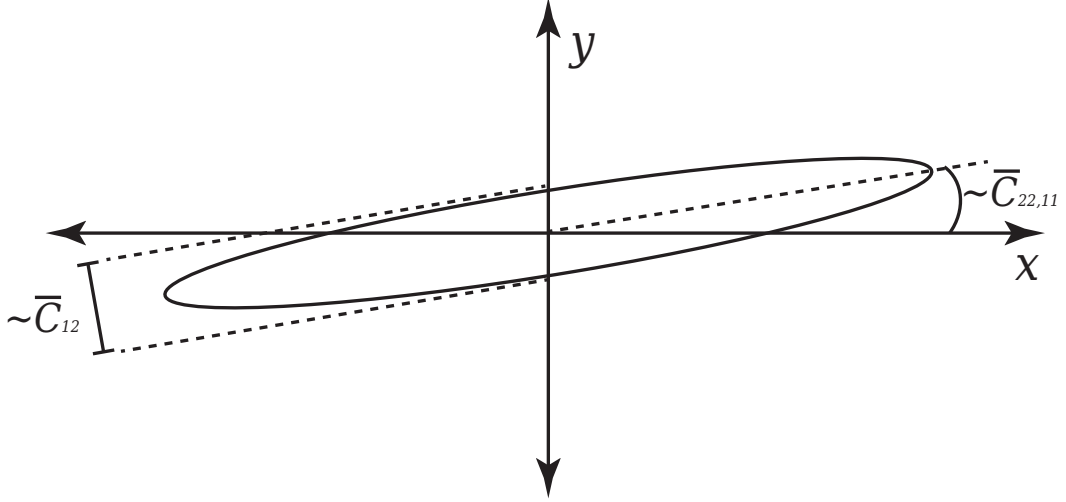


Figure 2.3: Physical interpretation of \bar{C} with respect to the transverse cross-section of the beam. \bar{C}_{12} is the out-of-phase coupling, and therefore represents a “widening” of the beam ellipse. $\bar{C}_{22,11}$ are both in-phase components, and produce a rotation of the beam ellipse.

Including coupling, the x, y position at a fixed location s on turn n can be written as:

$$\begin{pmatrix} x(s) \\ y(s) \end{pmatrix} = A \begin{pmatrix} \gamma(s) \sqrt{\beta_a(s)} \cos (\psi_a(s) + n\nu_a) \\ -\sqrt{\beta_b(s)} \left[\bar{C}_{22}(s) \cos (\psi_a(s) + n\nu_a) + \bar{C}_{12}(s) \sin (\psi_a(s) + n\nu_a) \right] \end{pmatrix} + B \begin{pmatrix} \sqrt{\beta_a(s)} \left[\bar{C}_{11}(s) \cos (\psi_b(s) + n\nu_b) - \bar{C}_{12}(s) \sin (\psi_b(s) + n\nu_b) \right] \\ \gamma(s) \sqrt{\beta_b(s)} \cos (\psi_b(s) + n\nu_b) \end{pmatrix} \quad (2.50)$$

where A, B are the normalized amplitudes of the a - and b -mode motion.

2.8 Radiation Integrals

It is useful to define a set of integrals which are used to calculate the effects of synchrotron radiation, referred to as the radiation integrals. These integrals are necessary when discussing radiation damping and excitation (Sec. 2.9), transverse emittance (Sec. 2.10), and longitudinal beam dynamics (Sec. 2.11). In most texts the integrals are presented for decoupled motion. However, beam motion in an actual machine is never fully decoupled, due to tolerances in magnet alignment, manufacturing, and so forth. Coupling must be included in order to accurately describe the effects of radiation.

For the case of coupled motion, a few additional definitions must be made, following the `Bmad` convention [22]. Rather than assuming all curvature is in the horizontal plane, the more general $\mathbf{g} = (g_x, g_y)$ is used, which points parallel to ρ (the total radius of curvature) with magnitude $|\mathbf{g}| = g = 1/\rho$. (Note that although g is a scalar, it still depends on coordinates (x, y, s)). Additionally, we define the dispersion in the a - and b -modes by their components in the x, y frame, $\boldsymbol{\eta}_v = (\eta_{x,v}, \eta_{y,v})$. The synchrotron radiation integrals for coupled motion are summarized in Equations 2.51–2.57.

$$I_1 = \oint \boldsymbol{\eta} \cdot \mathbf{g} \, ds \quad (2.51)$$

$$I_2 = \oint g^2 \, ds \quad (2.52)$$

$$I_3 = \oint g^3 \, ds \quad (2.53)$$

$$I_{4,a} = \oint (g^2 \mathbf{g} \cdot \boldsymbol{\eta}_a + \nabla g^2 \cdot \boldsymbol{\eta}_a) \, ds \quad (2.54)$$

$$I_{4,b} = \oint (g^2 \mathbf{g} \cdot \boldsymbol{\eta}_b + \nabla g^2 \cdot \boldsymbol{\eta}_b) \, ds \quad (2.55)$$

$$I_{5,a} = \oint g^3 \mathcal{H}_a ds \quad (2.56)$$

$$I_{5,b} = \oint g^3 \mathcal{H}_b ds \quad (2.57)$$

The function \mathcal{H}_v in $I_{5,v}$ ($v = a, b$) is defined as

$$\mathcal{H}_v = \gamma_v \eta_v^2 + 2\alpha_v \eta_v \eta'_v + \beta_v \eta_v'^2 \quad (2.58)$$

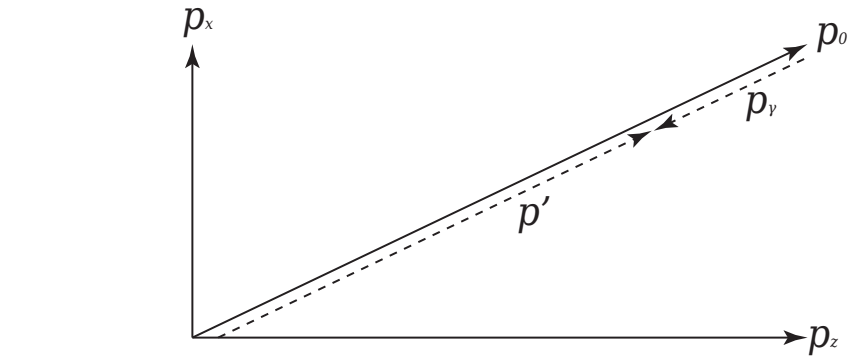
2.9 Radiation Damping and Quantum Excitation

When a particle is transversely deflected in a magnetic field it emits synchrotron radiation nearly tangential to its trajectory, with an angular spread of approximately $1/\gamma$. As each individual particle within a bunch has some small transverse component of momentum, the momentum lost to radiation emission also contains a transverse component. The momentum lost is replaced by a purely longitudinal component in RF cavities. Over many turns, this leads to radiation damping. This process is illustrated in Figure 2.4.

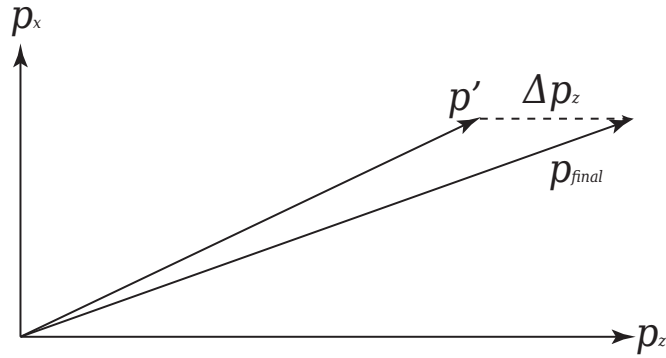
2.9.1 Damping

Betatron oscillations are damped exponentially as

$$A_u = A_{0,v} e^{-\alpha_v t} \quad (2.59)$$



(a)



(b)

Figure 2.4: A conceptual illustration of radiation damping. (a) A particle with total momentum p_0 radiates a photon with momentum p_γ , leaving momentum p' . (b) The longitudinal component of the momentum is replaced by RF cavities, resulting in p_{final} . The net result is a reduction in transverse momentum.

where $\alpha_v = 1/\tau_v$ is the damping decrement, determined by radiation emission.

This can be rephrased as an emittance damping:

$$\epsilon_v = \epsilon_{0,v} e^{-2\alpha_v t}, \text{ or} \quad (2.60)$$

$$\frac{d\epsilon_v}{dt} = -2\alpha_v \epsilon_{0,v} \quad (2.61)$$

The damping decrements can be computed from the radiation integrals I_2

and I_4 :

$$\alpha_v = \frac{U_0}{2E_0 T_0} J_v \quad (2.62)$$

$$J_v = \begin{cases} 1 - \frac{I_{4,v}}{I_2}, & v = a, b \\ 1 + \frac{I_{4,a} + I_{4,b}}{I_2}, & v = c \end{cases} \quad (2.63)$$

where T_0 is the circulation time, J_v are the damping partition numbers. Note that $J_a + J_b + J_c = 4$, implying that there is a total amount of damping per turn which is then distributed among the three dimensions. This is the Robinson Theorem. U_0 is the power radiated per turn:

$$U_0 = \frac{C_\gamma E^4}{2\pi} I_2 \quad (2.64)$$

$$\text{with } C_\gamma = \frac{4\pi}{3} \frac{r_e}{(m_e c^2)^3} = 8.86 \times 10^{-5} \text{ m/GeV}^3.$$

2.9.2 Excitation

When the emission of synchrotron radiation occurs in a dispersive region (i.e., $\mathcal{H}_v \neq 0$), the particle's change in energy is accompanied by a change in the particle's orbit onto a dispersive trajectory. This creates an emittance growth rate due to quantum excitation (QE):

$$\left. \frac{d\epsilon_v}{dt} \right|_{QE} = \frac{\langle \mathcal{N} \mathcal{H} \langle u^2 \rangle \rangle}{2E_0} \quad (2.65)$$

where $\langle u^2 \rangle$ is the mean square energy per photon emitted, \mathcal{N} is the average photon emission rate around the entire lattice (in units of γ/s), and E_0 is the beam energy. This growth rate is always nonzero in the horizontal, as bending magnets are required in order to store the beam, and therefore \mathcal{H}_a cannot be zero everywhere.

There is also a “quantum excitation” growth rate due to the distribution of finite opening angles for radiated photons:

$$\left. \frac{d\epsilon_v}{dt} \right|_{OA} = \frac{\langle \mathcal{N} \langle u^2 \rangle \beta_v \rangle}{4\gamma^2 E_0^2} \quad (2.66)$$

where γ in the denominator is the relativistic factor. In practice, this term is much smaller than Eqn. 2.65 for the horizontal mode. For the vertical, \mathcal{H}_b is nearly always zero by design, therefore Eqn. 2.65 is zero and Eqn. 2.66 dominates.

2.10 Equilibrium Transverse Emittance

The equilibrium emittance, also called the “single-particle” natural emittance or zero-current emittance, is determined by a balance between radiation damping (Eqns. 2.61 and 2.63) and excitation from stochastic photon emission (Eqns. 2.65-2.66):

$$\left. \frac{d\epsilon_v}{dt} \right|_{damping} + \left. \frac{d\epsilon_v}{dt} \right|_{QE} + \left. \frac{d\epsilon_v}{dt} \right|_{OA} = 0 \quad (2.67)$$

For the horizontal, the term for quantum excitation is much larger than the term from the finite radiation opening angle. After some math, the resulting horizontal emittance is:

$$\epsilon_a = C_q \frac{\gamma^2 I_{5,a}}{J_a I_2} \quad (2.68)$$

with $C_q = 8.85 \times 10^{-5} \text{ m/GeV}^3$.

This result warrants a few comments. First, I_5 is an integral of \mathcal{H} over all regions where transverse deflection occurs, and therefore where synchrotron radiation is produced. It follows that in order to minimize the design emittance, one must minimize \mathcal{H} in regions with strong bending fields. This is most often accomplished through reducing the dispersion and its derivative in the dipoles.

Second, the equilibrium emittance is proportional to γ^2 . All else equal, a low-energy lattice will inherently have lower emittance than a high-energy lattice.

Third, the vertical dispersion in nearly all accelerators is globally zero by design, therefore $I_{5,b} = 0$ and Eqn. 2.68 is not valid for the vertical emittance in an ideal lattice. In this scenario the vertical emittance is determined by the growth rate from the finite spread in opening angle of radiation. The equilibrium vertical emittance is then:

$$\epsilon_b^{min} = C_q \frac{\langle \beta_b \rangle I_3}{2J_b I_2} \quad (2.69)$$

where $\langle \beta_b \rangle$ is the average vertical beta in the ring. ϵ_b^{min} is typically of order 0.1 pm for most relativistic electron/positron storage rings. However, in an actual ma-

chine the vertical dispersion is never identically zero due to misalignments and magnet imperfections. η_b (and therefore \mathcal{H}_b and $I_{5,b}$) is no longer zero in this case, and Eqn. 2.68 will determine the equilibrium vertical emittance. It is also interesting to note that whereas $\epsilon \propto \gamma^2$ in Eqn. 2.68, ϵ_b^{min} does not directly scale with beam energy.

2.10.1 Damping Wigglers

In Equation 2.68, it is clear that an increase in I_2 without increasing I_5 will reduce the equilibrium emittance. This can be achieved by placing an element consisting of an alternating series of strong dipoles (called a “wiggler”) in a region with small \mathcal{H} (that is, $\eta = \eta' = 0$). By alternating the polarity of adjacent poles, the dispersion is kept to a minimum and I_5 is contained. When a wiggler is designed specifically and solely for this purpose, it is called a damping wiggler.

Damping wigglers modify the equilibrium emittance in Equation 2.68 as:

$$\epsilon_v^w = C_q \frac{\gamma^2 I_{5,v}^0 + I_{5,v}^w}{J_v I_2^0 + I_2^w} \quad (2.70)$$

where $I_{2,5}^0$ are the unperturbed radiation integrals, and $I_{2,5}^w$ are the contributions to the radiation integrals from the damping wigglers. The dipole field $B(s)$ inside the damping wigglers can be approximated as varying sinusoidally:

$$B_w(s) = B_w^{max} \cos\left(\frac{2\pi}{\lambda_w} s\right) \quad (2.71)$$

with λ_w as the wiggler period, that is, the distance between poles of the same polarity. The bending radius ρ can be determined from the beam rigidity (Eqn. 2.23).

The damping wigglers also generate a small amount of dispersion internally, therefore \mathcal{H} is nonzero, and the wigglers will introduce a small but finite contribution to I_5 , and therefore some level of horizontal emittance.

Damping wigglers will contribute to an increase in the total energy radiated per turn by increasing I_2 in Eqn. 2.64, therefore the damping time $\tau = 1/\alpha$ will decrease. They will also significantly contribute to the energy spread (Eqn. 2.75) through an increase in I_3 , which outpaces the increase in I_2 in the denominator.

2.11 Longitudinal Beam Dynamics

The longitudinal beam dynamics are distinct from the transverse dynamics, though many similarities arise, including a disturbing level of repetition in symbols used to represent entirely different concepts from their prior definitions. Care must be taken to differentiate between these definitions.

Stochastic emission of synchrotron radiation requires the energy to be replaced by radio-frequency (RF) cavities, which produce a sinusoidal electric field that the particles “surf” to gain longitudinal momentum. The sinusoidal RF field enforces collections of particles to become “bunched” longitudinally. Bunches are separated by a minimum time $\Delta t = 1/f_{RF}$, where f_{RF} is the frequency of the RF cavity, typically in the hundreds to thousands of MHz.

The RF frequency also defines the number of possible bunches in the ring,

called the harmonic number h :

$$h = \text{Circumference} \times \frac{f_{RF}}{c_{light}} \quad (2.72)$$

Note that this mandates that the circumference be an integer multiple of RF wavelengths.

Particles circulating at different energies will travel different path lengths and different transit times. The momentum compaction factor α_p is the change in circumference with respect to energy:

$$\alpha_p = \frac{\Delta C/C}{\Delta E/E_0} \quad (2.73)$$

The slippage factor η (not to be confused with the dispersion) is the change in transit time with respect to energy:

$$\eta = \frac{\Delta T/T_0}{\Delta E/E_0} \quad (2.74)$$

Particles arriving at the RF cavity at different times will experience different accelerating voltages. The phase of the RF cavities is set such that this introduces a longitudinal focusing. The resulting bunches have a well-defined energy spread and bunch length:

$$\frac{\sigma_E}{E} = \sqrt{\frac{C_q \gamma^2}{J_z} \frac{I_3}{2I_2 + I_{4,a} + I_{4,b}}} \quad (2.75)$$

$$\sigma_s = \frac{c_{light} |\eta| \sigma_E}{\omega_s E_0} \quad (2.76)$$

where C_q is defined in Sec. 2.10, and $\omega_s = 2\pi\nu_s$ is the synchrotron frequency, analogous to the tunes in the transverse motion:

$$\nu_s = \sqrt{\frac{h|\eta|eV}{2\pi\beta^2 E}} \quad (2.77)$$

where $\beta = v/c$ (and not the envelope function from Section 2.4), e is the elementary charge, V is the cavity voltage, and η is the slippage factor.

Note in Equation 2.75 that the energy spread does not depend on the RF voltage, whereas the bunch length and synchrotron tune (Eqns. 2.77, 2.76) do.

2.12 Vertical Emittance Dilution from Lattice Errors

In a real accelerator components are not perfectly aligned. Rather, there will be a distribution of strength errors, offsets, and rolls which will generate orbit, beta, dispersion, and coupling errors, which in turn generate vertical emittance. The goal of beam-based emittance tuning is to compensate for these errors.

2.12.1 Orbitry Errors

Errors and misalignments in the main dipole field will generate a closed-orbit perturbation. For dipole errors i , the orbit $u = x, y$ is perturbed as:

$$u(s) = \frac{\sqrt{\beta_v(s)}}{2 \sin \pi \nu_v} \sum_i \theta_{u,i} \sqrt{\beta_v(s_i)} \cos [|\phi_v(s) - \phi_v(s_i)| - \pi \nu_v] \quad (2.78)$$

where again $\nu = a, b$ represents the normal modes. There are three primary sources of steering errors: steering strength errors, dipole rolls, and offsets in quadrupoles. Steering strength errors arise from poor magnet regulation or calibration. A dipole roll will introduce dipole kicks into the vertical beam motion, propagating as a vertical steering error. Offsets in quadrupoles will produce a dipole kick proportional to the amplitude of the offset.

Steering errors are compensated through use of dipole (steering) correctors. For horizontal steerings these tend to be independently-powered trim windings on the dipoles. For vertical steerings there are two common solutions: dedicated vertical steering correctors, and trim windings on the side poles of sextupoles.

2.12.2 Beta Errors

Focusing errors will distort the beta functions, producing a so-called “beta beat,” or a betatron phase error. Contributions to beta beat are quadrupole K errors and offsets in sextupoles.

A distribution of focusing errors $(\Delta KL)_i$ will propagate as:

$$\frac{\Delta\beta_v(s)}{\beta_v(s)} = \frac{1}{2 \sin (2\pi\nu_v)} \sum_i (\Delta KL)_i \beta_v(s_i) \cos [2|\phi_v(s) - \phi_v(s_i)| - 2\pi\nu_v] \quad (2.79)$$

Beta beat is corrected by adjusting the individual strengths of quadrupoles to match the design beta functions or betatron phase advance. Note that the beta

beat must be corrected in both horizontal and vertical modes simultaneously, as any change in quadrupole strength will affect both.

2.12.3 Vertical Dispersion Errors

Vertical dispersion in most accelerators is zero by design, as there is no need for vertical steering in the design lattice, and therefore nothing to create vertical dispersion. However, dipole rolls, offsets in quadrupoles, and coupling generated by sextupole offsets and rotated quadrupoles will introduce vertical dispersion, and therefore vertical emittance.

The vertical dispersion resulting from a distribution of these errors can be written as an integral around the ring:

$$\eta_y(s) = \frac{\sqrt{\beta_b(s)}}{2 \sin \pi \nu_b} \int_s^{s+C} F(s') \sqrt{\beta_b(s')} \cos [|\phi_b(s') - \phi_b(s_i)| - \pi \nu_b], \quad (2.80)$$

$$F(s) = (K + S \eta_x) y_c(s) - K_{sk} \eta_x - \theta_y \quad (2.81)$$

where K, S, K_{sk}, θ_y are the quadrupole, sextupole, skew quadrupole, and vertical steering strengths, and $y_c(s)$ is the vertical closed orbit.

The vertical dispersion can be corrected through a combination of vertical steerings and skew quadrupoles.

2.12.4 Coupling Errors

Transverse coupling arises from rotated quadrupoles and offset and rotated sextupoles.

For a quadrupole with tilt θ , the 4×4 transfer matrix (Eqn. 2.27) becomes:

$$\mathbf{M}_{quad, \text{tilted}} = \mathbf{R}^{-1}(\theta)\mathbf{M}_{quad}\mathbf{R}(\theta) \quad (2.82)$$

$$= \begin{pmatrix} \mathbf{M}_F \cos^2\theta + \mathbf{M}_D \sin^2\theta & \sin\theta \cos\theta(\mathbf{M}_D - \mathbf{M}_F) \\ \sin\theta \cos\theta(\mathbf{M}_D - \mathbf{M}_F) & \mathbf{M}_D \cos^2\theta + \mathbf{M}_F \sin^2\theta \end{pmatrix} \quad (2.83)$$

where $\mathbf{R}(\theta)$ is a rotation matrix defined by:

$$\mathbf{R}(\theta) = \begin{pmatrix} \mathbf{I} \cos\theta & \mathbf{I} \sin\theta \\ -\mathbf{I} \sin\theta & \mathbf{I} \cos\theta \end{pmatrix} \quad (2.84)$$

Coupling is corrected using a distribution of skew quadrupoles.

Coupling will not directly impact the normal-mode emittances $\epsilon_{a,b}$. Rather, it will do two things. First, it will couple the horizontal dispersion into the vertical, generating vertical emittance. Second, it will alter the projections of the emittances $\epsilon_{a,b}$ into the lab-frame beam sizes $\sigma_{x,y}$, which are the true observables.

The components of beam size from the two modes are added in quadrature. For the horizontal beam size:

$$\sigma_x = \sqrt{\sigma_{x,a}^2 + \sigma_{x,b}^2 + \sigma_{x,\eta_x}^2} \quad (2.85)$$

$$\sigma_{x,a} = \gamma \sqrt{\epsilon_a \beta_a} \quad (2.86)$$

$$\sigma_{x,b} = \sqrt{\epsilon_b \beta_a} [\bar{C}_{11}^2 + \bar{C}_{12}^2]^{1/2} \quad (2.87)$$

$$\sigma_{x,\eta_x} = \eta_x \frac{\sigma_E}{E} \quad (2.88)$$

where $\eta_x = \sqrt{\eta_{x,a}^2 + \eta_{x,b}^2}$. Similarly, for the vertical:

$$\sigma_y = \sqrt{\sigma_{y,a}^2 + \sigma_{y,b}^2 + \sigma_{y,\eta_y}^2} \quad (2.89)$$

$$\sigma_{y,a} = \sqrt{\epsilon_a \beta_b} [\bar{C}_{22}^2 + \bar{C}_{12}^2]^{1/2} \quad (2.90)$$

$$\sigma_{y,b} = \gamma \sqrt{\epsilon_b \beta_b} \quad (2.91)$$

$$\sigma_{y,\eta_y} = \eta_y \frac{\sigma_E}{E} \quad (2.92)$$

with $\eta_y = \sqrt{\eta_{y,a}^2 + \eta_{y,b}^2}$.

2.13 Vertical Emittance Dilution from Time-Varying Sources

If an element in the lattice is varying on a timescale which is short compared to the damping time $\tau = 1/\alpha$ (Eqn. 2.62), the beam will be excited to a larger equilibrium emittance. The effect of a time-varying element can be interpreted as an additional growth rate, to be added to the right-hand side of Eqn. 2.67:

$$\left. \frac{d\epsilon_b}{dt} \right|_{damping} + \left. \frac{d\epsilon_b}{dt} \right|_{QE} + \left. \frac{d\epsilon_b}{dt} \right|_{OA} + \sum_i \left. \frac{d\epsilon_b}{dt} \right|_i = 0 \quad (2.93)$$

The contributions to the equilibrium emittance from time-varying sources will therefore add linearly. Using the damping rate from Eqns. 2.61 and 2.63:

$$\delta\epsilon_b^i = \frac{1}{2} \frac{T_0 E_0}{U_0 J_b} \left. \frac{d\epsilon_b}{dt} \right|_i \quad (2.94)$$

The two sources of time-varying modulation considered here are kick modulation and RF voltage modulation.

2.13.1 Kick Modulation

Time-varying kicks can arise in a number of places. Feedback systems which are malfunctioning can impart undesired kicks on the beam. Similarly, magnet power supplies with insufficient filtering or inductance may also contribute.

For a kick modulating with an RMS of θ_{RMS} , the contribution to the emittance growth rate is:

$$\left. \frac{d\epsilon}{dt} \right|_{\theta} = \frac{1}{2} f_0 \beta_0 \theta_{RMS}^2 \quad (2.95)$$

where $f_0 = 1/T_0$ is the revolution frequency, and β_0 is the beta function evaluated at the kick location.

2.13.2 RF Modulation

If the RF voltage varies with time, the contribution to the emittance growth rate for a highly relativistic beam will be:

$$\left. \frac{d\epsilon}{dt} \right|_{RF} = \frac{1}{2} f_0 \langle \mathcal{H} \rangle \frac{e^2 V_{RMS}^2}{E_0^2} \quad (2.96)$$

where $\langle \mathcal{H} \rangle$ is the average over all RF cavities, V_{RMS} is the RMS voltage noise, and E_0 is the beam energy. The dependence on \mathcal{H} implies that this term will not contribute to vertical emittance dilution in a lattice without vertical dispersion. However, as the vertical dispersion increases at the RF cavities, so does the sensitivity to this growth rate.

2.14 Dynamic Aperture

Stored particles are lost when they strike a physical aperture, such as the vacuum chamber which contains the beam. The vacuum chamber aperture is typically many tens of σ 's compared to the beam size, and does not typically contribute directly to beam lifetime. However, particles also see a “dynamic aperture” which defines the maximum on-energy phase space amplitude a particle may have before it is lost due to single-particle nonlinear dynamics. A large dynamic aperture is required in order to minimize particle loss, and therefore maximize beam lifetime.

The dynamic aperture is typically limited by nonlinear effects from chromatic focusing in sextupoles, and in practice can be increased through clever manipulation of the sextupole distribution to tens of σ 's with respect to the beam size.

CHAPTER 3

CESRTA - OVERVIEW

Contributions to vertical emittance fall into two categories: single-particle effects and collective effects. The former includes misalignments and field errors, as well as time-dependent variation of the optics (as discussed in Sections 2.12– 2.13), and choice of optics correction procedures. The latter includes the electron cloud effect, where synchrotron radiation striking the vacuum chamber creates photoelectrons which are attracted to a stored positron beam, and intra-beam scattering, where particles within a bunch hard-scatter to increase the emittance. Correction of single-particle effects and mitigation for collective effects are both necessary in order to achieve the small vertical emittance required by modern storage rings, and in particular for the International Linear Collider (ILC) damping rings.

The Cornell Electron/positron Storage Ring (CESR) was reconfigured in 2008 for low-energy, low-emittance operations as a Test Accelerator for the ILC damping rings. The principle tasks of the CesrTA program are to determine the efficacy of emittance correction procedures for single-particle effects and mitigation techniques for collective effects proposed for the ILC damping rings. In this chapter, the requirements and optics design of CesrTA are discussed.

3.1 CESR Overview

CESR is an electron/positron storage ring, 768 m in circumference. Parameters for the CESR ring are shown in Table 3.1.

CESR was originally designed as a high-energy physics electron/positron

Parameter	Value	Units
Circumference	768.4	[m]
Circulation Time	2.56	[μ s]
Energy	2.085 (1.5-5.3)	[GeV]
Lattice Type	FODO	
Symmetry	\approx Mirror	
H / V Steerings	55/58	
Quadrupoles	105	
Skew Quadrupoles	27	
RF Cavities	4	
Max. Total RF Voltage	8	[MV]
Damping Wigglers	12	
Wiggler B_{max}	1.9	[T]
Position Monitors	100	

Table 3.1: Parameters of the CESR electron/positron storage ring.

colliding-beam storage ring, and as such, it is unique among modern storage rings in several respects.

Dual-Species Operation

CESR is one of only a few storage rings capable of storing electrons or positrons, or both simultaneously, in the same ring. This allows for a direct comparison of beam dynamics between electrons and positron in identical machine conditions. This ability is crucial for characterizing species-dependence for collective effects.

Flexibility of CESR Optics

The magnet layout in most storage rings has a high level of periodicity, repeating a basic cell many times throughout a lattice. There are several reasons why this is desirable. A highly-periodic lattice helps to average out resonances oc-

curing from alignment errors. Additionally, many insertion devices such as wigglers and undulators for light sources have the similar requirements for the storage ring optics where they are located. A highly-periodic lattice enables many beamlines to have the same optics parameters at a regular interval around the ring.

However, the cell designs used at light sources are strongly optimized for one mode of operation, and limit the flexibility of the optics. The CESR lattice on the other hand lacks any low-order symmetry– the nearest symmetry is approximately mirror-symmetric. This lack of symmetry enables CESR to manipulate the optics functions at specific locations in the ring to aid in characterizing beam conditions without requiring the optics to change globally.

Because they are highly periodic, many storage rings gang quadrupoles and sextupoles into families, where all magnets in one family run on the same power supply. This simplifies the design, though it again limits the flexibility of allowing one cell to have different focusing from another. In CESR, all quadrupole and sextupole magnets are independently powered, further enabling localized changes to the optics.

Most light source storage rings are intended to operate at a fixed energy, with limited ability to vary. CESR operated as a collider, and as such it was designed to have a broad energy reach, from 1.5-5.3 GeV in normal operations. A large energy reach is required in colliders in order to scan over resonances for particle production. This also allows for characterization of the energy scaling of various effects.

Damping Wigglers

CESR is equipped with twelve superconducting damping wigglers [23,24]. Parameters for the damping wigglers are summarized in Table 3.2.

Parameter	Value	Units
# Poles	8	[-]
Wiggler Period	40	[cm]
Pole Width	20	[cm]
Pole Gap	7	[cm]
Beam Pipe Aperture (H)	9	[cm]
Beam Pipe Aperture (V)	5	[cm]
B^{max}	2.1	[T]
Field Rolloff at $x = \pm 20$ mm	1%	[%]

Table 3.2: Parameters of the CESR damping wigglers.

The damping wigglers were originally designed and installed for CESR-c collider studies, in order to reduce the damping time and increase the horizontal emittance to increase luminosity (as per Eqn. 1.4). The final design was a compromise between energy spread, damping time, horizontal emittance, and cost [25]. Two-beam colliding conditions mandated that the beams be electrostatically separated everywhere except at the interaction point, inducing a “pretzel orbit” tens of millimeters in amplitude. Because of this large-amplitude orbit, the transverse field quality of the damping wigglers was required to be very high, with less than a 1% field rolloff across a region of $x = \pm 20$ mm. It is because of this high field quality, in addition to the maximum field strength, that the CESR-c damping wigglers were chosen as the basis for the ILC damping ring wigglers.

The maximum peak field of the damping wigglers is 2.1 T, over twenty times stronger than the dipoles (0.08 T). At low energy (2.085 GeV), this means ra-

radiation emission is heavily dominated by the damping wigglers. Following Equation 2.64, the ratio of power emitted from wigglers and dipoles scales as $I_2^{\text{wigglers}}/I_2^{\text{dipoles}}$. For CESR standard low-energy conditions (2.085 GeV, with $B_{\text{peak}}^{\text{wig}} = 1.9$ T and $B_{\text{dipole}} = 0.08$ T) the 12 damping wigglers account for approximately 90% of the energy lost per turn. Per Eqn. 2.62, the increased energy loss reduces the damping time from around 500 ms without wigglers to 50 ms. Additionally, by Eqn. 2.75, it is clear that the damping wigglers dominate the energy spread at 2.085 GeV, contributing approximately 75% of σ_E/E .

3.2 CEsrTA Objectives

The significant flexibility of the CESR optics and the unique opportunities presented by the CESR-c damping wigglers and the ability to store either species demonstrate that CESR is an ideal testbed for damping ring research. To this end, after high-energy physics operation concluded, the CESR ring was reconfigured to CESR Test Accelerator (CesrTA) [2–5]. The objectives of the CesrTA project are to characterize effects which limit the vertical emittance achievable in damping rings.

Low-Emittance Tuning

As will be shown in Chapter 7, optics correction methods have been developed at light sources in the past decade which have enabled demonstration of vertical emittances better than that required by the ILC damping rings [11, 14]. However, the time required for beam-based measurements in these methods scales linearly with the number of components in the ring, making them prohibitively

slow at large rings like the proposed 3.2 km ILC damping rings. The objective at CEsrTA is to demonstrate a vertical emittance correction technique which:

1. Has a fast turnaround time, in order to enable iteration of corrections.
2. Scales well to large rings such as the ILC damping rings.
3. Reliably produces vertical emittance ≤ 10 pm with rapid convergence.

The details of the technique developed at CEsrTA will be discussed in Section 7.2.

Characterize the Growth and Mitigation of Electron Cloud

When synchrotron radiation strikes the vacuum chamber, photoelectrons are emitted. In a positron storage ring the photoelectrons will then be attracted toward the stored beam, inducing additional focusing and instabilities. At CEsrTA methods for electron cloud mitigation have been explored, including coatings for the beam chamber walls, solenoids for pinning the field to the wall, and clearing electrodes [26].

Characterize emittance growth due to intra-beam scattering (IBS)

Particle scattering within a bunch creates an abrupt change in individual particles' momenta. When this scattering occurs in horizontally-dispersive regions, horizontal emittance growth occurs. If it occurs in regions with vertical dispersion or coupling, vertical emittance growth occurs. This mechanism for emittance growth is called intra-beam scattering (IBS). The goal for CEsrTA is to

characterize emittance growth due to IBS, and to demonstrate the validity of existing IBS models [27].

3.3 CesrTA Lattice Design

The objectives laid out in the proceeding section define constraints on the optics for CesrTA. In the interest of brevity, only emittance-related requirements of the CesrTA layout will be discussed. The design vertical emittance is only determined by the finite opening angle of radiation, as shown in Eqn. 2.69. Therefore, only the horizontal emittance constraints must be optimized.

In order for emittance studies at CesrTA to be relevant to the ILC damping rings, the lattice must have a horizontal emittance similar to that of the ILC. The damping time should also be similar to the ILC damping rings, and the synchrotron radiation emission should be dominated by damping wigglers. From a pragmatic standpoint, preference was given to a layout which relies only on preexisting magnets, and minimizes the number of magnets to be relocated.

The final layout chosen involves locating the twelve superconducting damping wigglers to regions where the horizontal optics can be constrained to have zero dispersion. In doing so, the \mathcal{H} functions are minimized in the wigglers, and (per Eqn. 2.70) the equilibrium horizontal emittance is reduced. For six of the wigglers this required no relocation, as it was possible to constrain the dispersion where they were previously located in the arcs. For the remaining six wigglers, a relocation was necessary. To minimize the distance cryogenics lines would have to travel the L0 region was chosen, namely in the center of where the former CLEO detector sits. This required removing the drift chamber of the

CLEO detector and routing a girder through the center of the calorimeter.

A global increase in horizontal focusing, corresponding to a reduction in β_a and γ_a everywhere, also reduces \mathcal{H}_a in the dipoles, where the remainder of the synchrotron radiation is emitted. This corresponds to an increase in the horizontal tune, and further reduces the equilibrium horizontal emittance. From CESR-c to CesrTA conditions, the horizontal integer tune was increased from 10 to 14.

The layout of the final CesrTA lattice is shown in Figure 3.1. Three wigglers are located at 18W and 18E, and six wigglers reside in the L0 straight. Additional instrumentation for electron cloud diagnostics has been installed in the opposing straight in L3.

Parameters for low-energy conditions are summarized in Table 3.3, and the optics functions are shown in Figure 3.2.

Parameter	Value	Units
Energy	2.085	[GeV]
ϵ_x	2.6	[nm]
ϵ_y	< 20	[pm]
$Q_{x,y}^{int}$	(14, 9)	[-]
$\langle \beta_{x,y} \rangle$	(16.3, 20.4)	[m]
$\langle \eta_x \rangle$	0.8	[m]
Damping Time	50	[ms]
Energy Loss/Turn	189.2	[keV]
Bunch Length	11	[mm]
σ_E/E	8.1×10^{-4}	[-]
α_p	6.8×10^{-3}	[-]

Table 3.3: Parameters of the CesrTA lattice.

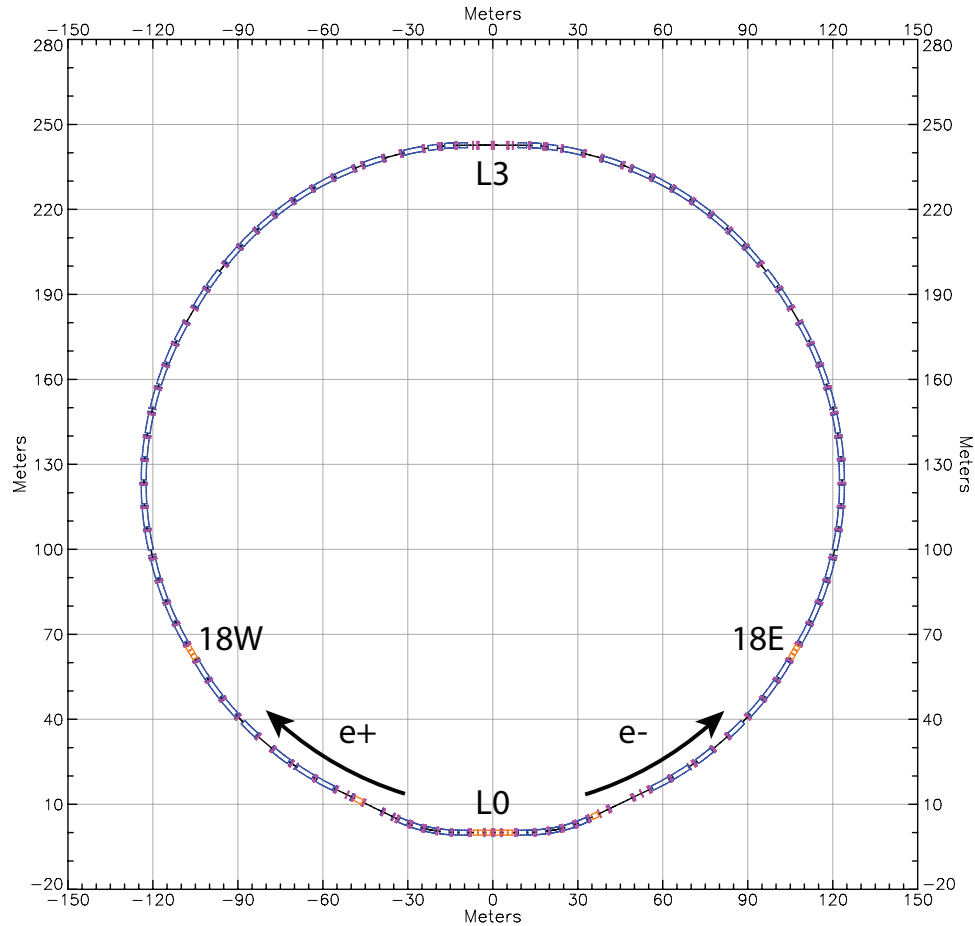


Figure 3.1: Layout of the CEsrTA storage ring. Six damping wigglers are located at L0, and three each at 18W and 18E, for a total of 12. Directions of propagation are indicated for electrons and positrons.

3.4 Survey and Alignment at CEsrTA

As was discussed in Section 2.12, the primary contributions to vertical emittance dilution are tilted and vertically-offset quadrupoles, and dipole rolls. Without beam-based corrections of orbit, dispersion and coupling, the vertical emittance would be limited by the quality of survey and alignment.

The measured distributions of surveyed quadrupole and dipole offsets and tilts for CESR are shown in Figure 3.3. The root mean square (RMS) of magnet

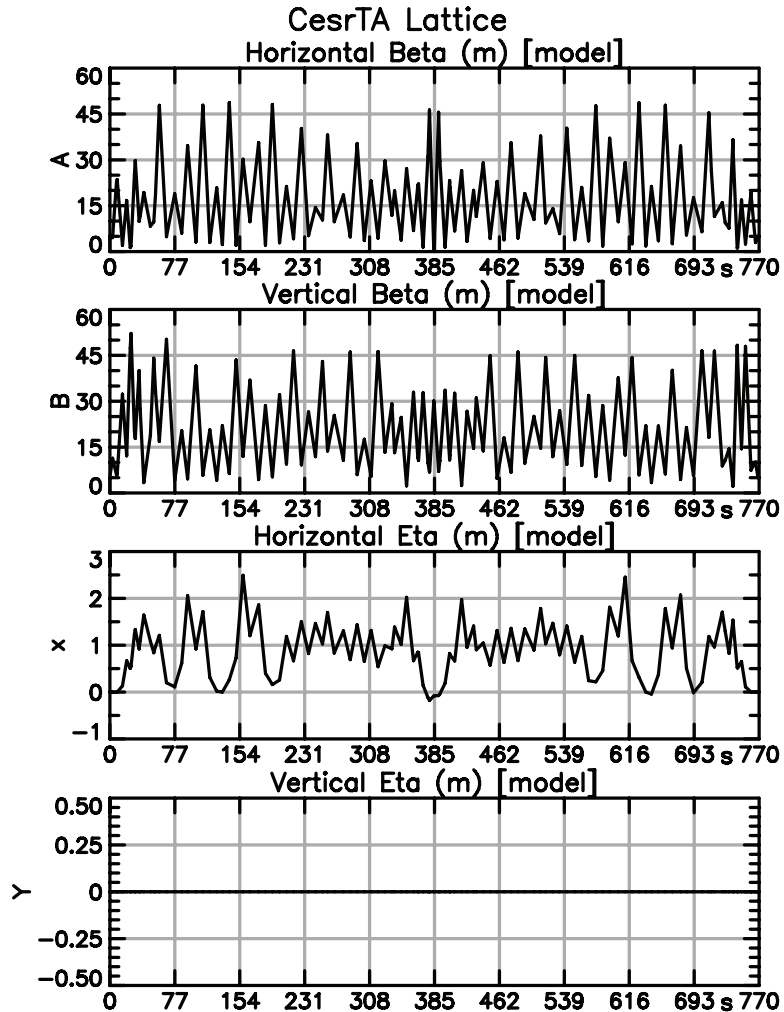


Figure 3.2: Beta functions and horizontal dispersion for the CesrTA storage ring. Note that the plot wraps around at 768.4 m = 0 m. Damping wigglers are located in regions of zero dispersion, at $s = 761 - 7$ m (L0), $s = 127 - 132$ m (18W), and $s = 636 - 641$ m (18E), all regions of zero horizontal dispersion.

alignments are summarized in Appendix E, and include an estimated $100 \mu\text{m}$ uncertainty in the displacement of the magnetic center from geometric center of focusing magnets.

Simulations using random distributions of magnet errors consistent with the measured alignments summarized in Appendix E have been used to study the effect of these errors on the vertical emittance. The method of simulation will

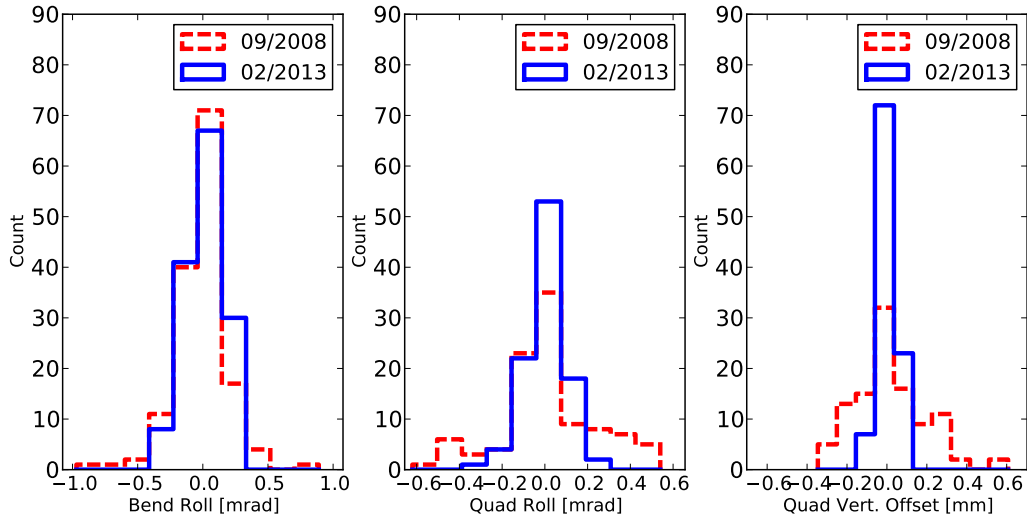


Figure 3.3: Survey and alignment results for CesrTA as of December 2012 CesrTA run, compared to alignment in September 2008 at the start of the CesrTA program. Left to right: dipole roll, quadrupole tilt, and quadrupole vertical offset.

be discussed in Chapter 8. Repeating for 100 random sets of magnet errors, the resulting distributions of emittance, dispersion, and coupling yield statistical information about the probability of achieving the target emittance, and are shown in Figure 3.4.

Relying solely on the geometric alignment of guide field magnets, simulations show that out of 100 random seeds, only three yielded the target vertical emittance of ≤ 10 pm; the mean vertical emittance of the 100 seeds is 104 pm. It is evident that the survey and alignment techniques used are insufficient by themselves to reach the CesrTA emittance target. Some form of beam-based correction is clearly required in order to achieve and maintain low-emittance operating conditions.

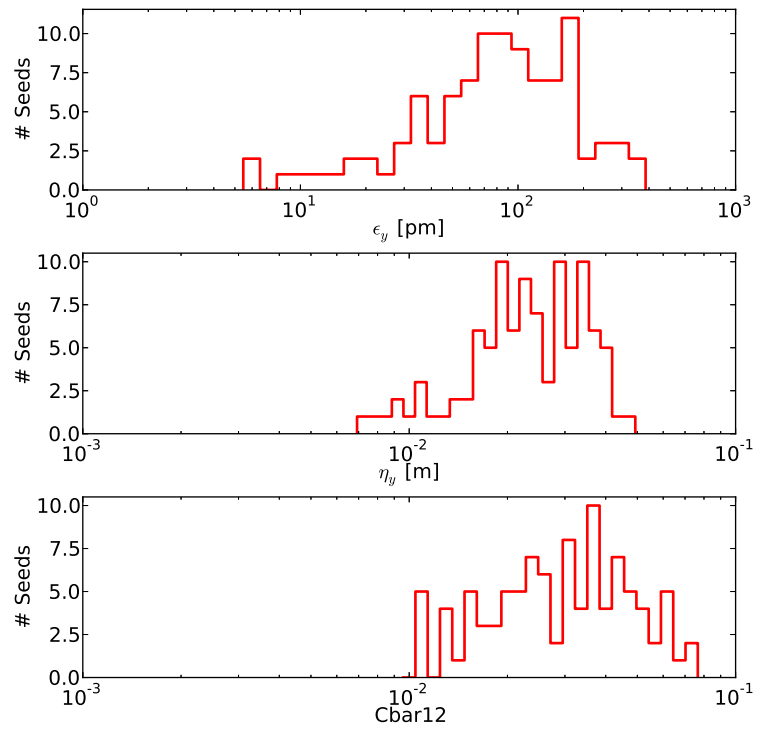


Figure 3.4: Resulting distributions of vertical emittance, vertical dispersion, and coupling when applying errors at the RMS amplitudes specified in Appendix E.1.

CHAPTER 4

INSTRUMENTATION

From Section 3.4, it is clear that survey and alignment are necessary but by themselves are insufficient for achieving the vertical emittance goal of 10 pm at CEsrTA. Corrector magnets, such as steerings and skew quadrupoles, must be powered in such a way as to counteract the residual optics errors which cannot be corrected by magnet alignment alone.

In order to calculate the necessary corrections, measurements must be made of the beam conditions in the accelerator. The measurement methods themselves will be discussed in Chapter 5, and the techniques for deriving corrections from measurements (called low-emittance tuning, or optics correction) will be covered in Chapter 7. First, the instrumentation required to measure beam conditions must be introduced.

The three components of the instrumentation system covered here are the beam position monitors (BPMs), tune trackers, and x-ray beam size monitors (xBsMs).

4.1 BPM System

Beam position monitors (BPMs) are used to collect data for most beam-based optics characterization techniques used in emittance tuning at CEsrTA. A BPM is comprised of four electrodes, or buttons, symmetrically placed around a beam chamber at a fixed location in the ring. CESR is instrumented with 100 BPMs, illustrated in Figure 4.1.

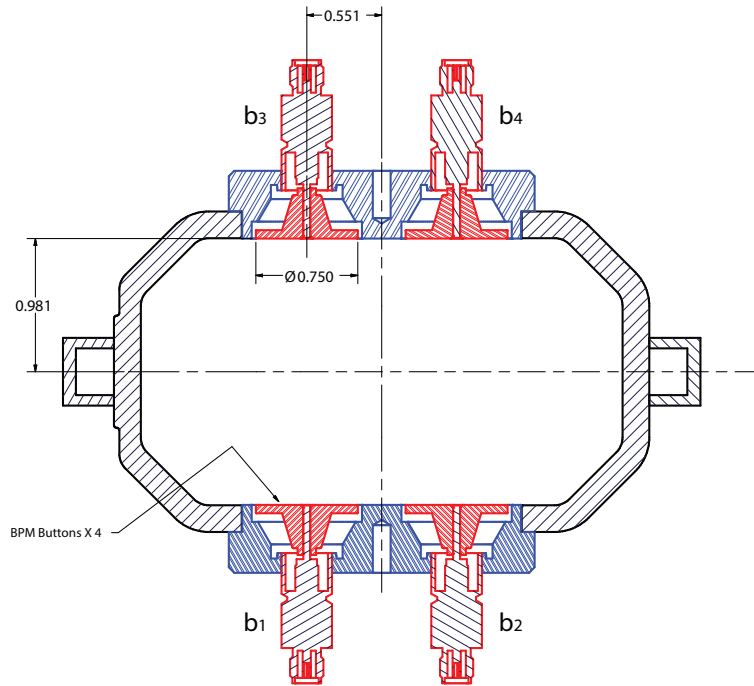


Figure 4.1: Cross-section of a CESR BPM. Dimensions are in inches. The conventional indexing at CESR for buttons is $b_1 - b_4$, where b_1 is bottom-left, b_2 is bottom-right, b_3 is top-left, and b_4 is top-right.

A stored beam creates a potential which is then sampled by the four buttons on the vacuum chamber wall. The CESR BPM electronics are timed such that each BPM records the peak signal generated during a bunch passage. This style of BPM is called a peak-detection BPM. The CESR BPM system utilizes processing electronics developed in-house and is capable of bunch-by-bunch, turn-by-turn readout for bunch spacings of ≥ 4 ns [28].

Many modern lightsource BPMs take four signals into one controller that pre-processes the raw signals into horizontal and vertical data. This design is straightforward, and simplifies the post-processing necessary to reconstruct beam conditions. However, by converting from four button signals to an x and y position and an intensity I , information is lost. Additionally, by bringing all four signals into one processor, there will inevitably be cross-talk between the

channels prior to digitization, degrading the signals.

CESR BPMs have four separate controller cards, one for each button, which are read out independently. This allows for greater flexibility in measurements and post-processing, and minimizes channel-to-channel crosstalk. Bunch-to-bunch cross-talk is below 4% after 4ns, and is effectively zero after 50ns; there is no turn-to-turn cross-talk. Shot-to-shot single-turn orbit reproducibility is approximately 10 μm . The BPM system has a buffer of approximately 300,000 bunch-turns. Depending on the user's request for data, some level of pre-processing is done onboard the BPM electronics before committing data to file, or the raw bunch-by-bunch turn-by-turn button signals are written directly to file.

4.2 Tune Trackers

Several measurement and analysis techniques used at CEsrTA require the beam to be resonantly excited to large amplitude (several millimeters) while recording turn-by-turn data with the BPM system. Phase measurements (Section 5.3) and BPM gain calibrations (Section 6.2) are two examples, and will be discussed later.

One method for exciting the beam is to “ping” the beam with a fast kicker on a single turn. The beam will then oscillate around the closed orbit at the betatron tunes until it is damped. However, particles at different amplitudes will experience different focusing due to sextupoles, causing the bunch distribution to “smear out” over a much larger cross-section compared to its initial size. BPMs are only capable of measuring the bunch centroid, so once the bunch loses its

coherence, all BPM measurements will appear as though the beam were on the closed orbit and no longer oscillating. In practice, with a chromaticity near zero, a few thousand turns may be recorded. Even over these few thousand turns the betatron tunes will vary slightly from turn to turn, making analysis difficult.

If more turns are necessary the bunch must be resonantly excited at the betatron tunes on a turn-by-turn basis, without allowing the particles within the bunch to oscillate at drastically different tunes. This can be accomplished through use of a “tune tracker,” a phase-locked feedback system designed to drive the beam resonantly [29]. If the tunes vary from turn to turn due to amplitude-dependent tuneshift or other effects, the drive remains phase-locked and will report an accurate instantaneous measurement of the tunes.

4.2.1 System Overview

The tune trackers are based on a phase-locked loop (PLL) to lock to the resonant frequency of the beam. This is the same principle of a feedback system, except rather than damping oscillations the tune trackers resonantly excite them. A conceptual illustration of the tune tracker setup is shown in Figure 4.2. A beam position monitor in the storage ring acts as a “pickup,” determining the horizontal and vertical location of the bunch on a single turn. This information is sent to the processing hardware which, depending on the phase advance between the pickup and a stripline kicker, determines what voltages to apply to the stripline such that the amplitude of the bunch centroid oscillation is increased until it reaches an equilibrium over many turns. The voltage is applied as a fast pulse which affects only the single bunch targeted for excitation.

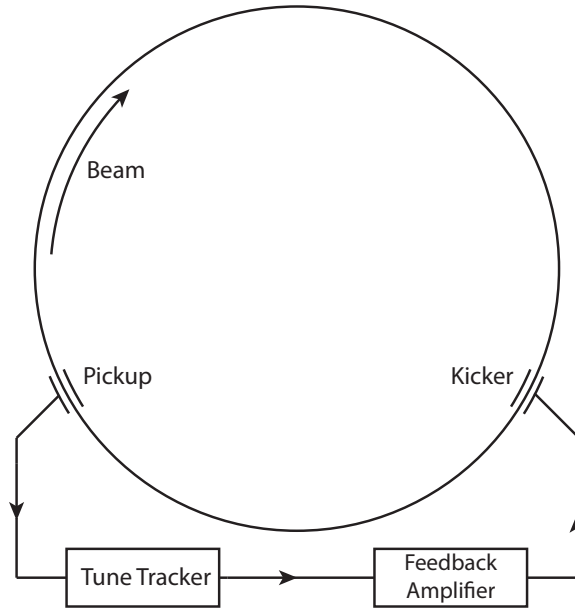


Figure 4.2: Conceptual illustration of the tune tracker setup used at CESR.

Betatron phase and coupling measurements (discussed in Sec. 5.3) require a running sum to be recorded on the BPM modules, where the button signals are compared to the phase of the drive signals. This could be done as a post-process analysis, however it is faster to perform the calculations onboard the distributed BPM modules. The reference phases for the tune trackers are propagated through the timing system by encoding the signals within the BPM clock signal. Appendix A discusses how this is accomplished.

4.3 X-Ray Beam Size Monitor

One of the most straightforward methods for measuring the vertical emittance is to measure the vertical beamsize. The vertical beamsize for an arbitrarily-coupled beam is given by Eqn. 2.89. Assuming the beam is well-decoupled, a safe assumption in low-emittance conditions where the emittance coupling is

below 0.5%, this simplifies to:

$$\sigma_y = \sqrt{\beta_y \epsilon_y + \left(\eta_y \frac{\sigma_E}{E}\right)^2} \quad (4.1)$$

β_y and η_y can be derived from measurements of the machine, as will be discussed in Chapter 5. The energy spread σ_E/E is a property of the lattice design, calculated by Eqn. 2.75, and is a known quantity. Therefore, if the beam size is measured, the emittance can be inferred. For $\beta_y = 40$ m and $\epsilon_y = 10$ pm, and assuming no vertical dispersion, Eqn. 4.1 yields $\sigma_y = 20$ μ m.

The beam size monitor is required to have the ability to image the beam on a bunch-by-bunch, turn-by-turn basis, for several reasons. First, by fitting the beam profile turn-by-turn enables beam motion to be removed from the observed beam size. Second, bunch-by-bunch capability allows for characterizing emittance growth down a train of bunches. Third, turn-by-turn imaging enables more advanced diagnostics such as an FFT of the beam size or centroid motion over tens of thousands of turns.

Beam imaging methods depend on the spectrum of photons measured. There are many factors advocating for imaging the beam using x-rays rather than lower-energy spectra such as visible light:

- **Flux:** Having sufficient flux to image a bunch on a single pass is difficult. For a beam energy of 2.085 GeV, the spectrum of synchrotron radiation produced by a CESR dipole is maximal around $E_\gamma \approx 2$ keV, indicating the largest flux is in the x-ray spectrum. Additionally, optical elements originally in the beam line (such as beryllium or diamond windows) sig-

nificantly attenuate low-energy photons, whereas x-rays are mostly unaffected.

- **Optics:** The beam size is measured using direct imaging with a pinhole, therefore the resolution is diffraction-limited. Higher-energy photons will diffract less than low-energy photons, and therefore provide better resolution.
- **Signal:** Higher-energy photons will convert to more charge when striking a semiconductor detector, providing a larger signal for the same photon flux. This eases the requirements of the electronics and signal processing.

For these reasons, the vertical beam size monitors at CEsrTA operate in the x-ray spectrum.

4.3.1 System Overview

CESR is instrumented with two x-ray beam size monitors (xBsMs), one for each species [30,31]. The xBsMs are one-dimensional 32-diode arrays with a pixel width of $400\ \mu\text{m}$, and pixel pitch of $50\ \mu\text{m}$. The instruments are capable of bunch-by-bunch, turn-by-turn measurements with a buffer of 250,000 bunch-turns. Dynamic range for the instruments span beam currents $0.25 - 10\ \text{mA} = 0.4 - 16 \times 10^{10}/\text{bunch}$ at the standard CEsrTA operating energy of 2.085 GeV. A schematic of the xBsM setup is shown in Figure 4.3.

When characterizing low-emittance conditions, the beam is imaged using a one-dimensional horizontal slit, which acts as a pinhole in the vertical dimension. The effective pinhole diameter D is determined by [32]:

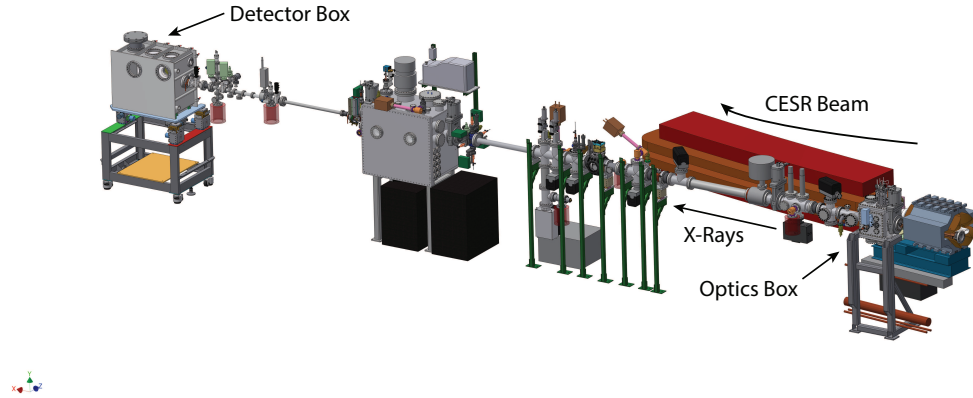


Figure 4.3: xBSM beam line setup at CEsrTA.

$$D \approx 2 \sqrt{\frac{1}{2} f \lambda} \quad (4.2)$$

where f is the distance from the optic to the imaging sensor. For x-rays with $E_\gamma = 1 - 10$ keV ($\lambda_\gamma \approx 0.1 - 1$ nm), and an optic-to-detector distance of roughly 4 m, $D \approx 50 \mu\text{m}$.

In practice, the smallest beam size which can be resolved using the pinhole optic is around $10 - 15 \mu\text{m}$, corresponding to $\epsilon_y \approx 2.5 - 5.5$ pm. Beam size is determined by fitting to the beam profile over a minimum of 1024 turns on a turn-by-turn basis, then averaging. In this way any effect of turn-by-turn centroid motion from the measured beam size is removed.

4.3.2 Reference Orbit and Source Point

The x-ray beam lines at CESR are aligned to a non-zero orbit to accommodate off-axis counter-rotating beams during light source operation. As such, a non-

zero reference orbit is required in order to project light down the beam lines for the xBSMs. The reference orbit is on-axis everywhere except a small region around the beamline source point. An example reference orbit is shown in Figure 4.4.

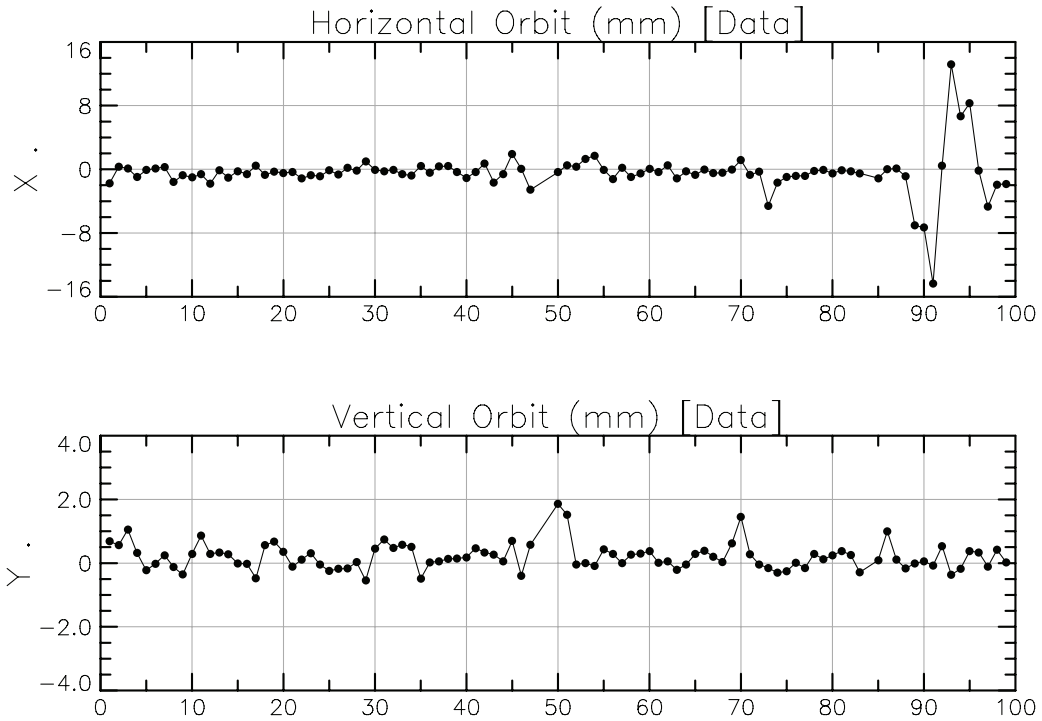


Figure 4.4: A reference orbit for the D-line xBSM. The source point for the beam line is between BPMs 94 and 95. Note the horizontal and vertical scales differ.

The location of the source point within the dipole will determine the source-to-optic distance, which in turn defines the magnification. The calculations and analysis of sensitivity to errors are summarized in Appendix B. Resulting distances and magnifications for C-line and D-line (used for imaging electrons and positrons, respectively) are summarized in Table 4.1.

Beamline	Source-Optic [m]	Optic-Detector [m]	Magnification
C-line	4.4896	10.6211	2.3657 ± 0.0043
D-line	4.6313	10.0117	2.1640 ± 0.0038

Table 4.1: C-line and D-line parameters for optical distances, using survey results and CESR orbitry. These are valid for use in analysis of data from December 2012 and newer.

CHAPTER 5

MEASUREMENT TECHNIQUES

Using the instrumentation described in Chapter 4, measurements of the optics functions can be made in order to determine how the corrector magnets should be powered in order to minimize contributions to the vertical emittance from residual optics errors. The vast majority of measurements of the lattice optics utilize the beam position monitor (BPM) system (see Section 4.1 for details). The primary forms of BPM data used in optics correction are closed orbit, dispersion, and betatron phase and coupling. Methods for determining corrections from these measurements will be discussed in Chapter 7.

5.1 Closed Orbit

The closed orbit at each BPM is measured by averaging button signals over 1024 turns of turn-by-turn bunch trajectory data onboard the BPM modules. Following the indexing in the caption of Figure 4.1, the linearized position measurements can be written as a "difference over sum":

$$x \approx k_x \frac{(b_2 + b_4) - (b_1 + b_3)}{b_1 + b_2 + b_3 + b_4} \quad (5.1)$$

$$y \approx k_y \frac{(b_3 + b_4) - (b_1 + b_2)}{b_1 + b_2 + b_3 + b_4} \quad (5.2)$$

where $k_{x,y}$ are geometric factors, determined by the geometry of the beam pipe. For CESR beam pipes this is a valid approximation for small amplitudes (a few millimeters or less). Larger amplitudes will cause a "pincushion" distortion, which must be corrected using a nonlinear response map [33].

A closed orbit measurement takes roughly 5 seconds, with measurement reproducibility of around 10 μm .

5.2 Dispersion

Through the momentum compaction factor α_p (Eq. 2.73) and the harmonic number h (Eq. 2.72), there is a known relationship between a change in RF frequency and a change in the energy:

$$f_{RF} = \frac{1}{C} \times \frac{c_{light}}{h} \quad (5.3)$$

$$\frac{\Delta f_{RF}}{f_{RF}} = \frac{1}{\Delta C/C} \quad (5.4)$$

$$= \alpha_p \frac{1}{\Delta E/E} \quad (5.5)$$

That is, a change in RF frequency corresponds linearly to an inverse change in the beam energy. This provides a convenient method for measuring the dispersive trajectory.

The dispersion functions are measured by varying the RF frequency by a known amount and measuring the change in closed orbit. A standard dispersion measurement at CESR varies the 500 MHz superconducting RF cavities by ± 2 kHz (corresponding to $\delta_E/E = 5.9 \times 10^{-4}$) and takes several minutes to acquire. Most of the required time is due to varying the RF frequency. The measurement reproducibility is better than 1 mm.

5.3 Betatron Phase and Coupling

Quadrupole focusing errors and coupling errors are determined by measuring betatron phase advance, using turn-by-turn data acquired while resonantly exciting the beam [34].

Resonant excitation is achieved by phase-locking a pair of tune trackers, described in Section 4.2, to the horizontal and vertical betatron tunes. The tune trackers then excite the beam to amplitudes of several millimeters. 40,960 consecutive turns of data are acquired, where on each turn the button response is compared to the phase of the tune tracker by processors onboard the BPMs. The button-by-button phase and amplitude are then post-processed into horizontal and vertical phase, the out-of-phase component of the coupling matrix \bar{C}_{12} , and the two in-phase components of the coupling matrix $\bar{C}_{22,11}$.

All of the above information is determined from one measurement of the machine. Betatron phase and coupling measurements take roughly 10 seconds per measurement. Reproducibility of betatron phase measurements is of order 0.1 deg.

Phase and coupling measurements are a more sophisticated method than orbit and dispersion measurements, and require further background to understand how raw button signals are processed into usable data. This is discussed in Appendix C.

5.4 Turn-by-Turn Data

The BPM system can be operated in a true bunch-by-bunch, turn-by-turn mode for bunch spacings ≥ 4 ns, and a buffer of approximately 300,000 bunch-turns. The shot-to-shot reproducibility of turn-by-turn data is around $10 \mu\text{m}$.

Turn-by-turn data is used during calibration of the BPM system, namely in determining detector rotation and button-to-button gain variations. These procedures will be discussed in Chapter 6.

CHAPTER 6

BEAM POSITION MONITOR CALIBRATIONS

BPM systematics must be understood in order to measure machine characteristics with the requisite precision to achieve low-emittance conditions. The primary characteristics to consider are: button-by-button timing, button-to-button relative gains, BPM tilts, and BPM-to-quadrupole transverse offsets. Each of these is now discussed in the order they are evaluated.

6.1 Button-by-Button Timing

Each controller card has independent timing, therefore every button on every BPM must be timed in separately. A mistimed channel results in sampling the bunch passage off-peak, which reduces the observed signal amplitude for that button. Errors in button timing will affect orbit, dispersion, and in-phase coupling measurements. Betatron phase and out-of-phase coupling measurements have been shown in simulation to be insensitive.

The time-in procedure consists of sampling the temporal profile of a bunch passage at a resolution of 10 ps and fitting to determine the peak. The process takes less than one minute for all four buttons on all 100 BPMs to converge, with less than 10 ps drift over a period of four hours.

6.2 Button-to-Button Relative Gains

Differences in gain between button channels can produce distortions in observed positions on the cross-section of the BPM. In the simplest scenario, a single button gain error will shift all apparent orbits on that BPM toward one quadrant. Multiple gain errors will introduce more complex behavior. Gain errors affect orbit, dispersion, and in-phase coupling measurements, but not betatron phase. For out-of-phase coupling measurements the processing method has shown to be insensitive to gain errors in simulation.

The method of calibrating button gains used at CEsrTA, called “gain mapping,” was developed by Rubin *et al.* at Cornell [35], and is based on a second-order expansion of the button signal response. The method utilizes turn-by-turn data, therefore data acquisition is fast, on the order of several seconds to collect data for characterizing all 100 BPMs. The analysis relies on the fact that a linear relation exists between two combinations of the four button signals. For n turns of turn-by-turn trajectory data there are $4n$ button measurements at each BPM. There are only four unknowns, namely the button gains, and the system is overconstrained for $n > 1$ orbits; typically 1024 turns are used. Data acquisition takes about 10 seconds, and the fitting process takes less than a minute to determine all four button gains on all 100 BPMs.

All gain calibration techniques are sensitive to timing errors, which manifest themselves as an apparent gain error. This method is insensitive to detector rotation or offset, as the method uses raw button signals across a large cross-section of the BPM, and does not rely on distinguishing between horizontal and vertical modes.

Typical BPM gain variations before correction are of order 5%, and are calibrated with a reproducibility of a few tenths of a percent.

6.3 Electronic Centering

A relative offset between the electronic center of a BPM and the magnetic center of its nearest quadrupole will appear in measurements as an offset in the quad, resulting in kicks from the quadrupole when the beam is centered to the electronic center of the BPM. To minimize vertical dispersion (and thus the emittance), the relative offset between the electronic center of a BPM and the magnetic center of the nearest quadrupole must be measured.

BPM-to-quadrupole relative offsets will only affect closed orbit measurements and turn-by-turn trajectory data. Dispersion measurements are a difference of two closed orbits, therefore absolute offsets do not affect the measurement, although real vertical dispersion will be created if the closed orbit is corrected when the offsets have not been measured. Betatron phase and coupling measurements are computed button-by-button, therefore transverse offsets will not affect the measurement.

BPM-to-quadrupole centering is achieved using resonant excitation data [36]. For each BPM/quadrupole pair, two consecutive betatron phase measurements are taken, with two different quadrupole settings. The difference in phase measurements is fit to determine the actual change in quadrupole strength, so that there is no reliance on a current-to-field calibration, which may be inaccurate due to hysteresis.

The closed orbit is measured simultaneously with each phase measurement, and is therefore known before and after the change in quadrupole strength. The difference in closed orbits is fit to determine the kick induced by the quadrupole. The relative offset is then determined from the change in kick to the beam due to the change in strength of the quadrupole. The beam is then shifted toward the center of the quadrupole to improve the accuracy of the measurement, and the calibration is repeated.

Typical BPM-to-quadrupole offset calibrations are around 1mm RMS in both horizontal and vertical, with a resolution of around $170 \mu\text{m}$.

6.4 Tilt Calibration

If a BPM is rotated, a horizontal orbit perturbation will indicate a vertical offset. This becomes particularly significant when measuring the dispersion, as the average design horizontal dispersion in CESR is large, on order 1 m, whereas the design vertical dispersion is zero. A rotated BPM will incorrectly measure some component of the horizontal dispersion as vertical, which will then be used in emittance corrections.

The smallest RMS vertical dispersion recorded in CesrTA conditions is around 12 mm. Simulations have shown that an RMS of 12 mm of actual vertical dispersion corresponds to 15-30 pm vertical emittance. However, as will be discussed in Sec. 7.4, the vertical emittance is routinely measured to be smaller than 15 pm. This suggests that at least some component of the vertical dispersion measurement is due to rotated BPMs. The RMS horizontal dispersion is roughly 1 m, therefore if the BPM tilts are randomly distributed, the largest

anticipated RMS BPM tilt is around 12 mrad.

Two methods for BPM tilt measurement have been developed. The first is based on the in-phase coupling matrix elements $\bar{C}_{22,11}$, and the second uses turn-by-turn data.

6.4.1 Method I: In-Phase Coupling

As previously mentioned, when acquiring betatron phase and coupling data, three of the four elements of the \bar{C} matrix are measured. For coupling corrections only the out-of-phase component \bar{C}_{12} is used, which is insensitive to BPM tilts. When the machine is well-corrected (i.e., \bar{C}_{12} is small), the residual in-phase components $\bar{C}_{22,11}$ will be dominated by BPM tilt errors; the in-phase components can therefore be fit to derive the BPM tilts, which can then be utilized when processing dispersion data. The analytic derivation for how a BPM tilt affects the observed betatron phase and \bar{C} matrix elements is included in Appendix D.

Simulations of this method of BPM tilt calibration suggest that even when including effects of finite measurement resolution and BPM measurement errors the method can determine BPM tilts to within 2.5 mrad. However, fitting machine data has yielded BPM tilts which are inversely correlated with the amplitude of horizontal dispersion, resulting in an RMS fitted BPM tilt of around 20 mrad.

6.4.2 Method II: Turn-By-Turn Trajectory Data

In a machine where the coupling is well-corrected, both the in-phase and out-of-phase components of the coupling matrix will be small. After correcting the out-of-phase coupling \bar{C}_{12} , the observed tilt of the beam ellipse in x - y space will be dominated by observational errors from BPM tilts.

Using this method, the fitted BPM tilts have a distribution with an RMS of roughly 12 mrad, in agreement with the maximum BPM tilt allowed by measurements of the vertical dispersion. However, using these tilts in corrections have not yet yielded any improvement in the vertical dispersion. BPM tilt studies are an ongoing effort.

CHAPTER 7

LOW-EMITTANCE TUNING TECHNIQUES

The measurement techniques described in Chapter 5 allow for characterizing the existing conditions in a storage ring, and the BPM calibrations in Chapter 6 ensure that the measurements accurately reflect the beam properties. This information is utilized for calculating corrections to the optics to bring the storage ring conditions closer to the design parameters. A typical outline of optics correction procedure would be:

1. Measure and correct the closed orbit.
2. Measure and correct the beam envelope (beta functions).
3. Correct contributions to the emittance.

The final step, where the objective of the correction is to specifically reduce contributions to the vertical emittance, is called “emittance tuning.” Methods for emittance tuning differ greatly between accelerators, however the objective is usually the same. From Eqn. 2.68, the equilibrium emittance depends on $I_{5,y}$, which in turn depends on \mathcal{H}_y . Contributions to \mathcal{H}_y are primarily vertical dispersion and coupling.

One could in principle correct these contributions sequentially, however corrections to one function (for example, the coupling) will affect other functions (for example, the dispersion). An ideal correction procedure would address all interdependencies simultaneously.

7.1 Response Matrix Analysis (RMA)

Response Matrix Analysis (RMA) is by far the most common method for optics correction at storage rings. In this method, the “response” of BPMs to changes in corrector magnets is measured. The most widely used implementation of this concept is Linear Optics from Closed Orbits (LOCO) [37], a package developed on the Accelerator Toolbox (AT) platform [38] in MATLAB.

For LOCO, each steering magnet i is varied individually to two settings (typically symmetrically, $-\theta_i$ and $+\theta_i$), taking a closed orbit measurement at all BPMs j for each setting. From each pair of closed orbits, a difference orbit can be computed. One therefore has the “response” of the BPMs to a change in that steering:

$$\frac{d\mathbf{x}_j}{d\theta_i} = \frac{\mathbf{x}_j^{+\theta_i} - \mathbf{x}_j^{-\theta_i}}{2\theta_i} \quad (7.1)$$

where $\mathbf{x}_j^{\pm\theta_i}$ are the closed orbits at BPM j for steering strengths $\pm\theta_i$. Repeating for all N BPMs and M steerings, this information can be consolidated into a response matrix \mathbf{M}^{ORM} . This response matrix determines the change in the closed orbit at all BPMs due to a change in an arbitrary linear combination of changes in steerings:

$$\Delta\mathbf{x} = \mathbf{M}^{ORM}\Delta\boldsymbol{\theta} \quad (7.2)$$

$$\begin{pmatrix} \Delta x_1 \\ \Delta x_2 \\ \vdots \\ \Delta x_N \\ \Delta y_1 \\ \Delta y_2 \\ \vdots \\ \Delta y_N \end{pmatrix} = \begin{pmatrix} \frac{dx_1}{d\theta_1} & \frac{dx_1}{d\theta_2} & \dots & \frac{dx_1}{d\theta_M} \\ \frac{dx_2}{d\theta_1} & \frac{dx_2}{d\theta_2} & \dots & \frac{dx_2}{d\theta_M} \\ \vdots & \vdots & \ddots & \vdots \\ \frac{dx_N}{d\theta_1} & \frac{dx_N}{d\theta_2} & \dots & \frac{dx_N}{d\theta_M} \\ \frac{dy_1}{d\theta_1} & \frac{dy_1}{d\theta_2} & \dots & \frac{dy_1}{d\theta_M} \\ \frac{dy_2}{d\theta_1} & \frac{dy_2}{d\theta_2} & \dots & \frac{dy_2}{d\theta_M} \\ \vdots & \vdots & \ddots & \vdots \\ \frac{dy_N}{d\theta_1} & \frac{dy_N}{d\theta_2} & \dots & \frac{dy_N}{d\theta_M} \end{pmatrix} \begin{pmatrix} \Delta\theta_1 \\ \Delta\theta_2 \\ \vdots \\ \Delta\theta_M \end{pmatrix} \quad (7.3)$$

The response matrix \mathbf{M}^{ORM} can also be computed analytically for the design lattice from a computer model. The difference between the measured and design response matrices shows the deviation of the actual machine from that which is intended. A singular-value decomposition (SVD) then extracts the most significant contributions to that difference, and corrector strengths can be determined in order to minimize the largest contributions. This method also determines BPM gain and tilt errors.

A more complete version of this procedure, including dispersion data, is in regular use at SOLEIL [39], the Australian Synchrotron Light Source (ASLS) [40], the Advanced Light Source (ALS) [41], Advanced Photon Source (APS) [42], and several others. The ASLS used this method to achieve a vertical emittance of 1.2 pm in 2010 [11]. Similarly, the Swiss Light Source (SLS) used LOCO as a first stage in achieving a sub-picometer vertical emittance in 2012 [14]. Clearly, this is a very powerful technique.

However, the time required for acquiring data scales linearly with the number of correctors, and data analysis of M BPMs and N correctors scales as $(2M)^2 \times N$ (assuming $2M > N$, a safe assumption in most storage rings). This

scaling is acceptable in a smaller ring such as the ASLS, which has 98 BPMs and 140 correctors (horizontal and vertical steerings, and skew quadrupoles) [43]. The ASLS is unusually fast at acquiring ORM data, requiring roughly fifteen minutes to record a full data set and another five minutes to compute corrections. By comparison, one ORM data set takes around 2.5 hours to acquire at CesrTA.

For a large ring such as the ILC damping rings, with 561 detectors and around 300 correctors, the time required for data acquisition would be over five times longer than the ASLS, and analysis would take approximately 70 times longer. This makes ORM and LOCO prohibitively time consuming to perform on a regular basis at the ILC damping rings. A faster method of emittance tuning is required.

7.2 Combined Coupling and Dispersion Correction

The low-emittance tuning procedure developed at CesrTA takes advantage of the fact that all BPMs are capable of betatron phase and coupling measurements through turn-by-turn acquisition. As described in Section 5.3 (and elaborated on in Appendix C), only one measurement of the machine is necessary to determine the betatron phases and transverse coupling. Most of the processing for these measurements occurs onboard the BPM modules, which greatly enhances the data processing throughput while still returning a detailed characterization of the optics. As such, correction methods utilizing betatron phase and coupling measurements scale easily to any size storage ring.

The emittance correction procedure developed for CesrTA is as follows:

1. Measure the closed orbit and correct to the xBSM reference orbit using all horizontal and vertical steering correctors.
2. Measure the betatron phase, transverse coupling (\bar{C}_{12}), and horizontal dispersion. Fit a model lattice to the measurements, allowing all normal quadrupoles and skew quadrupole correctors to vary, and load the computed corrections.
3. Remeasure the closed orbit, transverse coupling, and vertical dispersion. Fit model lattice to all machine data simultaneously using all vertical steerings and skew quadrupoles, and load the fitted corrector changes.

The turnaround time for one full set of corrections is roughly ten minutes, or about 1/15 the time required to collect an ORM data set at CesrTA.

Lattice corrections are determined by a χ^2 fit of a machine model to measurements of the lattice functions, with a merit function defined as [34]:

$$\chi^2 = \sum_i w_i^{data} \left[\left(d^{measured}(i) - d^{ref}(i) \right) - \left(d^{model}(i) - d^{design}(i) \right) \right]^2 + \sum_j w_j^{var} \left[\left(v^{measured}(i) - v^{ref}(i) \right) - \left(v^{model}(i) - v^{design}(i) \right) \right]^2 \quad (7.4)$$

where $d(i)$ is the i^{th} datum (for example, the vertical orbit at a BPM), $v(j)$ is the j^{th} variable (such as a corrector strength), and $w_{i,j}$ are user-defined weights. Weights are applied to corrector strengths in order to prevent the optimizer from reaching a minimum which requires unrealistic corrector strengths. The merit function is minimized through an optimization algorithm such as Levenberg-Marquardt [44], which adjusts corrector magnets in the model to best match the

measurements such that the correctors in the model will reproduce the measurements. The inverse of the model corrector strengths can then be loaded into the lattice to compensate for optics errors.

To ensure conditions return with minimal effort a hysteresis loop must be established. It is standard procedure when first recovering conditions to save magnet settings after achieving low emittance, run the machine through a hysteresis loop where magnet currents are ramped in a well-defined pattern, then re-load the previously saved conditions and repeat the emittance tuning procedure to apply minor corrections. In general the corrections required after looping are minimal, and a second loop is not necessary to further enforce the reproducibility of low-emittance conditions. The only magnets strongly affected by hysteresis are those used to create the xBSM orbit bump, as described in Section 4.3.2.

A summary of optics functions after a typical low-emittance correction are shown in Table 7.1. The values reported are the RMS of the measurement itself (labeled “data” in the table), and the RMS of the best-fit model to the data (labeled “machine model”).

Measurement	RMS (data)	RMS (machine model)	Units
δy	253	110	[μm]
$\delta\phi_{a,b}$	0.3	0.3	[deg]
$\delta\beta/\beta$	—	0.73%	[%]
η_y	13	5	[mm]
\bar{C}_{12}	0.004	0.003	[—]

Table 7.1: Typical levels of correction for optics measurement after the full emittance tuning procedure. Measurements were taken at 0.8 mA (1.3×10^{10} /bunch), and RMS values are reported for both the machine measurement and a machine model which is fit to the measurements. Beta beat is computed from fitting phase data.

7.3 Calculating Emittance and its Uncertainties

The vertical emittance ϵ_y is computed from measurements of the vertical beam size using the xBSM (Section 4.3). The coupling \bar{C}_{12} is measured to be small, $O[0.003]$, therefore the terms in σ_y from the a -mode (horizontal-like) in Eqn. 2.89 are insignificant and the beam size takes the form of Eqn. 4.1. In practice this is a valid assumption for well-corrected optics.

Modifying Eqn. 4.1 to solve for the emittance:

$$\epsilon_y = \frac{\sigma_y^2 - \left(\eta_y \frac{\sigma_E}{E}\right)^2}{\beta_y} \quad (7.5)$$

The beam size σ_y is related to the measured image at the xBSM σ_{im} by

$$\sigma_y^2 = \left(\frac{\sigma_{im}}{M}\right)^2 - \sigma_p^2 \quad (7.6)$$

where σ_p is the image size at the detector for a point source, projected back to the source point. When the source has finite size, the resulting image on the xBSM detector is a convolution of the point-source response with the finite source size. If both the source and the point response are sufficiently Gaussian, then the width of the final image is approximately the widths of the finite source size and the point response added in quadrature.

Uncertainties in the measurement of the vertical emittance fall into two classes: systematic and statistical. The former are uncertainties which are consistent from one measurement to the next, such as confidence in the method

used to determine the beam size from fitting the xBSM data, and uncertainty in the source point within the dipole. The latter includes parameters which vary from one measurement to the next, for example beam size fluctuation or the reproducibility of measurements of optics functions (β_y, η_y). A proper assessment of the uncertainty in the emittance measurement must account for both systematic and statistical uncertainties.

The uncertainties associated with measurements of vertical emittance with the xBSM were originally outlined in [45], however not all sources of uncertainty were included at the time. The sources of uncertainty fall into two categories:

- **Uncertainty in Beam Size** - The measurement in the beam size itself has both systematic and statistical uncertainties. The former is due to confidence in the procedure used to determine the beam size from the measured image size at the xBSM detector, confidence in the fidelity of the image sampled by the xBSM detector, and confidence in the understanding of the optics used to image the beam. This includes the location of the source point within the dipole and the height of the vertically-limiting aperture used as a pinhole for imaging. The statistical uncertainty is due to shot-to-shot variation in the beam size from variation in the actual beam size and in photon flux.
- **Uncertainty in Lattice Optics Functions** - For a fixed measurement of the beam size, a variation in the optics functions (β, η) will change the resulting emittance. The systematic uncertainty in the optics functions is entirely due to uncertainty in the longitudinal source point, as the optics functions vary along s within the dipole. Statistical uncertainties are due

to fluctuations in the measured optics functions, and are estimated from repeated measurements of the optics.

As always, statistical uncertainties add in quadrature, whereas systematic uncertainties add linearly [46]. The uncertainties therefore propagate as follows:

$$\delta\epsilon_y^{stat} = \sqrt{\left|\frac{\partial\epsilon_y}{\partial\beta_y}\right|^2(\delta\beta_y^{stat})^2 + \left|\frac{\partial\epsilon_y}{\partial\eta_y}\right|^2(\delta\eta_y^{stat})^2 + \left|\frac{\partial\epsilon_y}{\partial\sigma_{im}}\right|^2(\delta\sigma_{im}^{stat})^2} \quad (7.7)$$

$$\delta\epsilon_y^{sys} = \left|\frac{d\epsilon_y}{d\sigma_{im}}\right|\delta\sigma_{im}^{sys} + \left|\frac{d\epsilon_y}{d\sigma_p}\right|\delta\sigma_p + \left|\frac{d\epsilon_y}{ds}\right|\delta s \quad (7.8)$$

where

$$\left|\frac{d\epsilon_y}{ds}\right| = \left|\frac{\partial\epsilon_y}{\partial\beta_y}\frac{\partial\beta_y}{\partial s} + \frac{\partial\epsilon_y}{\partial\eta_y}\frac{\partial\eta_y}{\partial s} + \frac{\partial\epsilon_y}{\partial M}\frac{\partial M}{\partial s}\right| \quad (7.9)$$

and *sys* and *stat* refer to the systematic and statistical uncertainties, respectively. The individual terms $d\epsilon_y/dx_i$ are computed by varying the terms x_i in Eqn. 7.5 by their uncertainties $\pm\delta x_i$. Relevant parameters used in the calculation of the emittance and the propagation of uncertainties are summarized in Table 7.2. Note that for the magnification M and optics functions β , η , the systematic uncertainties are accounted for through $\partial x_i/\partial s$ to emphasize their sole dependence on longitudinal source point in the dipole.

Parameter	Value	Systematic	Statistical	Units
σ_{im}	56.4	± 2.2	± 0.1	$[\mu\text{m}]$
σ_p	17.0	± 2.0	–	$[\mu\text{m}]$
M	2.1629	–	–	[–]
$\partial M/\partial s$	-0.4673	–	–	$[\text{m}^{-1}]$
β_y	42.09	–	± 0.75	[m]
$\partial\beta_y/\partial s$	-9.56	–	–	$[\text{m}/\text{m}]$
η_y	-0.9	–	± 2.0	[mm]
$\partial\eta_y/\partial s$	0.51	–	–	$[\text{mm}/\text{m}]$
δs	–	± 8	± 2	[mm]
σ_E/E	8.125×10^{-4}	–	–	[–]

Table 7.2: Parameter values and uncertainties used for calculating uncertainty in the December 2012 2.085 GeV e^+ emittance measurement. This table is representative of results typically seen in each of the conditions characterized, however every set of conditions where the vertical emittance is measured will have different values for the parameters in this table.

Energy [GeV]	Species	ϵ_y [pm]	$\delta\epsilon_y^{\text{sys}}$ [pm]	$\delta\epsilon_y^{\text{stat}}$ [pm]	Date
2.085	e^+	8.7	$\begin{cases} +2.9 \\ -3.4 \end{cases}$	$\begin{cases} +0.2 \\ -0.2 \end{cases}$	12/2012
2.085	e^+	11.8	$\begin{cases} +3.3 \\ -3.5 \end{cases}$	$\begin{cases} +0.3 \\ -0.2 \end{cases}$	4/2013
2.085	e^-	13.3	$\begin{cases} +3.4 \\ -3.5 \end{cases}$	$\begin{cases} +0.3 \\ -0.3 \end{cases}$	4/2013
2.305	e^+	12.7	$\begin{cases} +3.0 \\ -3.9 \end{cases}$	$\begin{cases} +0.2 \\ -0.2 \end{cases}$	12/2012
2.553	e^+	10.2	$\begin{cases} +2.9 \\ -3.4 \end{cases}$	$\begin{cases} +0.2 \\ -0.2 \end{cases}$	4/2013

Table 7.3: Lowest-achieved emittance at CEsrTA in a variety of energies. Electron conditions are only reported for the April 2013 CEsrTA run at 2.085 GeV.

7.4 Results of Emittance Tuning at CEsrTA

Using the above tuning method, and propagating errors according to Equations 7.7–7.9, results of emittance tuning at CEsrTA are summarized in Table 7.3. For all measurements, bunch current was 0.7–0.9 mA = $1.1 - 1.6 \times 10^{10}$ /bunch.

The measurement for positrons at 2.085 GeV in December 2012 demonstrates the achievement of the CEsrTA Phase II target vertical emittance of 10 pm. Subsequent measurements in near-identical conditions in April 2013 do not reproduce this achievement. There are several reasons why this may be. First, while in December 2012 all four superconducting RF cavities were operational, only three were running in April 2013. This reduced the total RF voltage from 6.4 MV to 4.8 MV, which could have affected the beam size. Secondly, it was observed during the April 2013 machine studies that BPM-to-quadrupole centering did not converge well. Subsequent investigations showed that there were indeed problems with the automated method, which have been addressed after the CEsrTA run ended.

Measurements of the vertical emittance for electrons are consistently larger than for positrons in similar machine conditions. The only difference in the machine optics between electron and positron low-emittance setups is the use of a different closed-orbit bump for alignment to the xBSM beam lines. The discrepancy in emittance measurements is not understood at this time.

7.5 Alternative Emittance Tuning Methods at CesrTA

Several alternative LET tuning methods have been explored. To date, no method has proven to be faster or yield consistently better results than the three-stage correction algorithm based on betatron phase and coupling measurements described in Sec. 7.2.

LOCO analysis was briefly tested at CesrTA [47]. Data acquisition was found to be prohibitively slow (of order two hours or more for a single data set), and the corrector strengths determined by LOCO were nearly identical to those determined by the combined coupling and dispersion corrections already in use.

An alternative to the phase and coupling correction, using turn-by-turn data and developed jointly with A. Wolski [48], was also tested at CesrTA. This method, called “normal-mode analysis,” aims to determine the response of the individual button signals to the normal modes a and b . Starting in an uncorrected lattice this method delivered similar corrections to the nominal coupling and dispersion correction. However, iteration of the coupling and dispersion correction would often further reduce the emittance, whereas the normal mode corrections did not. Further development of this method may result in similar results to that achieved with the coupling and dispersion correction.

CHAPTER 8

EMITTANCE CORRECTION SIMULATIONS

The vertical emittance measurements presented in Section 7.4 demonstrate the best corrections achieved to-date. However, the measured vertical emittance after correction remains two orders of magnitude above the fundamental quantum limit (around 0.1 pm). It is of interest to diagnose what factors are limiting the effectiveness of corrections, and to determine whether it is possible to reduce the vertical emittance further.

In this chapter the methods for simulating optics measurement and correction are discussed, including how BPM measurement errors and guide field magnet errors are modeled. Results of simulations based on input parameters representing the physical accelerator are presented.

8.1 `ring_ma2`

Without beam-based optics corrections, the most significant contributions to the vertical emittance are magnet misalignments and BPM measurement errors. The choice of correction algorithm will also contribute to the final emittance after correction. To evaluate these contributions to vertical emittance, a simulation package has been developed. The program, `ring_ma2`, uses the `Bmad` accelerator code library [22,49], and does the following:

1. Assigns random misalignments and BPM errors with user-defined amplitudes to the ideal lattice to create a realistic machine model.
2. Simulates beam-based measurements of optics functions including the ef-

fects of BPM measurement errors.

3. Computes and applies corrections for each iteration based on the simulated measurements.
4. After each correction iteration, it records the effectiveness of the correction in terms of emittances and optics functions.

The entire procedure is repeated for typically 100 random seeds in order to generate statistics for analysis. The simulation is approached from a statistical perspective for three reasons. First, magnet positions continually drift, making it difficult to know the exact set of misalignments in the ring on any given day. Second, the precise distributions of magnetic centering or BPM measurement errors are not known, mandating that their distributions be approached from a statistical perspective. Third, by framing the analysis in terms of statistical probability of achieving the required emittance, the characterization process may be extrapolated to new machines which are not yet built using only the knowledge of survey and alignment tolerances.

When discussing the results of statistical analysis the 95% confidence levels (CL) are presented. That is, after applying the full optics correction procedure 95% of simulated lattices, each with a randomly chosen distribution of misalignments and measurement errors, achieve a vertical emittance below the 95%CL. The simulation is believed to be sufficiently complete such that it is very unlikely that the contribution of static optics errors to the vertical emittance in the actual machine is greater than this number.

8.1.1 Model Lattice with Errors

`Bmad` allows for introducing strength errors (including systematic and random multipole errors) and alignment errors (such as offset, roll, and pitch) to any lattice element. Magnet strength errors scale with the absolute strength of the magnet. Alignment errors are treated as additive errors, and are applied directly without scaling. In all cases, errors are constrained to be less than 3σ , as any errors larger than this would be isolated and rectified.

`ring_ma2` also models BPM measurement errors, which are discussed in detail in Section 8.1.3.

8.1.2 Simulated Measurements

All simulated measurements are modeled as realistically as possible. For closed orbit measurements this involves recording 1024 turns of trajectory data, including the effects of BPM measurement errors on every turn, and averaging the results. Dispersion is simulated as a difference of two closed orbits, varying the RF frequency by a known amount in-between. All measurements include the effects of radiation damping and excitation.

For phase and coupling measurements, a macroparticle is resonantly excited using a simulated phase-locked tune tracker and allowed to equilibrate by tracking for several damping times (10^5 turns). After the particle trajectory has equilibrated, 40,960 turns of raw BPM button data are recorded at every BPM. The data is then processed with the same code used for processing CESR phase and coupling data, following Appendix C.

A comparison of lattice parameters derived from simulated measurements in an ideal lattice and those calculated directly by `Bmad` are summarized in Table 8.1 for each measurement type, and presumably represent a fundamental lower limit to the resolution of each measurement technique. Measurements for orbit, dispersion, and betatron phase have differing levels of agreement for horizontal and vertical, which can be attributed to the aspect ratio of the BPM geometry (seen in Fig. 4.1).

Measurement	RMS (Simulated - <code>Bmad</code>)	Units
Closed Orbit x, y	$20, < 1 \times 10^{-3}$	$[\mu\text{m}]$
$\eta_{x,y}$	$0.75, < 1 \times 10^{-6}$	$[\text{mm}]$
$\phi_{x,y}$	0.1, 0.05	$[\text{deg}]$
\bar{C}_{12}	4.3×10^{-4}	$[-]$

Table 8.1: RMS difference between simulated measurements and `Bmad`-calculated values, neglecting any BPM measurement errors.

8.1.3 BPM Errors

As was discussed in Chapter 6, BPM measurement errors can limit the quality of data used in optics corrections. It is therefore necessary to rigorously model BPM errors.

The two classes of BPM errors modeled in `ring_ma2` are BPM misalignments (offsets and tilts) and button-by-button effects (button gain, timing, and electronic noise). Each type of error will affect the measurement differently, and the order and application of errors must be modeled correctly. All simulated measurements presented include the effects of all listed BPM measurement errors.

BPM Misalignments: Offsets and Tilts

BPM alignment errors (offsets and tilts) are applied in the following way:

$$\begin{pmatrix} x \\ y \end{pmatrix}^m = R(\theta) \begin{pmatrix} x^{lab} - \delta x \\ y^{lab} - \delta y \end{pmatrix} \quad (8.1)$$

where $(x, y)^m$ are the coordinates with BPM misalignments applied, $R(\theta)$ is the rotation matrix for angle θ , and $\delta x, \delta y$ are the horizontal and vertical offset between the BPM and nearest quadrupole.

Button Effects: Gain, Timing, and Reproducibility

Timing errors, gain variations, and turn-by-turn resolution affect individual button signals. Modeling their effects requires an accurate method for converting from (x, y) coordinates to button signals $b_{1,2,3,4}$, applying errors, and converting back to (x, y) coordinates.

All button-by-button errors of these classes are handled through use of a nonlinear interpolation grid which converts (x, y) coordinates to button signals. Button-by-button errors are applied to the individual channels, and the final “measured” (x, y) coordinates are determined by the best fit to the set of new button signals using the same interpolation grid [33]. The nonlinear map used in these studies is for a BPM with a “CESR geometry” (see Figure 4.1).

The only geometric distortion which must be accounted for on a button-by-button basis is a relative horizontal shearing of the top and bottom BPM button

blocks. In this case, the upper two buttons will move in one direction, and the lower two buttons will move in the other direction. A common shift of the blocks in the same direction will change the electronic centering of the BPM, and therefore will be accounted for when calibrating the BPM-to-quadrupole centering (Sec. 6.3).

Including effects from button-to-button gain errors, timing errors, and measurement reproducibility, the four observed button signals b_i at each BPM are:

$$b_i^{meas} = g_i t_i b_i^m + \delta b_i^{noise} \quad (8.2)$$

In Equation 8.2 b_i^m is defined to be the button signal determined through the interpolation grid for the coordinates $(x, y)^m$ from Equation 8.1. g_i is the gain error on button i , and t_i is an effective gain error for button i arising from the timing error:

$$t_i = 1 + \frac{a_0}{a_2 - \frac{a_1^2}{4a_0}} (\delta t[s])^2 \quad (8.3)$$

where the constants $a_{0,1,2}$ are empirically determined, and a_0 is negative. This method of modeling the timing error also allows the BPM model to account for synchrotron motion by modulating the timings on all four buttons on a turn-by-turn basis.

BPM position measurement reproducibility is dominated by electronic noise arising from the digitization and amplification of an analog signal on each of the four controllers, and is modeled in Equation 8.2 as an additive error δb_i^{noise} on

each of the four button signals. The amplitude of the button-by-button reproducibility is set by determining the change in a single button signal consistent with changing the observed orbit by the desired (x, y) resolution (for example $10\mu\text{m}$).

8.2 Simulation Results for CsrTA

Misalignments and BPM errors used for simulations are summarized in Appendix E, Tables E.1, E.2, and E.3, and are either from directly-measured values or inferred from machine measurements.

The emittance correction procedure used in the simulation is identical to that used on the actual machine, outlined in Section 7.2. Results from `ring_ma2` are shown in Figure 8.1, and summarized in Table 8.2. The dashed black lines in Fig. 8.1 indicate the measured values from CESR presented in Tables 7.1 and 7.3.

Measurement	Initial	Iter 1	Iter 2	Iter 3	Units
ϕ	7.7	1.6	0.1	0.1	[deg]
η_y^{meas}	42.6	18.7	18.7	15.4	[mm]
η_y^{Bmad}	40.1	13.9	12.2	5.0	[mm]
\bar{C}_{12}	6.3	3.2	0.34	0.24	$[\times 10^{-2}]$
ϵ_y	255.8	33.0	27.5	4.1	[pm]

Table 8.2: 95% confidence level (CL) correction levels after each correction iteration. All values except η_y^{Bmad} include observational effects from BPM measurement errors. Details of the correction iterations are discussed in Section 7.2.

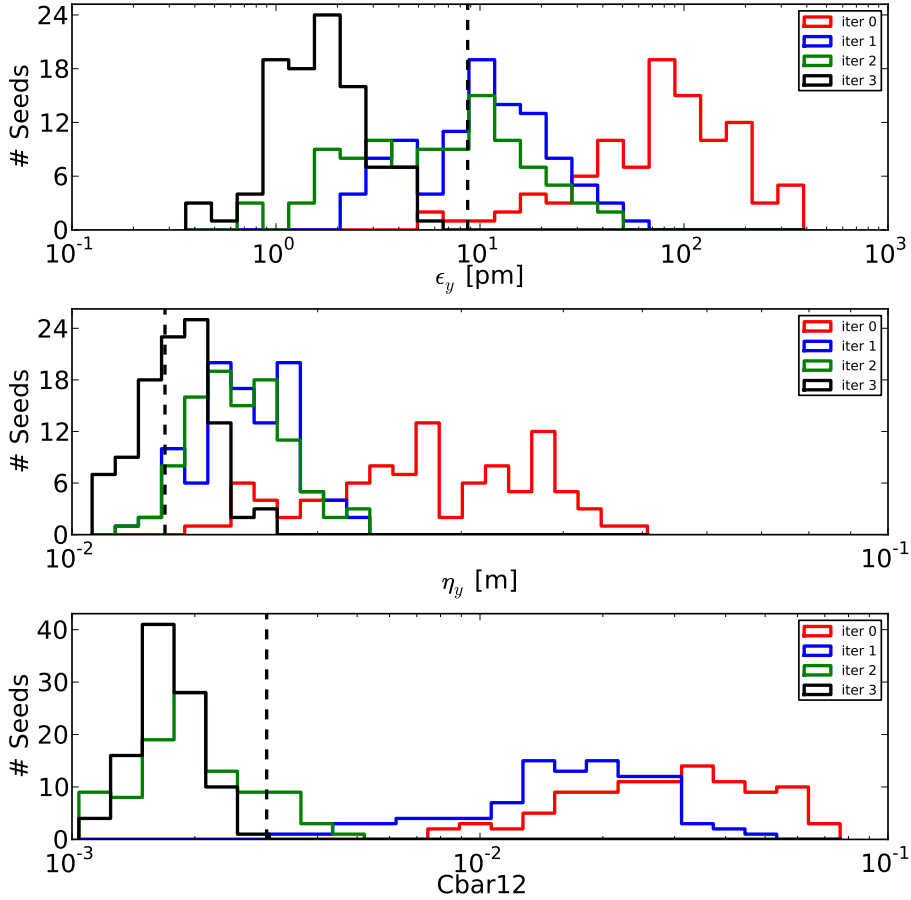


Figure 8.1: Results from `ring_ma2`, using misalignments and BPM measurement errors stated in Table E.1, plotted before correction (red), and after first, second, and third stage of emittance correction (blue, green, and black, respectively). Note that the horizontal axis is on a logarithmic scale. Dispersion and coupling are “observed” values, and include BPM measurement errors. Details of the correction iterations are discussed in Section 7.2. The dashed black lines indicate measured values in CESR.

8.3 Discussion of Simulation Results

Dispersion

When including the effects of BPM measurement errors the RMS vertical dispersion in the simulation agrees with what is measured in the machine. However,

the actual (rather than measured) RMS vertical dispersion in the simulation is much less. This implies that the measurement is dominated by BPM measurement errors, namely BPM tilt calibrations. Interestingly, although the actual dispersion is below the resolution of the dispersion measurement, the actual dispersion decreases after each step of the correction process. This suggests that by correcting the sources of vertical dispersion (vertical orbit and coupling) rather than the dispersion itself, most of the vertical dispersion present in the machine is eliminated.

Coupling

The average coupling in simulations after correction is roughly half of that measured in CESR. The lowest coupling measured in CESR is around $\bar{C}_{12} \approx 0.002$, barely within the distribution from the simulation.

Emittance

The 95%CL vertical emittance from `ring_ma2` is 4.1 pm, compared to the measured vertical emittance of $8.7 (+2.9/-3.4)^{sys} (\pm 0.2)^{stat}$ pm at 2.085 GeV. It is clear that there are sources of emittance dilution which are not accounted for in the `ring_ma2` model.

CHAPTER 9

DIAGNOSIS OF EMITTANCE DILUTION

The measured vertical dispersion in Table 7.3 and the minimum \bar{C}_{12} measured at CesrTA (0.002) are within the distributions from the simulation. This implies the errors applied to the model accurately reflect the optics in the accelerator. However, the simulations also indicate a vertical emittance significantly smaller than we measure, with 95% of seeds achieving $\epsilon_y < 4.1$ pm compared to a measured $\epsilon_y = 8.7$ pm. This suggests that the emittance is not limited by anything modeled in the `ring_ma2` simulations, including magnet misalignment, field errors, multipoles, and correction method.

Likely candidates for the remaining emittance dilution are time-dependent sources, which cannot be included easily in the `ring_ma2` simulations. Such sources include magnet power supply stability, line voltage stability, and interactions of the storage ring's stored beam with the pulsed synchrotron and transfer line magnets. These may contribute to the vertical emittance as discussed in Sec. 2.13.

9.1 Emittance Dilution from Feedback Modulators

Two bunch-by-bunch feedback systems are in use at CESR: a 14 ns system and a DIMTEL 4 ns system [5]. Both feedback systems are maintained in order to permit 4 ns bunch spacing for one species and 14 ns spacing for the other during dual-species CHESS operation. The outputs of the two feedback modulators are sent to a combiner, which is then sent to a common feedback amplifier which provides 55 dB of gain. This amplified signal is then sent to a stripline kicker in

the storage ring. Typical voltages are less than 5 V at the stripline kickers.

During the diagnosis of the residual vertical emittance, it was found that when the 14 ns feedback modulator gains are zeroed, the modulators continue to output a noise signal large enough to perturb the equilibrium emittance. This perturbation is seen as an increase in the vertical beam size and turn-by-turn spread in beam sizes from the xBSM, and an increase in beam centroid motion. The xBSM is a turn-by-turn device, therefore the beam centroid motion is not averaged into beam size during fitting, and the reduction in measured vertical emittance when disabling the feedback amplifiers cannot be attributed to a simple reduction in beam centroid motion. The feedback amplifiers were disabled for all low-emittance measurements reported in Table 7.3.

The turn-by-turn beam centroid motion before and after disabling the feedback amplifiers is shown in Fig. 9.1. Recalling that the circulation time in CESR is $2.56 \mu\text{s}$, it is clear that the overall beam motion is dominated by a substantial 60 Hz modulation, whose amplitude is unaffected by disabling the feedback amplifiers. However, a reduction in the intrinsic “width” of the 60 Hz modulation is seen. An FFT of the centroid motion data (Fig. 9.2) shows a significant reduction in the peaks at the vertical betatron tune (252 kHz) and its synchrotron sidebands (roughly $252 \text{ kHz} \pm 22 \text{ kHz}$).

A significant reduction in the turn-to-turn variation in beam size is also observed when disabling the feedback amplifiers (Fig. 9.3). There is a corresponding reduction in the vertical tune and sideband peaks in the FFT spectrum (Fig. 9.4), though the peak-to-floor amplitudes for the beam size FFT are smaller compared to those in the centroid motion FFT.

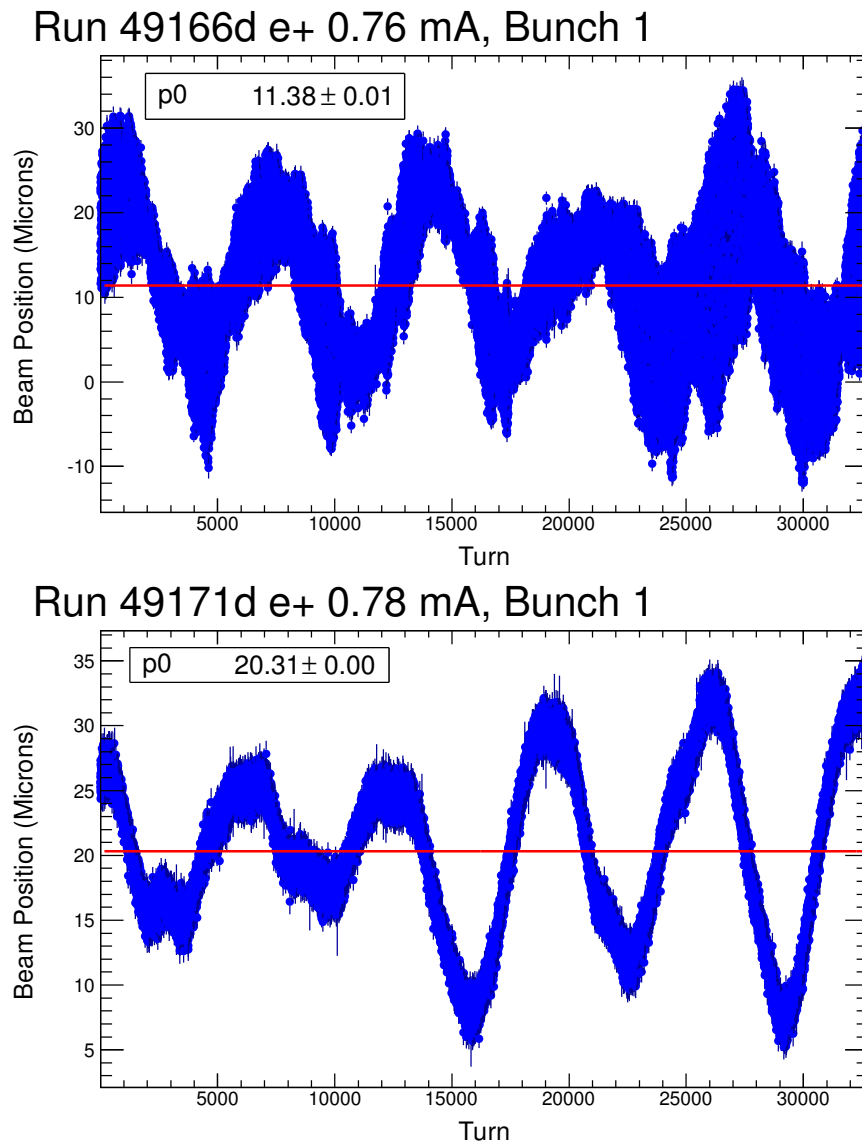
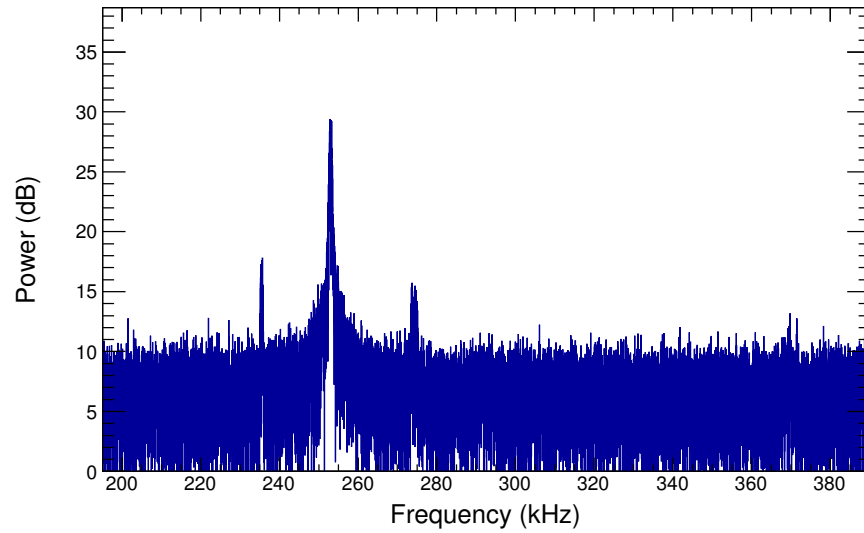


Figure 9.1: Turn-by-turn bunch centroid motion, before disabling transverse feedback amplifiers (top) and after (bottom).

Run 49166d e+ 0.76 mA, Bunch 1



Run 49171d e+ 0.78 mA, Bunch 1

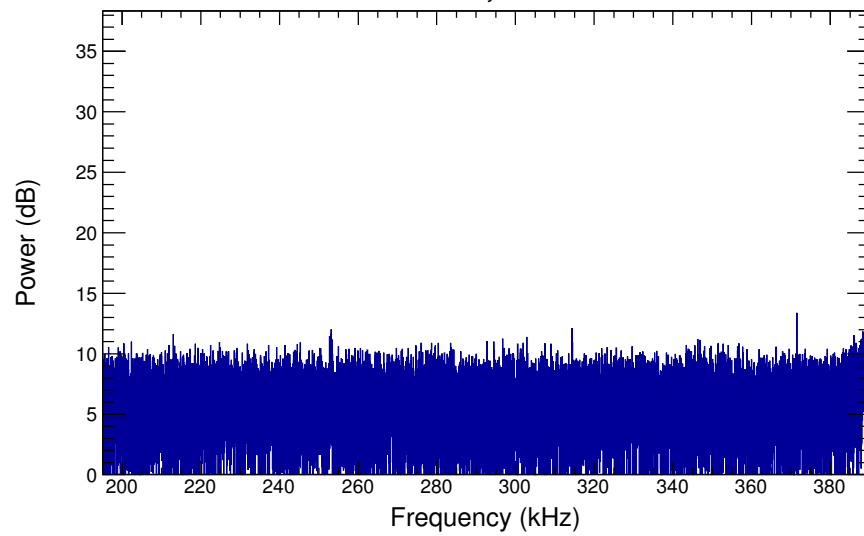
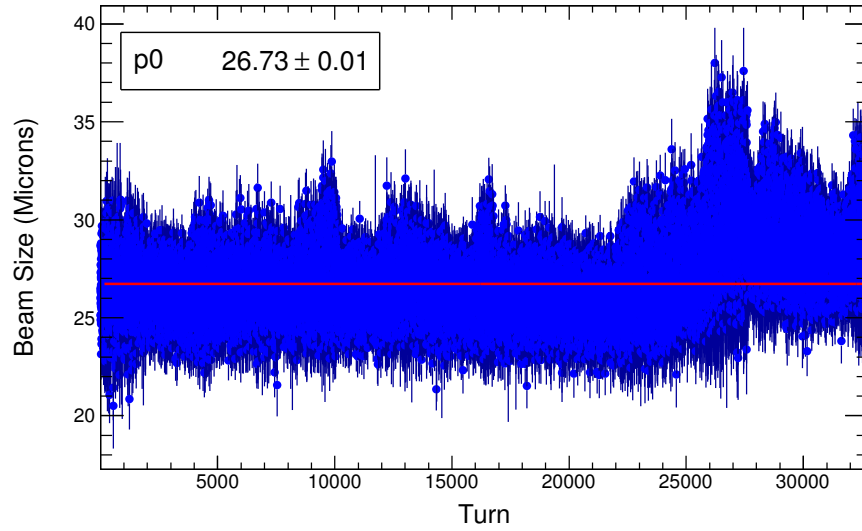


Figure 9.2: FFT of bunch centroid motion, before disabling transverse feedback amplifiers (top) and after (bottom). Circulation frequency is 390.1 kHz.

Run 49166d e+ 0.76 mA, Bunch 1



Run 49171d e+ 0.78 mA, Bunch 1

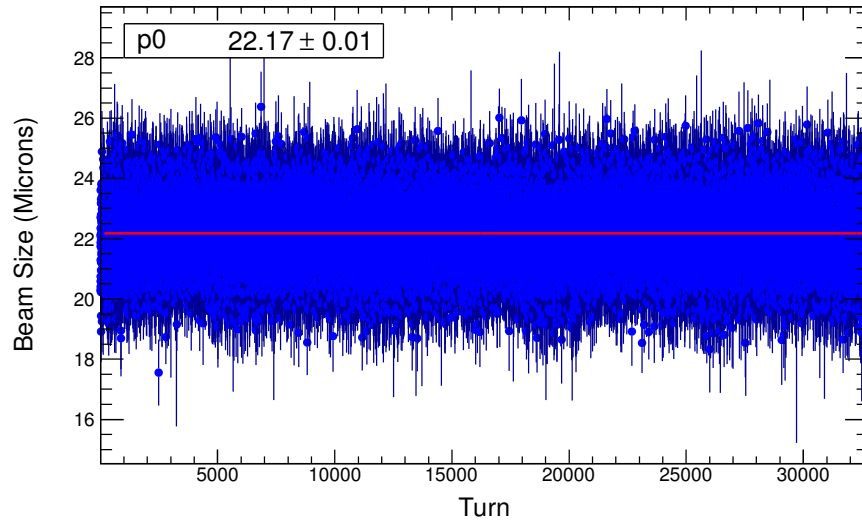
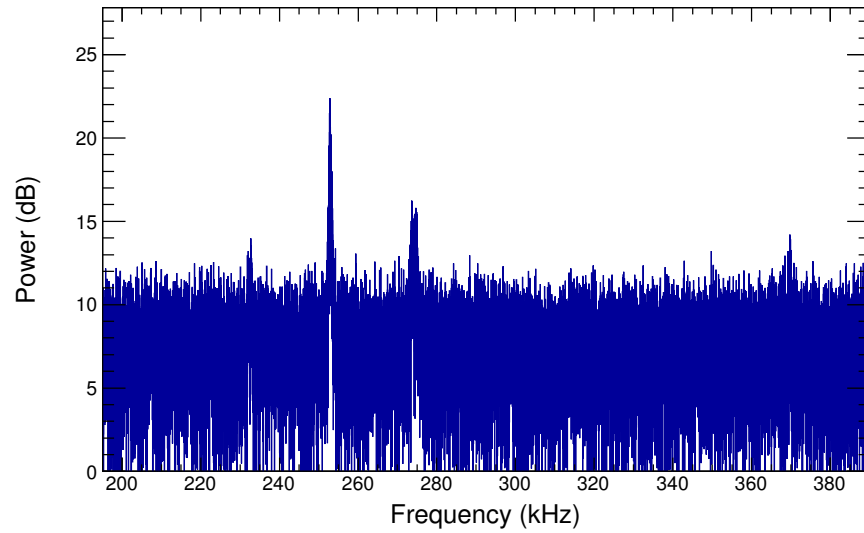


Figure 9.3: Turn-by-turn vertical beam size, before disabling transverse feed-back amplifiers (top) and after (bottom).

Run 49166d e+ 0.76 mA, Bunch 1



Run 49171d e+ 0.78 mA, Bunch 1

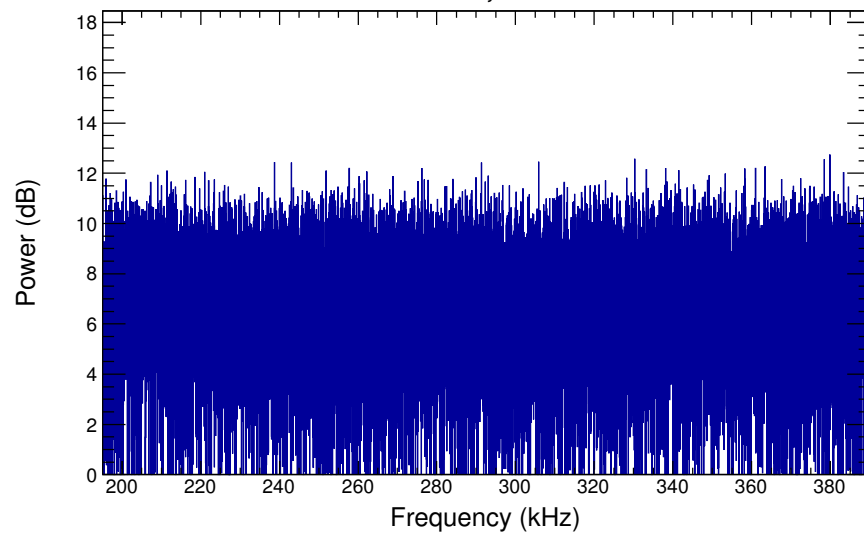


Figure 9.4: FFT of vertical beam size, before disabling transverse feedback amplifiers (top) and after (bottom). Circulation frequency is 390.1 kHz.

9.1.1 Estimate of Effect of Feedback Noise

The noise signal from the feedback modulator output has been measured in order to analytically compute its effect on the vertical emittance. An estimate of the contribution to emittance due to a time-varying kick was shown in Section 2.13 (Eqn. 2.95). Following Eqn. 2.94, this translates to an increase in the vertical emittance of:

$$\epsilon_{\theta} = \left(\frac{1}{2} \frac{T_0 E_0}{U_0 J_y} \right) \left(\frac{1}{2} f_0 \beta_0 \theta_{RMS}^2 \right) \quad (9.1)$$

$$= \frac{1}{4} \frac{E_0}{U_0 J_y} \beta_0 \theta_{RMS}^2 \quad (9.2)$$

where again θ_{RMS} is the RMS kick applied to the beam, on a turn-by-turn basis. This contribution to the vertical emittance adds linearly to the equilibrium emittance from radiation damping and quantum excitation. When attenuating the 14 ns feedback modulator input to the feedback amplifier, a reduction in vertical emittance is observed:

$$\sigma_y^0 = 25.2 \mu\text{m} \rightarrow \epsilon_y^0 = 15.1 \text{ pm} \quad (9.3)$$

$$\sigma_y^{atten} = 19.2 \mu\text{m} \rightarrow \epsilon_y^{atten} = 8.7 \text{ pm} \quad (9.4)$$

The contribution to the vertical emittance due to the 14 ns feedback modulator noise at zero-gain is therefore $\delta\epsilon_y = 6.4 \text{ pm}$.

The RMS voltage jitter from the modulator required to generate the observed change in emittance can be calculated using Eqn. 9.2. First, the kick θ_{RMS} which produces this level of emittance dilution is

$$\theta_{RMS} = \sqrt{4 \frac{U_0 J_y}{E_0 \beta_0} \delta\epsilon} \quad (9.5)$$

For $U_0 = 189$ keV/turn, $J_y = 1.001$, $E_0 = 2.085$ GeV, $\beta_0 = 26.8$ m, and $\delta\epsilon = 6.4$ pm, this yields $\theta_{RMS} = 9.3$ nrad.

The striplines are $L = 1$ m long, with a separation of $D = 10$ cm. The voltage can be determined by the beam rigidity (Eqn. 2.23):

$$E_0 [\text{GeV}] = 0.2998 B \rho [\text{T} \cdot \text{m}] \quad (9.6)$$

$$= 0.2998 \left(\frac{V/D}{c} \right) \left(\frac{L}{\theta_{RMS}} \right) \left[\frac{\text{V/m}}{\text{m/s}} \cdot \frac{\text{m}}{\text{rad}} \right] \quad (9.7)$$

$$V = \frac{E_0 c D \theta_{RMS}}{0.2998 L} \quad (9.8)$$

Using the provided values, the RMS voltage modulation at the plates is expected to be $V_{RMS} = 1.9$ V. This means the voltage jitter from the modulator output (prior to the 55 dB amplification) is expected to be:

$$V_{RMS} = 3.5 \text{ mV} \quad (9.9)$$

The measured voltage noise from the feedback modulator has a total peak-to-peak amplitude of ≈ 50 mV RMS. However, much of this is constant from shot to shot, which creates a static perturbation to the closed orbit. The modulation in the voltage from shot to shot is closer to 20 mV peak-to-peak, with a standard deviation of 2.3 mV, in reasonable agreement with the analytic estimate.

9.2 Remaining Sources of Beam Jitter

Other time-varying sources of emittance dilution may be responsible for the remaining discrepancy between the measured emittance and `ring_ma2` simulation results. From Fig. 9.1, it is clear that there are two components to the beam motion: a large-amplitude (roughly $40\ \mu\text{m}$ peak-to-peak) 60 Hz modulation varying over thousands of turns, and a small-amplitude (roughly $10\ \mu\text{m}$ peak-to-peak) fast modulation varying on a turn-by-turn basis.

By disabling the transverse feedback amplifiers the amplitude of fast modulation reduces in amplitude from around $12\ \mu\text{m}$ peak-to-peak to $6\ \mu\text{m}$, corresponding to a reduction in vertical emittance of $6.4\ \text{pm}$, or 40%. If real, the remaining fast modulation of $6\ \mu\text{m}$ will also contribute to emittance dilution. By extension of the feedback modulator study, eliminating this additional fast modulation may reduce the vertical emittance by a further $6\ \text{pm}$, bringing the measurements into agreement with the `ring_ma2` study.

The 60 Hz component is slow, on par with the damping time ($60\ \text{Hz} = 17\ \text{ms}$, compared to $\tau = 50\ \text{ms}$). Therefore, for Eqn. 9.2 to be applicable, one must consider the RMS variation in the kick on a turn-by-turn basis, rather than the full amplitude. To estimate the impact this modulation may have, the 60 Hz signal is assumed to have a single source, the feedback modulator. In this case, using the same derivation as before, the emittance dilution due to the turn-by-turn change in kick for the 60 Hz source would be $\delta\epsilon_y = 0.05\ \text{pm}$, which is insignificant compared to the roughly $5\ \text{pm}$ necessary to bring the measurements into agreement with the simulation.

The remaining sources of kicks inducing the fast modulation must be iden-

tified for this hypothesis to be tested. The diagnosis is complicated by the fact that there are no significant peaks in the FFTs of bunch centroid motion or vertical beam size which might correspond to the high-frequency centroid motion seen in the turn-by-turn plots. Two approaches to the analysis are taken: by considering the energy dependence of the vertical emittance, and by directly disabling non-critical time-varying components in the ring.

9.2.1 Energy Dependence

Contributions to the vertical emittance from quantum excitation, magnet misalignments and field errors, and from time-varying sources each scale differently with energy. By measuring the minimum vertical emittance achieved at multiple energies, some understanding of the relative contributions of these terms may be gained.

A detailed derivation of the energy dependence is presented in Appendix F. The emittance is modeled as having four components, summing linearly:

$$\epsilon_b(E_0) = C_{OA}\epsilon_b^{OA}(E_0) + C_{QE}\epsilon_b^{QE}(E_0) + C_{RF,\theta_s}\epsilon_b^{RF,\theta_s}(E_0) + C_{\theta_c}\epsilon_b^{\theta_c}(E_0) \quad (9.10)$$

where the four terms arise from the finite opening angle of the radiation fan, quantum excitation for radiation emission in dispersive regions, RF jitter and time-varying dipole kicks whose amplitudes scale inversely with energy (combined into the same term as they have the same energy dependence), and time-varying dipole kicks whose amplitudes do not scale with energy.

Note that while the convention here refers to whether the dipole kicks themselves scale with energy, in reality these kicks would arise from places such as the current stability in magnet power supplies. Therefore, a time-varying dipole kick which does not scale with energy would arise from a magnet power supply whose amplitude of current jitter does scale with energy.

The constants C_i denote the relative strength of the contributions, and are constrained to be positive. The terms ϵ_b^i are normalized such that $\epsilon_b^i(2.085 \text{ GeV}) = 1$ and the constants C_i directly reflect the emittance contribution of each term in picometers. Additionally, $C_{OA}\epsilon_b^{OA}$ has been shown to contribute minimally to the emittance (0.22 pm at 2.085 GeV), and scales minimally with energy (down to 0.18 pm at 2.553 GeV). This term is therefore fixed at 0.2 pm for these studies, to reduce the number of free parameters.

The vertical emittance was measured after corrections at 2.305 GeV and 2.553 GeV, in addition to the nominal 2.085 GeV. For all three energies the optics are constrained such that the differences are minimal, aside from B_{max} in the damping wigglers remaining constant at 1.9 T. Using measurements from Table 7.3, the constants C_i are determined by fitting the data for four scenarios:

1. Assume no contributions from RF jitter or time-varying dipole kicks, therefore $C_{RF,\theta_s} = C_{\theta_c} = 0$.
2. Assume no contributions from RF jitter or time-varying dipole kicks which scale inversely with energy, therefore $C_{RF,\theta_s} = 0$.
3. Assume no contributions from time-varying dipole kicks which do not scale with energy, therefore $C_{\theta_c} = 0$.
4. Make no assumptions about the contributions from time-varying sources,

and allow both C_{RF,θ_s} and C_{θ_c} to vary.

The resulting curves for emittance as a function of energy are shown in Fig. 9.5. The constants C_i for each scenario are summarized in Table 9.1.

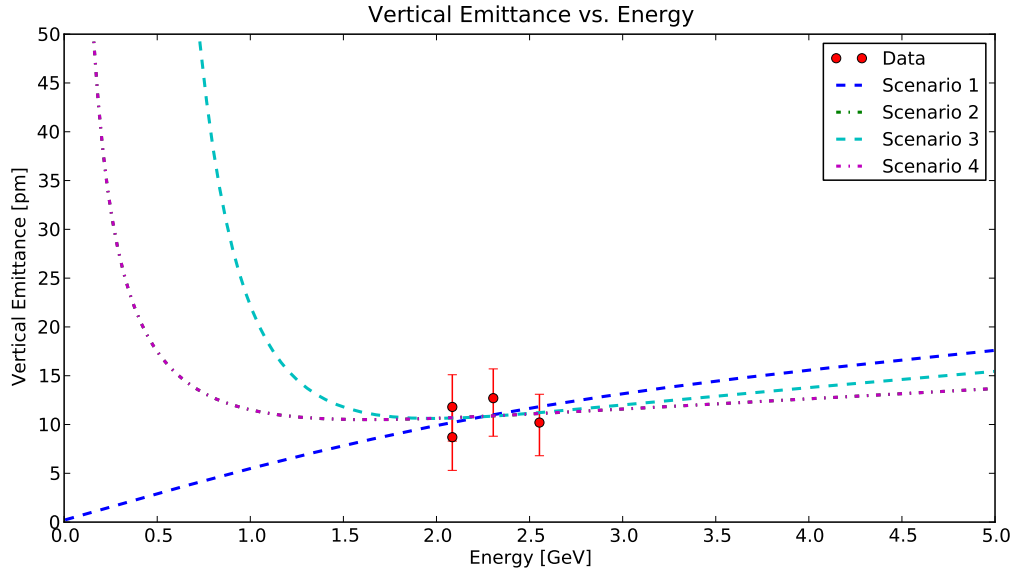


Figure 9.5: Vertical emittance for a single bunch of positrons, as a function of energy. Measurements are shown in red, and were taken in December 2012 (2.085 GeV, 2.305 GeV) and April 2013 (2.085 GeV, 2.553 GeV). Four functional fits to the data are shown (blue, green, cyan, magenta), using the form of Eqn. 9.10. Note that curves 2 and 4 overlap nearly identically. Plotted error bars are systematic only, and indicate that all measurements would move in the same direction; statistical error bars are smaller than the data points.

Scenario	C_{OA}	C_{QE}	C_{RF,θ_s}	C_{θ_c}
1	0.2	10.016	0	0
2	0.2	7.29404	0	3.2021
3	0.2	8.73394	1.71788	0
4	0.2	7.29406	3.29793×10^{-5}	3.2025

Table 9.1: Constants C_i for the three models of the energy dependence of the vertical emittance. Note that the functions are normalized such that the energy-dependent terms are unity at $E_0 = 2.085$ GeV, and the constants C_i may be read as the contribution to the vertical emittance from that term at 2.085 GeV.

It does not appear to be possible to distinguish between the four functions

over the energy reach of CESR. Below 1.5 GeV the curves begin to diverge, however CESR has not been run below 1.5 GeV, and it is doubtful that the xBSM would have sufficient flux at such low energy.

Yet it is still possible to glean some information from this plot. It is unlikely that no time-varying sources of emittance dilution exist in CESR, therefore Scenario 1 is unrealistic. Similarly, it is unlikely that the magnet power supplies are infinitely stable, therefore Scenario 3 is also eliminated. The curves for Scenarios 2 and 4 nearly identically overlap. That is, even when the fitter is allowed to vary the contributions from the RF and dipole kicks which do not scale with energy, it does not improve the quality of fit. This suggests that RF voltage jitter (and time-varying dipole kicks which scale inversely with energy) are not responsible for the emittance dilution. Scenario 2 is therefore the most likely model, in which case around 3.2 pm of the vertical emittance at 2.085 GeV may be due to time-varying dipole kicks which do not scale with energy.

Despite this possibility, it is still an insufficient contribution to the vertical emittance to bring the measurements into agreement with the simulation.

9.2.2 Eliminating Time-Varying Elements

Turn-by-turn beam size and centroid motion were recorded while systematically disabling various non-essential components in the storage ring. The tests are summarized in Table 9.2 (on p. 117). It should be noted that the studies summarized in this section were taken while the W2 RF cavity was disabled to prevent beam loss from the cavity tripping, therefore only three RF cavities were used (one in the West, and two in the East). Nominal total RF voltage was

4.8 MV.

For the majority of tests there is little or no effect on the emittance. A small reduction in beam size was observed when reducing the total RF voltage from 4.8 MV to 1.7 MV. A further reduction is seen when the W1 RF cavity is powered down and detuned, such that only the two East RF cavities are running; the emittance increased slightly when running only on the W1 RF cavity. This indicates that the RF system is contributing to the vertical emittance, although the extent or mechanism is not known. The East and West RF cavity pairs run on separate power supplies. One possibility is that the West RF power supply is less stable than the East, thereby introducing vertical emittance through modulation of the RF voltage as discussed in Sec. 2.13.2. Alternatively, by running a single cavity at a higher voltage, the level of voltage jitter is increased, possibly increasing the contribution to the emittance. Yet another possibility is that the input couplers to the RF cavities are applying a small transverse kick to the beam on a turn-by-turn basis.

In all tests, turn-by-turn beam size and centroid motion were also analyzed. The amplitude of the fast modulation seen in Fig. 9.1 does not decrease below the $6\ \mu\text{m}$ peak-to-peak amplitude seen when disabling the feedback amplifiers.

14 ns Feedback Modulators	Transverse Feedback Amps	Horiz. Sep. HV	Synch AC	Total RF Voltage	East RF	West RF	ϵ_y [pm]
On	On	On	On	4.8	On	On	17.0
Attenuated	On	On	On	4.8	On	On	11.5
Attenuated	Off	On	On	4.8	On	On	11.5
Attenuated	Off	Off	On	4.8	On	On	11.5
Attenuated	Off	Off	Off	4.8	On	On	11.5
Attenuated	Off	Off	Off	1.7	On	On	11.2
Attenuated	Off	Off	Off	1.7	Off	On	12.5
Attenuated	Off	Off	Off	1.7	On	Off	10.8

Table 9.2: Summary of beam stability tests at CestrA. The measurements were conducted in April 2013, for a single bunch of positrons at 0.7-0.85 mA.

9.3 Other Candidates for Residual Emittance Dilution

It is clear that none of the sources of emittance dilution addressed thus far are easily identified as the reason for the discrepancy between the `ring_ma2` simulations and the measured emittance.

It is highly unlikely that the vertical emittance in CESR is in fact in agreement with the `ring_ma2` studies, and that the discrepancy between measurement and simulation arises from observational errors in the beam size measurement. By Eqn. 4.1, assuming no vertical dispersion, $\epsilon_y = 4.1$ pm corresponds to $\sigma_y = 12.8$ μm , nearly 50% smaller than the measured beam size from the xBSM at 2.085 GeV. This is well outside the uncertainty of the xBSM measurements, as shown in Sec. 7.4.

There are four remaining possibilities for the discrepancy. First, there may be sources of emittance dilution which should be accounted for in the simulations, but have not been included. Second, the simulations may accurately reflect the contributions of static sources of emittance dilution, and there are non-static sources in the storage ring which have not been identified. The third possibility is that beam-gas scattering is contributing to an increase in the core emittance. Finally, collective effects may be diluting the emittance at very low beam current.

9.3.1 Errors Omitted from `ring_ma2`

No known optics errors with known amplitudes have been omitted from the `ring_ma2` model.

Static errors which are known or assumed to exist, but have not been investigated, are: RF cavity offset, tilt, and pitch; multipole fields in dipoles and quadrupoles; and internal manufacturing tolerances on dipoles and quadrupoles. These errors are assumed not to contribute significantly to the emittance dilution.

Additionally, there are known correlations between some magnet errors. For example, sextupoles share their mountings with quadrupoles, therefore the misalignments will be correlated. This correlation is not presently an option in the simulation, and should be included for completeness. Additionally, there are known large-scale correlations between horizontal positions of quadrupoles. Although the overall amplitude of the horizontal offsets may be as high as a few millimeters, the deviation from one quadrupole to the next has an RMS of more around $350 \mu\text{m}$. Simulations have suggested that this large-scale structure does not contribute to emittance dilution.

All static BPM measurement errors have been accounted for. However, it is possible that time-varying BPM measurement errors may exist. For example, random BPM processor failures where a single button may occasionally not report a value on a given turn, or button gains which fluctuate over the course of a measurement. These effects will need to be characterized in the machine in order to determine whether they need to be included in the model.

9.3.2 Sources in CESR

The remaining sources which may be contributing to the observed emittance discrepancy are time-varying errors. Time-varying sources been investigated

in substantial detail in Sec. 9.2.2, however not all potential sources have been examined. It is either not straightforward or not possible to test the remaining time-varying elements in CESR.

Candidates in this category include: the RF system, either through power supply stability, beam loading, or kicks from the couplers; vacuum pumps; and the magnet power supply “choppers,” which pulse current through the magnet coils at around 17 kHz.

9.3.3 Residual Gas Scattering

Infrequent, large-angle scattering between particles within the bunch and residual gas molecules will increase the scattered particle’s betatron amplitude and thus introduce non-Gaussian tails in the beam profile [50]. These tails typically start around $5-8\sigma$ of the beam distribution, where the density is $10^{-4}-10^{-8}$ of the core density.

Under normal measurement conditions the xBSM measures at most a few tens of photons/pixel/bunch in the core of the image, therefore the non-Gaussian beam tails will not produce enough light to be visible in the turn-by-turn vertical beam size measurements. This would result in a slight underestimation of the beam emittance derived from from xBSM imaging, implying the discrepancy between measured and simulated vertical emittances is slightly larger than previously thought. However, this effect is minimal as the particle density is extremely small in the tails.

Residual gas scattering will increase linearly with current, as gas particles

are released when synchrotron radiation strikes the vacuum chamber, and synchrotron radiation increases linearly with current in the machine. Scattering events will therefore also increase with current, and contributions to the vertical emittance will increase. Measurements of the emittance as a function of current (Fig. 9.6) do not demonstrate any significant increase with current, again indicating the contribution to the emittance from residual gas scattering is small.

9.3.4 Collective Effects

The CesrTA emittance target of 10 pm is for a “zero-current” beam; that is, neglecting any collective effects. It is possible, though again unlikely, that the emittance at 0.8mA/bunch (1.3×10^{10} /bunch) is already diluted to do collective effects. The four collective effects considered here are electron cloud, fast-ion instability, and intra-beam scattering.

In order for electron cloud to affect the emittance, typically a train of 30 positron bunches with 0.5 mA/bunch or more is necessary, and the emittance blow-up takes place much later than the first bunch, around bunch 10-15 [51]. The beam requirements are similar for fast-ion instability, which only significantly affects electron bunches. It is therefore unlikely that electron cloud or fast-ion instability are causing emittance dilution in a single bunch of 0.8 mA.

The mechanism through which intra-beam scattering (IBS) increases vertical emittance depends on transverse-to-longitudinal scattering in regions with dispersion or transverse-to-transverse scattering in regions with coupling, such that the vertical-mode action of the particle changes. Vertical dispersion and coupling are measured to be globally well-corrected, and are well below levels

required for IBS to contribute to vertical emittance dilution. Extensive measurements and simulations on IBS at CesrTA [27,52] also indicate that the vertical emittance is largely insensitive to IBS effects at currents $I < 1$ mA/bunch, where the measurements reported here were taken.

By recording beam size measurements at very low current, it may be possible to determine whether collective effects are contributing to the emittance at the nominal 0.8 mA/bunch used during measurements. However, at such low current, photon statistics become questionable and the turn-by-turn fitting procedure which is normally used is no longer sufficient. Instead, the turn-by-turn images must be averaged first in order to improve signal-to-noise, then fit as a single image. This has the drawback of incorporating a small amount of turn-by-turn beam motion, however this can be accounted for in post-processing.

Figure 9.6 shows the emittance calculated from a series of vertical beam size measurements from the xBSM, taken sequentially as the current was decreased from 1.1 mA to around 0.05 mA, and processed as described above.

It is unclear whether the behavior at very low current (below 0.1 mA) is due to insufficient photon statistics for the xBSM analysis, or whether it is due to actual beam physics. As such, it is not possible to rule out some form of collective effect with a very low-current threshold; however, no known collective effect would display this behavior as a function of bunch current, and the effect would have the unusual characteristic of saturating at very low bunch current (below $1 \text{ mA} = 1.6 \times 10^{10}$ /bunch).

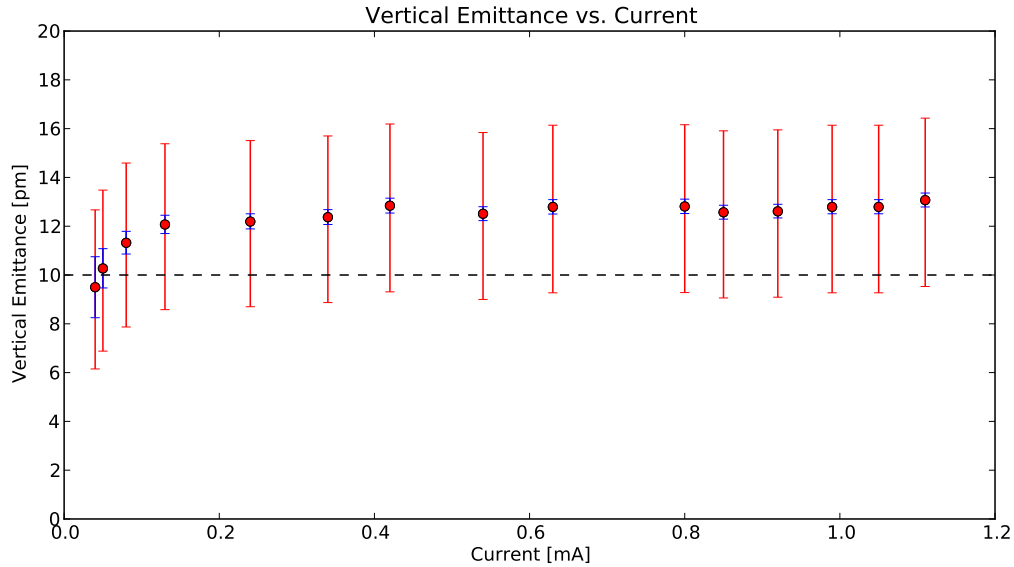


Figure 9.6: Vertical emittance for a single bunch of positrons as a function of bunch current, from April 2013 CEsrTA machine studies. Plotted error bars are systematic (red) and statistical (blue). The dashed horizontal line indicates the 10 pm zero-current vertical emittance target for CEsrTA.

9.4 Toward the Quantum Limit

It is evident that there are still sources of emittance dilution which have not been identified. If these sources can be eliminated, the vertical emittance will be in agreement with `ring_ma2` simulations. In this scenario, it is conceivable to push the 95%CL vertical emittance toward the ILC damping ring vertical emittance of 2 pm, and ultimately to the quantum limit ($\epsilon_y \approx 0.2$ pm).

The most significant contributions to emittance dilution in `ring_ma2` are the first to be examined, in the interest of achieving the largest reduction in vertical emittance with the least amount of effort in survey and alignment or BPM characterization. A summary of `ring_ma2` tests focusing on these contributions to the vertical emittance is presented in Table 9.3. For all tests, any parameters not mentioned are identical to those in the nominal CEsrTA simulations (see Tables

E.1, E.2, E.3).

By only decreasing the BPM tilt error from 12 mrad to 5 mrad, the vertical emittance due to optics errors is brought below the ILC damping rings emittance budget of 2 pm for 95% of the randomly-misaligned lattices. However, further reductions in other parameters do not further improve the vertical emittance. It appears BPM errors continue to limit the vertical emittance. Tests where each class of BPM error is systematically decreased by an order of magnitude are summarized in Table 9.4.

BPM Tilt [mrad]	Quad y Offset [μm]	BPM-to-Quad Offset [μm]	Quad Tilt [μrad]	Dipole Roll [μrad]	Wiggler Roll [μrad]	Mean ϵ_y [pm]	95%CL ϵ_y [pm]
12	107.8	170	148	144	250	1.86	4.15
10	107.8	170	148	144	250	1.41	2.94
5	107.8	170	148	144	250	0.96	1.85
2	107.8	170	148	144	250	0.76	1.33
5	25	170	148	144	250	1.46	2.74
5	25	25	148	144	250	1.27	2.55
5	25	25	25	144	250	1.14	2.12
5	25	25	25	25	250	1.28	2.33
5	25	25	25	25	25	1.27	2.14

Table 9.3: Summary of `ring_ma2` tests reducing the most significant contributions to the vertical emittance. The first row summarizes the results from the nominal simulation (Tab. 8.2). Unless stated in this table, all other errors in Sec. E.1 are included at the nominal amplitudes.

Reproducibility [μm]	Tilt [μrad]	Offset [μm]	Gain [%]	Timing [ps]	Shear [μm]	Mean ϵ_y [μm]	95%CL ϵ_y [μm]
10	12	170	0.5	10	100	1.86	4.15
1	12	170	0.5	10	100	1.86	3.68
10	1.2	170	0.5	10	100	0.85	1.70
10	12	17	0.5	10	100	1.69	3.07
10	12	170	0.05	10	100	1.50	2.89
10	12	170	0.5	1	100	1.86	3.21
10	12	170	0.5	10	10	1.97	3.86
5	6	85	0.25	5	50	0.78	1.22
1	1.2	17	0.05	1	10	0.51	0.86
0	0	0	0	0	0	0.50	0.92

Table 9.4: Summary of `ring_ma2` tests systematically reducing all BPM errors. The first row is for the nominal scenario, with measurement errors corresponding to measurements and estimates of actual machine conditions. All other errors are identical to those listed in Sec. E.1.1.

Although a few BPM errors contribute significantly to the emittance correction process, no single measurement error is preventing the correction of the vertical emittance to under 1 pm. It is only when all BPM measurement errors are decreased by a factor of 10 that the 95%CL for the contribution of the static optics to the vertical emittance is brought below the 1 pm level.

A more global reduction in magnet errors is required in order to approach the quantum limit. Table 9.5 summarizes the effects of reducing all misalignments and errors by a common factor. BPM measurement errors are included in the reduction, however multipoles are not, as multipoles are most commonly due to manufacturing tolerances and it is unreasonable in the context of this study to consider disassembling or replacing large numbers of magnets.

Reduction Factor	Mean ϵ_y [pm]	95%CL ϵ_y [pm]
Ideal Lattice	0.22	0.22
1x (Nominal)	1.86	4.15
2x	0.64	0.96
4x	0.33	0.47
10x	0.24	0.26

Table 9.5: Summary of `ring_ma2` tests reducing all misalignments and errors by a common factor. BPM errors are affected by the reduction factor, however multipoles are excluded from the multiplier on the basis of being a manufacturing tolerance in magnets which are already built.

By decreasing all misalignments and errors by a factor of 4, nearly 95% of the seeds achieve a vertical emittance within a factor of two of the quantum limit. Further improvements could hypothetically be made, and by decreasing all errors by a factor of 10 from their present values, all seeds achieve a corrected vertical emittance within a fraction of the quantum limit.

9.5 Conclusions

The vertical emittance in CEsrTA is clearly dominated by sources which have not yet been positively identified. Further work is necessary in order to diagnose the source (or sources) of emittance dilution.

The discrepancy between measured vertical emittance and `ring_ma2` simulations does not appear to be due to magnet misalignment or field errors, multipoles, manufacturing tolerances, xBSM beamline or detector systematics, or any easily-tested time-varying components in the storage ring.

The energy dependence of the minimum-achieved emittance (Fig. 9.5) implies roughly 1/3 of the residual vertical emittance may be due to time-varying sources. Possible candidates include: the RF system, including misalignments, higher-order modes, beam loading, and input coupler effects; and time-varying sources which are not easily tested, such as magnet power supply choppers, and the stability of the master oscillator. From the potential current-dependence of the emittance (Fig. 9.6), collective effects with a very low-current threshold may also be contributing.

Improving BPM detector tilt calibrations from 12 mrad RMS to 5 mrad RMS, the vertical emittance could potentially be decreased by more than 2 pm. If all BPM calibrations are improved by a factor of 2, the reduction in vertical emittance would be nearly 3 pm. Further decrease in the vertical emittance would require a global magnet realignment effort. Improving all magnet alignments by a factor of 4, the contributions from the static optics to the vertical emittance are nearly eliminated.

CHAPTER 10

ILC DAMPING RINGS

In Chapter 7, an optics correction method was demonstrated at CEsrTA which scales well to large rings. This optics correction method was then simulated in Chapter 8. Agreement between the measured and simulated optics functions was demonstrated, indicating that the model is accurate. It is then possible to extrapolate the characterization method to a storage ring which is not yet built. In particular, the optics correction procedure at CEsrTA was developed specifically for the International Linear Collider damping rings [1], and it is of interest to determine how the ILC damping rings will react to such a correction.

10.1 ILC - Overview

The proposed beam energy of the ILC is up to 250 GeV/beam (500 GeV center-of-mass). This is sufficiently high-energy to make a small-footprint circular collider impractical. The largest storage ring electron/positron collider to-date was the Large Electron/Positron Collider (LEP) at CERN, operating at roughly 100 GeV/beam with a circumference of 26.6 km [53]. Following Eqn. 2.64, the energy loss due to synchrotron radiation at LEP was around 2% on every turn, large enough to be problematic.

If LEP had operated at the proposed ILC energy (250 GeV), the losses due to synchrotron radiation would have been $> 30\%$ of the total beam energy on every turn. This would require an impractical number of RF cavities, reducing room required for other components. Conversely, if the ILC were built as a

circular accelerator, and the energy loss to synchrotron radiation were limited to be the same as LEP (2%), the storage ring would need to be 415 km in circumference, which is prohibitively large. However, power loss to synchrotron radiation is only a problem in circular accelerators; in a linear accelerator, the transverse deflection is minimal, therefore I_2 is small, and U_0 is small. Therefore, the proposed design is a pair of linear accelerators (linacs), each roughly 15 km long.

The International Linear Collider (ILC) design utilizes damping rings to cool beams delivered by the electron and positron sources before transferring to the main linacs. Three of the primary requirements of the baseline damping rings are: 1) they must accept an injected bunch from the positron source, with normalized phase-space amplitude 0.07 m-rad and $\delta_E/E = 0.75\%$; 2) the beams must be cooled to an equilibrium zero-current geometric vertical emittance ≤ 2 pm; and 3) the damping time must be short enough to provide fully damped bunch trains at a repetition rate of 5Hz.

10.2 DTC04 Lattice

The ILC damping ring design characterized is the DTC04 lattice developed by D. Rubin *et al.* [54]. The lattice is a 3.2km racetrack design with a modified TME-type arc cell. The zero-dispersion straights are based on the work of Korostelev and Wolski [55]. A schematic of the ring is shown in Figure 10.1; optics functions are shown in Figure 10.2. Tables 10.1 and 10.2 summarize the lattice parameters and number of magnets of each type.

The arc cell layout is shown in Figure 10.3. Arc cells are comprised of one

Parameter	Value	Units
Circumference	3239	[m]
Energy	5.0	[GeV]
Train Repetition Rate	5	[Hz]
Bunch Population	2×10^{10}	[-]
Extracted $\epsilon_x^{geometric}$	0.6	[nm]
Extracted $\epsilon_y^{geometric}$	< 2	[pm]
Extracted Bunch Length	6	[mm]
Extracted σ_E/E	0.11	[%]
Damping Time	24	[ms]
Wiggler B^{max}	1.5	[T]

Table 10.1: Summary of the DTC04 lattice parameters.

Class	Count
Beam Position Monitor	511
Dipole	164
Horizontal Steering	150
Vertical Steering	150
Combined H+V Steering	263
Quadrupole	813
Skew Quadrupole	160
Sextupole	600
Damping Wigglers	54

Table 10.2: Summary of elements in the DTC04 lattice.

dipole, three quadrupoles, four sextupoles, one skew quadrupole, and two beam position monitors.

A fully-symplectic Lie map has been created for tracking through the damping wigglers [56–58], however this tracking method is time-consuming. When the full nonlinearities of the damping wigglers are known to not affect the resulting simulation, a simplified MAD-style “bend-drift-bend” wiggler model which preserves the radiation integrals can be used to reduce the time required for simulations.

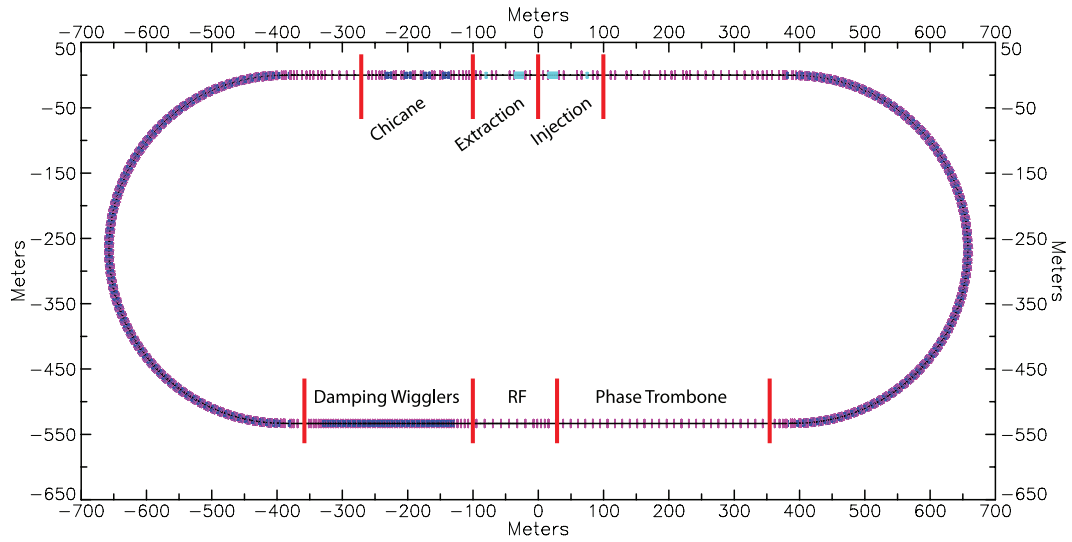


Figure 10.1: Layout of DTC04 lattice.

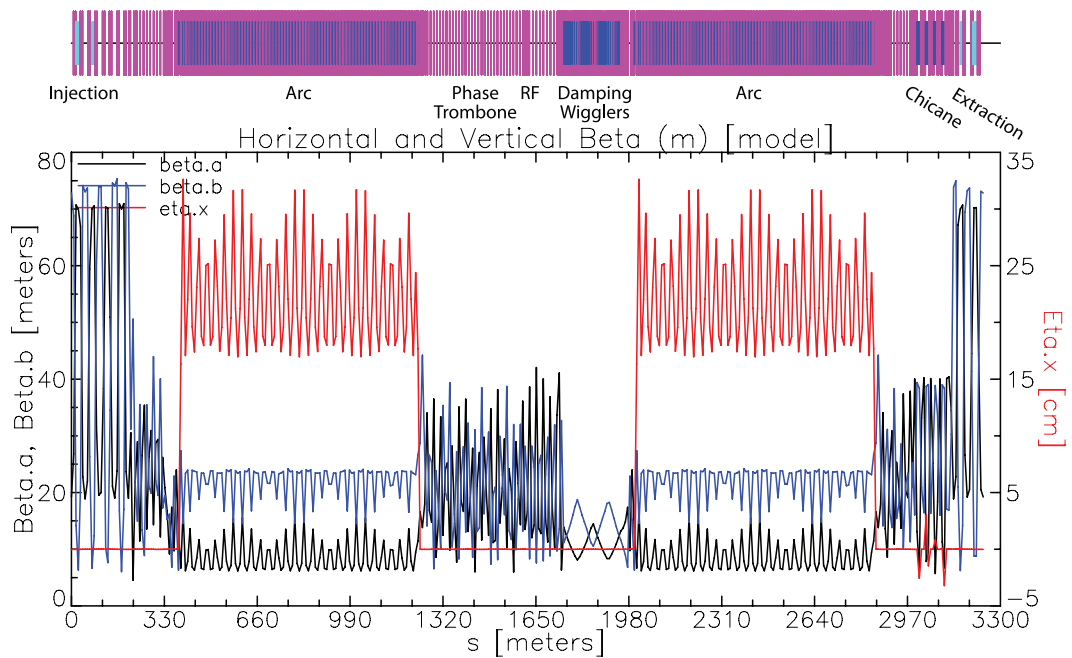


Figure 10.2: Horizontal and vertical beta functions and horizontal dispersion for the DTC04 lattice.

10.3 Characterization Method

The damping ring requirements must be met in a real machine that includes magnet misalignments, guide field multipoles (systematic and random), and

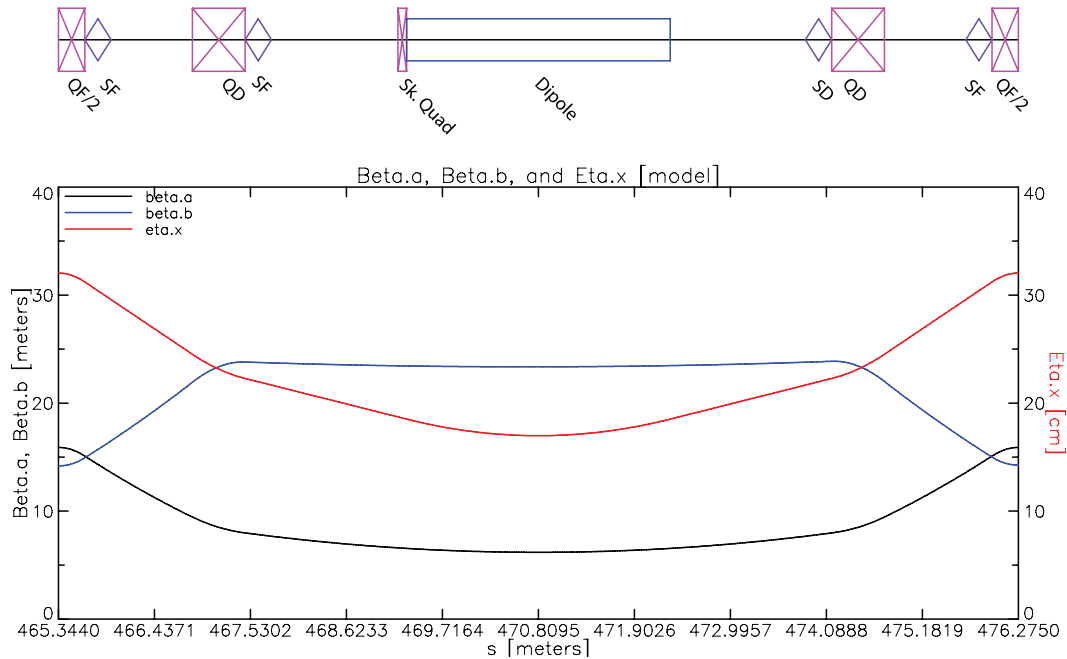


Figure 10.3: DTC04 arc cell.

beam position monitor (BPM) measurement errors. Emittance tuning will be essential to achieve the target zero-current emittance. Quadrupoles and corrector magnets will be independently powered, allowing for localized corrections through the use of beam-based measurements.

The lattice cannot be characterized with respect to the exact set of errors they will have, as the rings are not yet built. Alignment errors in the damping rings are assumed to be randomly distributed with amplitudes dictated by survey tolerances. The characterization is based on a statistical analysis of the likelihood that we will achieve the required parameters, by simulating a large number of lattices with random distributions of errors at the appropriate levels. A configuration is deemed acceptable if 95% of the randomly-misaligned and corrected lattices meet the required vertical emittance and dynamic aperture.

The characterization method is comprised of two tasks: generating a ran-

domly misaligned lattice and simulating the correction procedure, and finally analyzing the dynamic aperture of the corrected lattice. The former is performed using `ring_ma2`; the latter is accomplished through tracking simulations also built on the `Bmad` accelerator code library [22, 49].

10.3.1 Misalignment and Correction

Characterizing the effects of misalignments and correction is again performed using `ring_ma2`, as discussed in Chapter 8. The optics correction procedure used in this characterization is the same as that used at CsrTA, described in Section 7.2. Typically 100 randomly-misaligned lattices are generated and then corrected in order to generate statistics sufficient for analysis.

Simulating the full correction procedure includes turn-by-turn tracking for several damping times in order to accurately simulate measurements of betatron phase and coupling, and is very time-consuming due to the number of elements in the lattice. The method for simulating measurements with BPM errors described in Chapter 8 is prohibitively slow for the ILC damping rings, requiring roughly one week for each misaligned and corrected lattice. In order to apply the characterization method developed in Chapter 8, two modifications have been made to the measurement simulation procedure.

First is a modification to tracking in the damping wigglers, which dominates the time required for simulating measurements. Comparisons of simulations using the full wiggler model and a reduced MAD-style “bend-drift-bend” wiggler have shown that wiggler nonlinearities in the full wiggler model do not significantly affect the corrections of optics functions or the final emittance.

Therefore, as a time-saving measure the simplified “bend-drift-bend” wiggler model is used for all `ring_ma2` studies on the ILC damping ring lattice. This reduces the time required to simulate the correction procedure for one randomly-misaligned lattice from roughly one week to twelve hours.

The second modification affects the process through which optics measurements are simulated. In Chapter 8, measurements are simulated on a turn-by-turn basis, applying BPM measurement errors on every turn. Simulating one betatron phase measurement requires tracking for roughly 150,000 turns. Even with the simplified wiggler model, this is prohibitively time-consuming on a lattice as large as DTC04. An alternative is used in these studies, where BPM errors are applied directly to the `Bmad`-computed optics functions. Although not as rigorous as the full measurement simulation method, side-by-side comparisons of the two methods have shown minimal difference in the resulting optics functions. As a result, the amount of time to simulate the correction procedure for one randomly-misaligned and corrected lattice is further reduced from roughly twelve hours to thirty minutes, allowing the characterization of each configuration to be completed in roughly 48 hours.

10.3.2 Dynamic Aperture

After a lattice model has been misaligned and corrected using the simulated emittance tuning procedure, dynamic aperture is evaluated. A trajectory is offset with some initial amplitude and tracked for 1000 turns. Initial amplitude offset is increased until the particle is lost within the 1000-turn window thus determining the maximum stable amplitude. The tracking is repeated for off-

energy particles to ensure the full bunch is accepted at injection. Results are then plotted in terms of normalized amplitudes A_x, A_y .

The full wiggler map is required for evaluating the dynamic aperture in order to account for wiggler nonlinearities. This greatly increases the required computation time for a dynamic aperture study, however the jobs are easily parallelized. With 45-node parallelization, dynamic aperture scans take roughly eight hours to complete when using the full wiggler map that includes all nonlinearities. Analysis has shown minimal variation of dynamic aperture between different sets of misalignments and corrections, given the same misalignment amplitudes, therefore only one seed for each test configuration is evaluated for dynamic aperture.

10.4 Error Tolerance of DTC04

The characterization method is now applied to the DTC04 lattice. Three scenarios are examined. First, the magnet misalignments, guide field errors, multipoles, and BPM measurement error tolerances specified in earlier studies [54] are applied, to demonstrate that the design satisfies the requirements for emittance and dynamic aperture. The second and third scenarios demonstrate two possible cost-saving measures: by reducing the number of BPMs, and by relaxing the specifications on guide field multipoles.

10.4.1 Nominal Lattice and Errors

Misalignments and BPM measurement error tolerances are summarized in Appendix E, Table E.4, and are based on errors used in previous studies [54], expanded to now include quadrupole k_1 and sextupole k_2 errors. Multipole coefficients are taken from Y. Cai's measurements of PEP-II guide field multipoles [59], and are summarized in Appendix E, Table E.5. Multipole coefficients are defined in the Bmad format (see Eqn. 2.13). These error amplitudes and multipole coefficients, along with the full complement of 511 BPMs, define the nominal ILC-DR scenario. Results of `ring_ma2` and dynamic aperture studies for this scenario are shown in Figures 10.4 and 10.5, respectively.

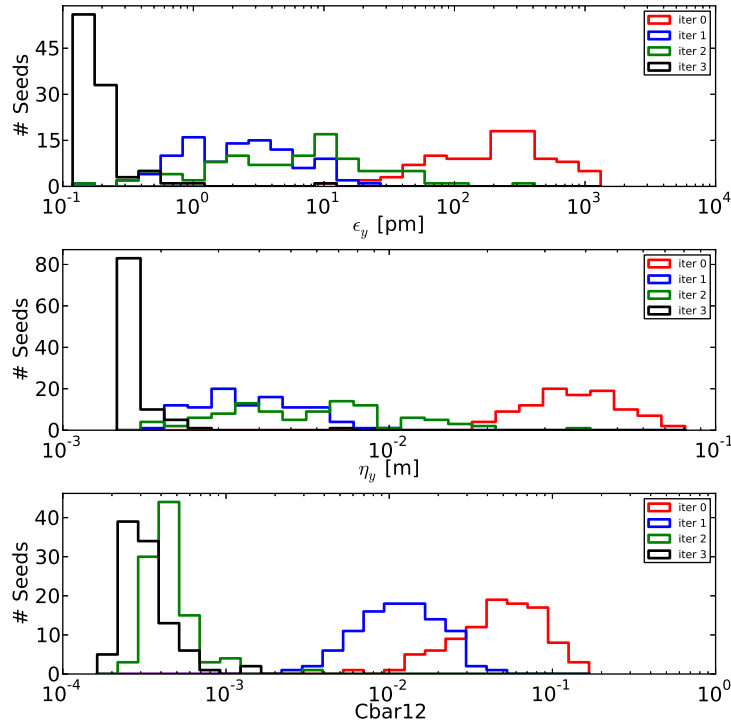


Figure 10.4: Distributions for emittance, dispersion, and coupling with misalignments, guide field multipoles, and BPM errors, using the full compliment of BPMs. Before correction (red), and after the first, second, and third corrections (blue, green, and black, respectively) are shown.

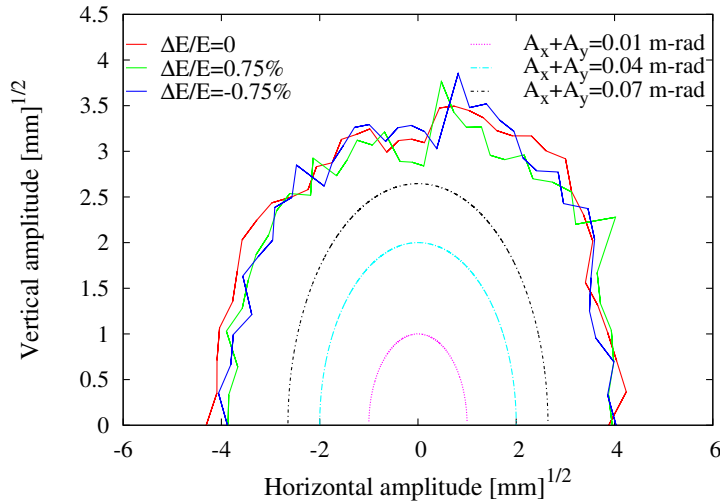


Figure 10.5: DTC04 dynamic aperture with nominal-amplitude misalignments, guide field multipoles, and BPM errors, using the full compliment of BPMs. The overlaid black ellipse represents the maximum amplitude for bunches transferred from the positron source.

Including misalignments, guide field errors, multipoles, and BPM measurement error tolerances, 95% of the resulting lattices have a vertical emittance below $\epsilon_y = 0.47$ pm after corrections. This is well below the emittance budget of $\epsilon_y = 2$ pm, though it is important to note that current-dependent effects and other non-static sources of emittance dilution have not been accounted for in the calculation of the simulated emittance. Additionally, the dynamic aperture is sufficiently large to accept the entire injected “hot” bunch from the positron source, even when accounting for all wiggler and multipole nonlinearities.

10.4.2 Reduced BPM Scheme

By reducing the number of BPMs in each arc cell from two to one, the total number of BPMs is reduced from 511 to 361. This represents a cost reduction of almost 30% for damping ring BPMs, making this an attractive cost-saving

measure.

Using the same amplitudes for errors as the nominal scenario, with the reduced BPM count, results for `ring_ma2` and dynamic aperture studies are shown in Figures 10.6 and 10.7, respectively.

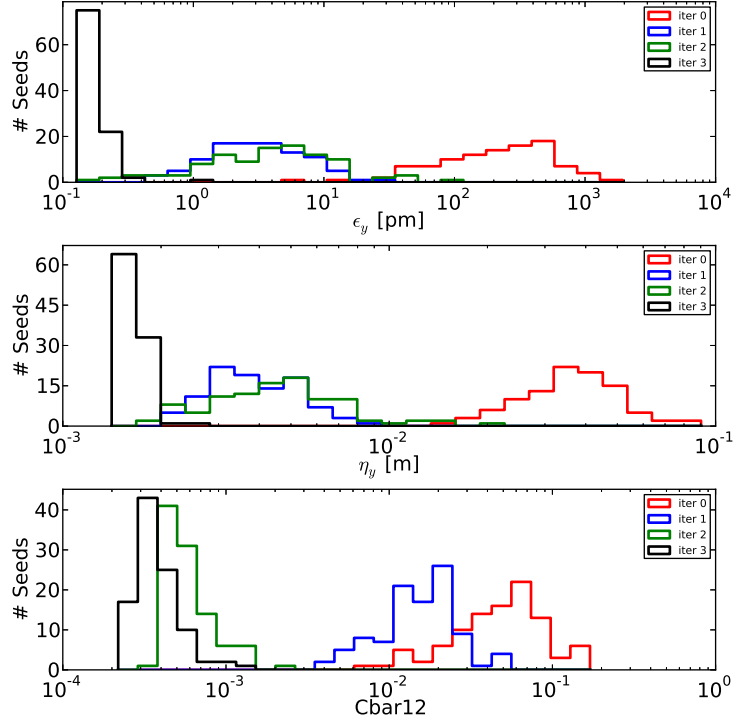


Figure 10.6: DTC04 emittance, dispersion, and coupling with nominal-amplitude misalignments, guide field multipoles, and BPM errors, with one of the two BPMs in each arc cell removed.

With the reduced BPM count, after corrections 95% of simulated lattices have a vertical emittance below $\epsilon_y = 0.25$ pm, consistent with the results when the full compliment of BPMs are used. Dynamic aperture is minimally affected. It is therefore feasible to remove half of the BPMs in the arc cells and maintain sufficient dynamic aperture and without compromising vertical emittance.

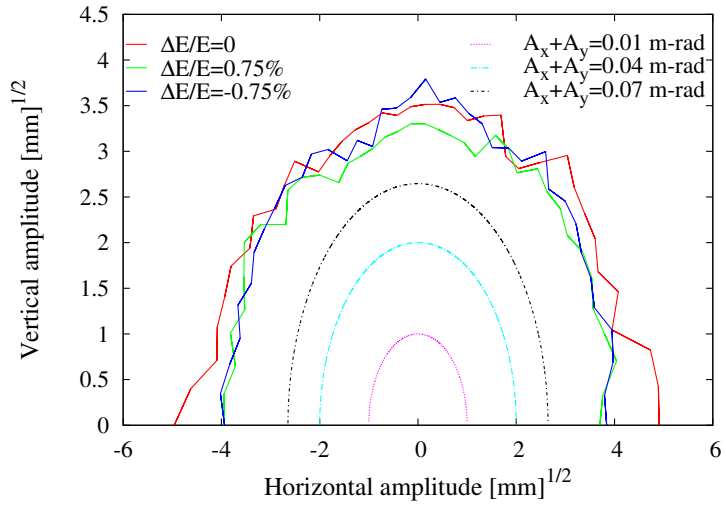


Figure 10.7: DTC04 dynamic aperture with nominal-amplitude misalignments, guide field multipoles, and BPM errors, with one of the two BPMs in each arc cell removed.

10.4.3 Increased Multipoles

Another cost saving measure could be to relax the tolerance on magnet multipole errors. Starting with the lattice with reduced BPM distribution from the previous section, both systematic and random multipole coefficients are increased by a factor of five. All other misalignments and BPM measurement errors are identical to the nominal scenario. Results for `ring_ma2` and dynamic aperture studies are shown in Figures 10.8 and 10.9, respectively.

With the relaxed constraints on multipole coefficients and reduced BPM count, 95% of simulated lattices have a vertical emittance below $\epsilon_y = 0.23$ pm after corrections, implying minimal impact of the multipoles on the emittance. Dynamic aperture is marginally affected, though it is not significant, implying that a further increase in multipole errors may be tolerable.

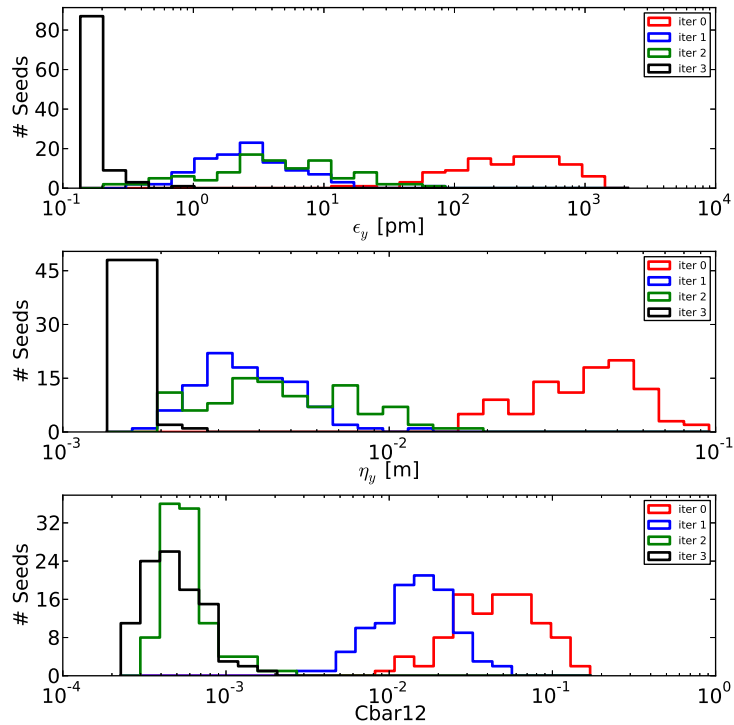


Figure 10.8: DTC04 emittance, dispersion, and coupling with multipole coefficients increased by a factor of five, and half of the arc BPMs removed.

10.5 Summary

Based on the work presented here, the DTC04 lattice achieves the required zero-current vertical emittance and dynamic aperture. The number of BPMs in the arcs can safely be reduced by 50% and specifications for magnet multipoles can be relaxed by a factor of five without compromising the effectiveness of the emittance tuning procedure or the dynamic aperture. This represents a significant potential cost-savings.

An infrastructure exists for evaluating further lattice modifications, such as sextupole optimizations, increased magnet or BPM errors, or a change in working point. Fully characterizing a new configuration takes approximately 48

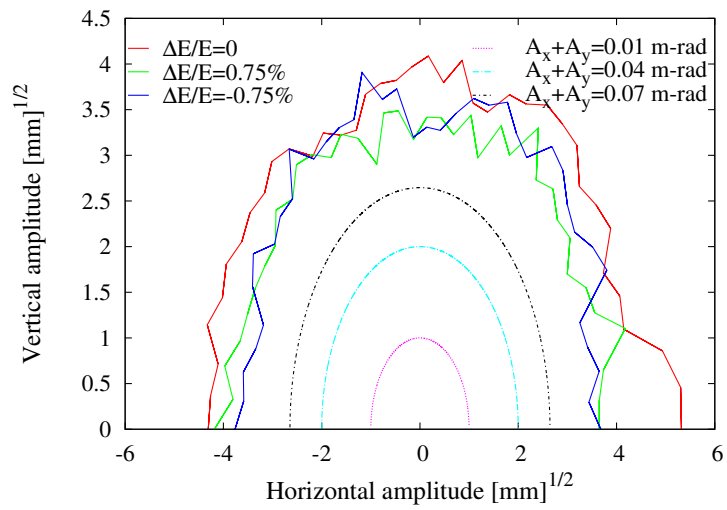


Figure 10.9: DTC04 dynamic aperture with multipole coefficients increased by a factor of five, and half of the arc BPMs removed.

hours when utilizing the Grid computing cluster [60].

CHAPTER 11

SUMMARY AND FUTURE WORK

11.1 Summary

An emittance correction technique with fast turnaround based on betatron phase and coupling measurements has been demonstrated at CEsrTA to achieve sub-10 pm vertical emittance. This represents the achievement of the CEsrTA Phase II emittance target. Simulations suggest that the contribution to the vertical emittance from misalignments, multipoles, field errors, and BPM measurement errors is around 4.1 pm or less, whereas the lowest measured vertical emittance at 2.085 GeV is $8.7 (+2.9/-3.4)^{sys} (\pm 0.2)^{stat}$ pm. From the agreement between measured and simulated optics functions (namely, dispersion and coupling), and from the completeness of the errors included in the simulations, it is not believed that static misalignments and optics errors are responsible for the discrepancy in the emittance. A substantial list of possible sources of emittance dilution have been eliminated as candidates.

Applying the misalignment and correction simulation methods to the ILC damping rings, the DTC04 lattice is shown to be correctable at the 95% confidence level to well below the emittance budget for the nominal amplitude of misalignments and errors, while maintaining sufficient dynamic aperture to accept the entire incoming bunch from the positron source. Furthermore, it has been shown that the number of BPMs in the arcs can be reduced by half and the multipole tolerances on quadrupoles and sextupoles can be relaxed by a factor of five without affecting either the emittance or the dynamic aperture.

11.2 Future Work

Further investigations will be necessary in diagnosing the residual vertical emittance.

The discrepancy in minimum-achieved vertical emittance in December 2012 and April 2013 is unresolved at this time. Differences in experimental setup between the two runs are primarily limited to total RF voltage and the quality of BPM-to-quadrupole centering, and do not appear to be sufficient to provide an explanation. The additional discrepancy between minimum-achieved vertical emittance for electrons and positrons is also unresolved, and implies some species dependence of the emittance. Candidates include wakefields or other collective effects, though these typically require significantly higher bunch current.

The energy dependence of the minimum-achieved emittance implies roughly 1/3 of the residual vertical emittance may be due to time-varying sources. Possible candidates are the RF system, including higher-order modes, beam loading, and input coupler effects, and time-varying sources which are not easily tested, such as magnet power supply choppers and the stability of the master oscillator.

From the potential current-dependence of the emittance, collective effects with a very low-current threshold cannot be eliminated as a possible source of emittance dilution, however no known collective effect has such a low current threshold while saturating well below 1.6×10^{10} particles/bunch.

If the as-yet-undetermined source (or sources) of emittance dilution can be

identified and eliminated, a vertical emittance below the ILC damping ring emittance budget of 2 pm is potentially achievable through a better characterization of BPM measurement errors. Pushing to within a factor of two of the quantum limit will require a more widespread reduction in errors, which may be achievable through modern survey and alignment techniques.

Further studies on optimizing the ILC damping rings lattice may prove beneficial in further relaxing the constraints for misalignments and multipoles. A more sophisticated sextupole distribution will likely increase the dynamic aperture even further, allowing more headroom for error tolerance.

APPENDIX A

PROPAGATING TUNE TRACKER PHASE

The power of the betatron phase and coupling measurements lies in the fact that the majority of the processing occurs in parallel onboard the individual BPM modules. As will be discussed in Appendix C, this mandates that the tune tracker phase is known at all BPMs on a turn-by-turn basis. The way this is done at CESR is to encode the betatron phase into the BPM clock signal.

The master clock in CESR is set to 71.4 MHz (for 14 ns bunch spacing), and is illustrated in Fig. A.1(a). The BPM clock is created from the master clock and runs at 1/3 this frequency, at 23.8 MHz. This means there are three “master clock” cycles for every “CBPM clock” cycle, and $2.56 \mu\text{s} \times 23.8 \text{ MHz} = 61$ “CBPM clock” cycles for each beam revolution in the storage ring.

In order to minimize dispersion effects in the cabling, the clock signal must average to zero. Additionally, the CBPM system requires a rising edge at 23.8 MHz. There are two clock signals which accomplish both of these objectives, illustrated in Fig. A.1(b-c). If each two-cycle BPM clock signal is treated as one bit, this allows for 30 bits of information to be transmitted to the BPM system on each turn. The horizontal and vertical tune tracker phases on every turn are encoded as nine bits each, for a total of 18 bits of information. The remaining 12 bits are used for synchronization and triggering signals.

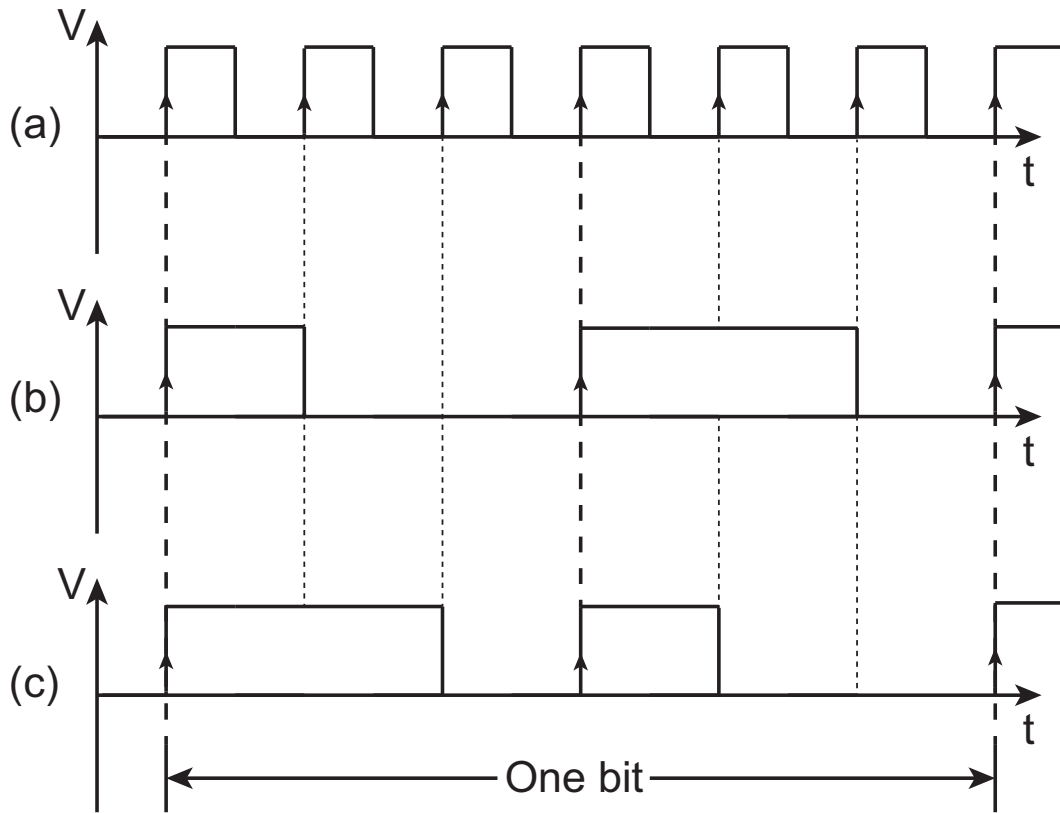


Figure A.1: An example of encoding the transverse tune tracker phases into the CBPM clock. (a) 71.4 MHz CESR master clock. (b-c) Two methods for constructing a 23.8 MHz BPM clock from the 71.4 MHz master clock. For both BPM clocks, it is necessary to maintain the average signal at $V/2$ to minimize dispersion, therefore a “short” pulse must always be accompanied by a “long” pulse. The two options allow for a single bit “0” or “1” to be encoded within two consecutive CESR clock cycles. There are 61 BPM clock cycles per revolution time ($2.56 \mu\text{s}$), therefore 30 bits can be encoded into the BPM clock signal. 9 bits are used to encode each of the two tune tracker drive phases; the remaining 12 bits are used for triggering and synchronization.

APPENDIX B

XBSM SOURCE POINT CALCULATIONS

This appendix outlines the procedure used for determining the exact source points for C-line and D-line during xBSM operation. Calculations account for all of the following:

- Surveyed locations for the xBSM detectors and optics boxes
- Real CESR orbitry from reference orbits
- Depth-of-field due to finite opening angle of radiation fan
- Longitudinal offset of the source dipole, from survey

B.1 Calculation Method

Both xBSM detectors (C-line and D-line) are routinely surveyed at the start of CesrTA runs. In February 2013 the locations of both optics boxes were also surveyed. All surveyed locations, in Lattice Coordinates (West = +x, North = +y), are shown in Table B.1.

Beamline	Detector Loc [m]	Optics Box Loc [m]
C-line	(8.657984, -2.252472)	(18.988971, 0.212821)
D-line	(-9.288702, -2.150914)	(-19.020430, 0.200139)

Table B.1: Surveyed locations for C- and D-line xBSMs, in Lattice Coordinates.

These surveyed locations produce a line, to which the CESR trajectory source point must be tangent. To determine the location of the source point:

1. Generate a model lattice with appropriate orbit in CESRv, using actual xBSM reference orbits. Export the model.
2. Read this model lattice with correct orbit into a secondary analysis program, `xbsm_sources`. This program steps through the dipole and determines the tangent to the orbit at a predetermined interval. Points with a tangent compatible with the beamline defined by the surveyed locations of the optics box and xBSM detector are flagged as source points.
3. Declare the source point to be the median location of all marked source points, and depth-of-field to be \pm (furthest source point - nearest source point) / 2.

The opening angle of the radiation fan is determined analytically:

$$\theta = \left(\frac{3\lambda}{2\pi\rho} \right)^{1/3} \quad (\text{B.1})$$

where $\lambda [\text{\AA}] \approx 12.4/E[\text{keV}]$. This is the full opening angle, therefore the convergence angle used in `xbsm_sources` is equal to this angle θ . For these calculations $E = 1 \text{ keV}$ was used, yielding a maximum opening angle $\theta = 0.265 \text{ mrad}$.

B.2 Results - December 2012 xBSM Reference Orbits

Using the above method, and using CesrTA xBSM reference orbits 804903 and 805323 for C-line and D-line respectively, the source points for C-line and D-line are computed, and are shown in Table B.2.

Beamline	Source Point [m]	DOF [m]
C-line	(23.361685, 1.255166)	± 0.008258
D-line	(-23.519680, 1.287832)	± 0.0080951

Table B.2: xBSM source points and depth of field (DOF), in Lattice Coordinates.

Note that these numbers do NOT include the surveyed longitudinal dipole offsets (-5.6 mm for C-line, +2.4 mm for D-line). Including these adjustments, the resulting source-to-optic, optic-to-detector, and magnifications are shown in table B.3. The confidence intervals for magnification are set by the depth-of-field. Plots demonstrating the level of agreement between the projected CHES beamline and CESR xBSM reference orbit from December 2012 are shown in Figures B.1 and B.2.

Beamline	Source-Optic [m]	Optic-Detector [m]	Magnification
C-line	4.4896	10.6211	2.3657 ± 0.0043
D-line	4.6313	10.0117	2.1640 ± 0.0038

Table B.3: C-line and D-line values for December 2012 and newer, using survey results and CESR orbitry. These are valid to use in analysis of data from December 2012 on.

B.3 Effect of Reference Orbit

The calculations can be repeated for using a flat (on-axis) orbit and CHES pretzel orbit. These results have been compiled into Tables B.4 and B.5.

Reference Orbit	Source-Optic [m]	Optic-Detector [m]	Magnification
xBSM Orbit	4.48963	10.6211	2.3657 ± 0.0043
Flat Orbit	4.56021	10.6211	2.3292 ± 0.0042
CHES Orbit	4.46227	10.6211	2.3802 ± 0.0043

Table B.4: C-line - effect of reference orbit on source point and magnification.

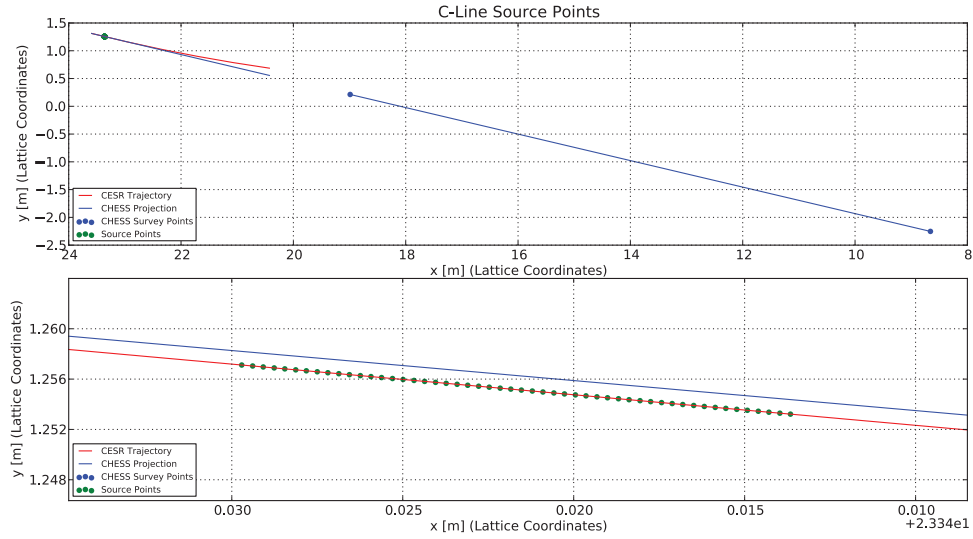


Figure B.1: Plots demonstrating the locations of the xBSM source points for C-line. The bottom plot is the same as the top plot, zoomed in to the source points.

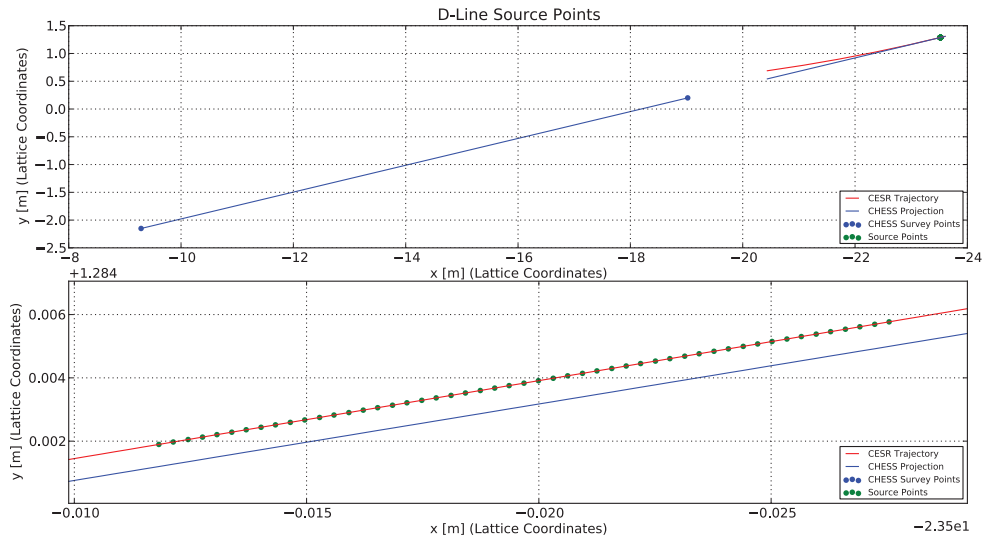


Figure B.2: Plots demonstrating the locations of the xBSM source points for D-line. The bottom plot is the same as the top plot, zoomed in to the source points.

To summarize: By including the effect of the xBSM reference orbit, rather than using the on-axis "10 mrad" line, there is a correction to the magnification of 1.7% for C-line and $< 0.1\%$ for D-line.

Reference Orbit	Source-Optic [m]	Optic-Detector [m]	Magnification
xBSM Orbit	4.62646	10.0117	2.1640 ± 0.0038
Flat Orbit	4.62854	10.0117	2.1630 ± 0.0039
CHESS Orbit	4.53383	10.0117	2.2082 ± 0.0039

Table B.5: D-line - effect of reference orbit on source point and magnification.

B.4 Sensitivity to Errors

Also of interest is how sensitive the calculation is to variations in the surveyed optics and reference orbit. Two additional tests were performed using the new December 2012 D-line results as a baseline. First, the survey locations of the optics box and detector were transversely offset by ± 1 mm in opposite directions (in order to maximize the angular error). Second, the xBSM reference orbit was altered by $\pm 50 \mu\text{m}$ at BPMs 5E and 4E, to estimate the repeatability of the magnification throughout the course of a CesrTA run.

Results from both of these studies are shown in Table B.6.

Error	Source-Optic [m]	Optic-Detector [m]	Magnification
Surveys Offset	4.6377	10.0122	2.1589 ± 0.0038
Orbit varied	4.6383	10.0117	2.1586 ± 0.0038

Table B.6: D-line - effect of various errors on the magnification. In the first scenario the surveyed locations of the detector and optics box are offset by ± 1 mm transversely. In the second, the orbit is varied by $\pm 50 \mu\text{m}$ at the BPMs adjacent to the source dipole.

The conclusion is that both errors are below 0.25% effect on the magnification.

APPENDIX C
PROCESSING OF PHASE DATA

On each button i at each BPM, a running sum is recorded over turns j to determine the in-phase and out-of-phase components of the measured button signals $b_{i,j}$ with respect to the turn-by-turn drive phases $\varphi_{(a,b),j}^{ref}$:

$$A_{i,in} = \sum_j b_{i,j} \sin \varphi_{a,j}^{ref} \quad (C.1)$$

$$A_{i,out} = \sum_j b_{i,j} \cos \varphi_{a,j}^{ref} \quad (C.2)$$

$$B_{i,in} = \sum_j b_{i,j} \sin \varphi_{b,j}^{ref} \quad (C.3)$$

$$B_{i,out} = \sum_j b_{i,j} \cos \varphi_{b,j}^{ref} \quad (C.4)$$

where A, B are the amplitudes of the a - and b -mode motion, respectively. When the summation is complete, the button-by-button relative phase and amplitude with respect to the drive signal are then calculated:

$$\phi_{a,i} = \tan^{-1} \frac{A_{i,in}}{A_{i,out}} \quad (C.5)$$

$$\phi_{b,i} = \tan^{-1} \frac{B_{i,in}}{B_{i,out}} \quad (C.6)$$

$$A_i = \sqrt{A_{i,in}^2 + A_{i,out}^2} \quad (C.7)$$

$$B_i = \sqrt{B_{i,in}^2 + B_{i,out}^2} \quad (C.8)$$

These values are then sent from the BPM modules to the server, which in turn commits them to file.

In post-process, the a - and b -mode phase in both the horizontal and vertical response at each BPM (modulo 2π) is determined by averaging the four measured phases:

$$\phi_{a,x} = \frac{(\phi_{a,2} + \phi_{a,4}) - (\phi_{a,1} + \phi_{a,3})}{4} \quad (\text{C.9})$$

$$\phi_{a,y} = \frac{(\phi_{a,3} + \phi_{a,4}) - (\phi_{a,1} + \phi_{a,2})}{4} \quad (\text{C.10})$$

$$\phi_{b,x} = \frac{(\phi_{b,2} + \phi_{b,4}) - (\phi_{b,1} + \phi_{b,3})}{4} \quad (\text{C.11})$$

$$\phi_{b,y} = \frac{(\phi_{b,3} + \phi_{b,4}) - (\phi_{b,1} + \phi_{b,2})}{4} \quad (\text{C.12})$$

$\phi_{a,x}$ and $\phi_{b,y}$ are the values reported as the “horizontal” and “vertical” phase. Note that for the horizontal phase, the left and right pairs of buttons are 180 degrees out of phase; similarly, for the vertical phase, the top and bottom pairs buttons are 180 degrees out of phase. Hence, the out-of-phase button phases are subtracted. The absolute phase is then computed by adding factors of 2π until the measured phase is within π of the design phase. This assumes that the phase advance between detectors is much less than 2π , and that the maximum phase error is less than π . In practice these are both safe assumptions. For CsrTA, the horizontal and vertical tunes are approximately $Q_{x,y} = (14.59, 9.63)$, or $\nu_{x,y} = (91.63, 60.48)$ rad. For 100 BPMs spaced roughly evenly, this yields a maximum phase advance per BPM of approximately 0.9 rad.

The measurable elements of the coupling matrix $\bar{\mathbf{C}}$ are then calculated in post-process. First, the measured button-by-button phase and amplitude must be converted from the 16 measured phases and amplitudes ($\phi_{a,i}, \phi_{b,i}, A_i, B_i$) to the four lab-coordinate amplitudes (A_x, A_y, B_x, B_y). To do this, first the total amplitudes must be deconstructed back into the button-by-button in-phase and

out-of-phase amplitudes (effectively reversing Equations C.7-C.8):

$$A_{i,in} = A_i \cos \phi_{a,i} \quad (\text{C.13})$$

$$A_{i,out} = A_i \sin \phi_{a,i} \quad (\text{C.14})$$

$$B_{i,in} = B_i \cos \phi_{b,i} \quad (\text{C.15})$$

$$B_{i,out} = B_i \sin \phi_{b,i} \quad (\text{C.16})$$

Each of these equations represents a set of four button amplitude, which can be interpreted as an overall amplitude of that mode, and can be converted into x,y amplitudes through `nonlin_bpm`. This yields 8 amplitudes: the in- and out-of-phase components, in x and y , for the a - and b - modes. The in- and out-of-phase components are then recombined into total amplitudes:

$$A_x = \sqrt{A_{x,in}^2 + A_{x,out}^2} \quad (\text{C.17})$$

$$A_y = \sqrt{A_{y,in}^2 + A_{y,out}^2} \quad (\text{C.18})$$

$$B_x = \sqrt{B_{x,in}^2 + B_{x,out}^2} \quad (\text{C.19})$$

$$B_y = \sqrt{B_{y,in}^2 + B_{y,out}^2} \quad (\text{C.20})$$

The coupling matrix elements can now be calculated. The out-of-phase component \bar{C}_{12} can be computed two ways: through the component of the a -mode in the vertical which is out-of-phase with the horizontal, and the component of the b -mode in the horizontal which is out-of-phase with the vertical:

$$\bar{C}_{12} = \frac{A_y / \sqrt{\beta_b}}{A_x / \sqrt{\beta_a}} \sin(\phi_{a,y} - \phi_{a,x}) \quad (\text{C.21})$$

$$\bar{C}_{12} = \frac{B_x / \sqrt{\beta_a}}{B_y / \sqrt{\beta_b}} \sin(\phi_{b,x} - \phi_{b,y}) \quad (\text{C.22})$$

where the amplitudes are from Equations C.17-C.20, phases are from Equations C.9-C.12, and the beta functions are taken from the design lattice and assumed correct.

Similarly, the in-phase components are calculated by:

$$\bar{C}_{22} = \frac{A_y / \sqrt{\beta_b}}{A_x / \sqrt{\beta_a}} \cos(\phi_{a,y} - \phi_{a,x}) \quad (\text{C.23})$$

$$\bar{C}_{11} = \frac{B_x / \sqrt{\beta_a}}{B_y / \sqrt{\beta_b}} \cos(\phi_{b,x} - \phi_{b,y}) \quad (\text{C.24})$$

APPENDIX D
EFFECTS OF BPM TILT ON BETATRON PHASE AND COUPLING
MEASUREMENTS

Start by considering the horizontal and vertical positions of a resonantly-excited beam, in terms of the coupling \bar{C} :

$$\begin{pmatrix} x \\ y \end{pmatrix} = A \begin{pmatrix} \gamma \sqrt{\beta_a} \cos \psi_a \\ -\sqrt{\beta_b} [\bar{C}_{22} \cos \psi_a + \bar{C}_{12} \sin \psi_a] \end{pmatrix} + B \begin{pmatrix} \sqrt{\beta_a} [\bar{C}_{11} \cos \psi_b - \bar{C}_{12} \sin \psi_b] \\ \gamma \sqrt{\beta_b} \cos \psi_b \end{pmatrix} \quad (\text{D.1})$$

where no assumptions are made about the state of the coupling between horizontal and vertical motion (aside from those required in order to use the \bar{C} formalism), and A, B are the amplitudes of the a- and b-mode motions respectively. $\psi_{a,b}$ is the total phase advance in each mode. This can be rephrased as:

$$\begin{pmatrix} x \\ y \end{pmatrix} = \begin{pmatrix} A_x^{in} \cos \psi_a \\ A_y^{in} \cos \psi_a + A_y^{out} \sin \psi_a \end{pmatrix} + \begin{pmatrix} B_x^{in} \cos \psi_b + B_x^{out} \sin \psi_b \\ B_y^{in} \cos \psi_b \end{pmatrix} \quad (\text{D.2})$$

$$= \begin{pmatrix} A_x^{in} & 0 \\ A_y^{in} & A_y^{out} \end{pmatrix} \begin{pmatrix} \cos \psi_a \\ \sin \psi_a \end{pmatrix} + \begin{pmatrix} B_x^{in} & B_x^{out} \\ B_y^{in} & 0 \end{pmatrix} \begin{pmatrix} \cos \psi_b \\ \sin \psi_b \end{pmatrix} \quad (\text{D.3})$$

where the amplitudes of motion are defined as in-phase and out-of-phase with the primary motion of that mode. The frequencies of the two modes are assumed sufficiently different such that we may distinguish the modes, and may consider them separately.

Applying a physical rotation of the coordinate system, corresponding to a tilt of the BPM:

$$\begin{pmatrix} x \\ y \end{pmatrix}^{obs} = R_\theta \begin{pmatrix} A_x^{in} & 0 \\ A_y^{in} & A_y^{out} \end{pmatrix} \begin{pmatrix} \cos \psi_a \\ \sin \psi_a \end{pmatrix} + R_\theta \begin{pmatrix} B_x^{in} & B_x^{out} \\ B_y^{in} & 0 \end{pmatrix} \begin{pmatrix} \cos \psi_b \\ \sin \psi_b \end{pmatrix} \quad (D.4)$$

$$\begin{aligned} &= \begin{pmatrix} \cos \theta & \sin \theta \\ -\sin \theta & \cos \theta \end{pmatrix} \begin{pmatrix} A_x^{in} & 0 \\ A_y^{in} & A_y^{out} \end{pmatrix} \begin{pmatrix} \cos \psi_a \\ \sin \psi_a \end{pmatrix} \\ &+ \begin{pmatrix} \cos \theta & \sin \theta \\ -\sin \theta & \cos \theta \end{pmatrix} \begin{pmatrix} B_x^{in} & B_x^{out} \\ B_y^{in} & 0 \end{pmatrix} \begin{pmatrix} \cos \psi_b \\ \sin \psi_b \end{pmatrix} \end{aligned} \quad (D.5)$$

$$\begin{aligned} &= \begin{pmatrix} A_x^{in} \cos \theta + A_y^{in} \sin \theta & A_y^{out} \sin \theta \\ -A_x^{in} \sin \theta + A_y^{in} \cos \theta & A_y^{out} \cos \theta \end{pmatrix} \begin{pmatrix} \cos \psi_a \\ \sin \psi_a \end{pmatrix} \\ &+ \begin{pmatrix} B_x^{in} \cos \theta + B_y^{in} \sin \theta & B_x^{out} \cos \theta \\ -B_x^{in} \sin \theta + B_y^{in} \cos \theta & -B_x^{out} \sin \theta \end{pmatrix} \begin{pmatrix} \cos \psi_b \\ \sin \psi_b \end{pmatrix} \end{aligned} \quad (D.6)$$

$$= \begin{pmatrix} A_x^{in,obs} & A_x^{out,obs} \\ A_y^{in,obs} & A_y^{out,obs} \end{pmatrix} \begin{pmatrix} \cos \psi_a \\ \sin \psi_a \end{pmatrix} + \begin{pmatrix} B_x^{in,obs} & B_x^{out,obs} \\ B_y^{in,obs} & B_y^{out,obs} \end{pmatrix} \begin{pmatrix} \cos \psi_b \\ \sin \psi_b \end{pmatrix} \quad (D.7)$$

The label “*obs*” indicates “observed”, i.e., in the rotated coordinate system.

To better see the components of the observed vertical motion in-phase and out-of-phase with the observed horizontal motion (and vice-versa), a second transform is required, to the form:

$$\begin{pmatrix} x \\ y \end{pmatrix}^{obs} = \begin{pmatrix} \tilde{A}_x^{in} & 0 \\ \tilde{A}_y^{in} & \tilde{A}_y^{out} \end{pmatrix} \begin{pmatrix} \cos \xi_a \\ \sin \xi_a \end{pmatrix} + \begin{pmatrix} \tilde{B}_x^{in} & \tilde{B}_x^{out} \\ \tilde{B}_y^{in} & 0 \end{pmatrix} \begin{pmatrix} \cos \xi_b \\ \sin \xi_b \end{pmatrix} \quad (D.8)$$

Starting with the a-mode, the horizontal motion transforms as:

$$A_x^{in,obs} \cos \psi_a + A_x^{out,obs} \sin \psi_a = \tilde{A}_x^{in} \cos \xi_a \quad (\text{D.9})$$

where

$$\tilde{A}_x^{in} = \sqrt{(A_x^{in,obs})^2 + (A_x^{out,obs})^2} \quad (\text{D.10})$$

$$\xi_a = \psi_a + \varphi_a \quad (\text{D.11})$$

$$\varphi_a = \text{sgn}(A_x^{in,obs}) \cos^{-1} \left(\frac{A_x^{out,obs}}{\sqrt{(A_x^{in,obs})^2 + (A_x^{out,obs})^2}} \right) - \frac{\pi}{2} \quad (\text{D.12})$$

The identity used for this transformation shifts to sine, but it is more convenient to work with only a cosine component in the horizontal, hence the $\pi/2$ phase shift. The vertical motion of the a-mode must be projected into this basis:

$$A_y^{in,obs} \cos \psi_a + A_y^{out,obs} \sin \psi_a = \tilde{A}_y^{in} \cos \xi_a + \tilde{A}_y^{out} \sin \xi_a \quad (\text{D.13})$$

$$= \tilde{A}_y^{in} \cos(\psi_a + \varphi_a) + \tilde{A}_y^{out} \sin(\psi_a + \varphi_a) \quad (\text{D.14})$$

$$= \tilde{A}_y^{in} (\cos \psi_a \cos \varphi_a - \sin \psi_a \sin \varphi_a) + \tilde{A}_y^{out} (\sin \psi_a \cos \varphi_a + \cos \psi_a \sin \varphi_a) \quad (\text{D.15})$$

$$= (\tilde{A}_y^{in} \cos \varphi_a + \tilde{A}_y^{out} \sin \varphi_a) \cos \psi_a + (-\tilde{A}_y^{in} \sin \varphi_a + \tilde{A}_y^{out} \cos \varphi_a) \sin \psi_a \quad (\text{D.16})$$

Utilizing the orthogonality of $\cos \psi_a$ and $\sin \psi_a$, there is now a system of two equations and two unknowns:

$$\begin{pmatrix} A_y^{in,obs} \\ A_y^{out,obs} \end{pmatrix} = \begin{pmatrix} \cos \varphi_a \tilde{A}_y^{in} + \sin \varphi_a \tilde{A}_y^{out} \\ -\sin \varphi_a \tilde{A}_y^{in} + \cos \varphi_a \tilde{A}_y^{out} \end{pmatrix} \quad (\text{D.17})$$

$$= \begin{pmatrix} \cos \varphi_a & \sin \varphi_a \\ -\sin \varphi_a & \cos \varphi_a \end{pmatrix} \begin{pmatrix} \tilde{A}_y^{in} \\ \tilde{A}_y^{out} \end{pmatrix} \quad (\text{D.18})$$

$$\begin{pmatrix} A_y^{in,obs} \\ A_y^{out,obs} \end{pmatrix} = R_{\varphi_a} \begin{pmatrix} \tilde{A}_y^{in} \\ \tilde{A}_y^{out} \end{pmatrix} \quad (\text{D.19})$$

In this form, it is trivial to invert the system:

$$\begin{aligned} \begin{pmatrix} \tilde{A}_y^{in} \\ \tilde{A}_y^{out} \end{pmatrix} &= R_{-\varphi_a} \begin{pmatrix} A_y^{in,obs} \\ A_y^{out,obs} \end{pmatrix} \\ &= \begin{pmatrix} \cos \varphi_a A_y^{in,obs} - \sin \varphi_a A_y^{out,obs} \\ \sin \varphi_a A_y^{in,obs} + \cos \varphi_a A_y^{out,obs} \end{pmatrix} \end{aligned} \quad (\text{D.20})$$

Equation D.7 has now been rephrased in terms of the new basis $(\tilde{A}_{x,y}^{in,out}, \xi_a)$. The procedure is identical for the vertical motion, and will not be shown here.

The *observed* coupling matrix elements $\bar{C}_{22,12,11}$ may now be written:

$$\begin{aligned} \bar{C}_{22}^{obs} &= -\gamma \sqrt{\frac{\beta_a \tilde{A}_y}{\beta_b \tilde{A}_x}} \cos \Delta\tilde{\phi}_a \\ \bar{C}_{12}^{obs} &= -\gamma \sqrt{\frac{\beta_a \tilde{A}_y}{\beta_b \tilde{A}_x}} \sin \Delta\tilde{\phi}_a \\ \bar{C}_{11}^{obs} &= \gamma \sqrt{\frac{\beta_b \tilde{B}_x}{\beta_a \tilde{B}_y}} \cos \Delta\tilde{\phi}_b \end{aligned} \quad (\text{D.21})$$

where

$$\tilde{A}_x = \sqrt{(\tilde{A}_x^{in})^2 + (\tilde{A}_x^{out})^2}, \text{ etc.} \quad (\text{D.22})$$

$$\Delta\tilde{\phi}_a = \tan^{-1}\left(\frac{\tilde{A}_y^{out}}{\tilde{A}_y^{in}}\right) \quad (D.23)$$

$$\Delta\tilde{\phi}_b = \tan^{-1}\left(\frac{\tilde{B}_x^{out}}{\tilde{B}_x^{in}}\right) \quad (D.24)$$

and \tilde{A}_x^{in} , etc., are defined by equation D.20.

Applying this formalism to fit existing coupling data for BPM tilts, the procedure would be:

1. Start with defining the in-phase and out-of-phase of horizontal and vertical motion in the a- and b-modes, as per equation D.3, and apply the tilt to generate equation D.7
2. Phase-shift the primary motion in each plane such that it is only defined as a cosine (equation D.9), and project that mode's motion in the other plane into this basis (equation D.20)
3. These projected amplitudes may then be used in the final definitions of the coupling matrix elements (equations D.21), with the help of equations D.22 - D.24

APPENDIX E

ERRORS FOR RING_MA2 SIMULATIONS

E.1 CsrTA

Table E.1 shows the misalignments and errors used in CsrTA ring_ma2 studies. Offsets of quadrupoles and sextupoles include measured alignment levels along with $100\ \mu\text{m}$ added in quadrature to account for the estimated uncertainty in the offset of magnetic center with respect to geometric center of these elements.

Systematic multipoles are included for sextupoles which have vertical steering or skew quadrupole trim windings. These multipoles are computed using field modeling software, and are scaled to a measurement radius of 20 mm. There is also a known skew quadrupole component to the damping wiggler fields [56], due to manufacturing tolerances in the radii of the pole windings. This has also been accounted for, using a measurement radius of 1 m for input into Bmad. Multipoles used in this study are summarized in Table E.3.

E.2 ILC Damping Ring

The magnet misalignments and field errors used in the ILC damping ring studies are summarized in Table E.4. Systematic and random multipoles are based on Y. Cai's multipole measurements at PEP-II [59], and are summarized in Table E.5.

Element Class	Error	Applied RMS	Units	Source
Dipole	x Offset	0.9	[mm]	Survey
	y Offset	2.0	[mm]	Survey
	s Offset	2.3	[mm]	Survey
	Roll	144	[μ rad]	Survey
	x Pitch	600	[μ rad]	Survey
	y Pitch	300	[μ rad]	Survey
	Quadrupole	x Offset	350	[μ m]
y Offset		107.8	[μ m]	Survey
s Offset		5.2	[mm]	Survey
Tilt		148	[μ rad]	Survey
x Pitch		1100	[μ rad]	Survey
y Pitch		62	[μ rad]	Survey
k1		0.1%	[%]	Estimate
Sextupole	x Offset	300	[μ m]	Estimate
	y Offset	300	[μ m]	Estimate
	s Offset	5.2	[mm]	Estimate
	Tilt	200	[μ rad]	Survey
	x Pitch	1200	[μ rad]	Estimate
	y Pitch	800	[μ rad]	Estimate
	k2	0.1%	[%]	Estimate
Wiggler	x Offset	1	[mm]	Survey
	y Offset	250	[μ m]	Survey
	s Offset	500	[μ m]	Estimate
	Tilt	300	[μ rad]	Survey
	x Pitch	200	[μ rad]	Estimate
	y Pitch	250	[μ rad]	Estimate

Table E.1: Misalignments and errors introduced into model CesrTA lattice for `ring_ma2` studies. All parameters are determined either from machine measurements or survey; parameters labeled as “estimate” are estimated from a small sample size (about 10) of surveyed elements.

Error	Applied RMS	Units
Reproducibility	10	[μm]
Tilt	12	[mrad]
Gains	0.5%	[%]
Timing	10	[ps]
Offset (x, y)	170	[μm]
Horizontal Shear	± 100	[μm]

Table E.2: BPM errors introduced into model CesrTA lattice for `ring_ma2` studies.

Element Class	Multipole	Value
Sextupole with Vert. Steering	a3	-7.25×10^{-4}
	a5	-1.46×10^{-2}
	a7	6.68×10^{-4}
	a9	8.7×10^{-6}
	a11	1.0×10^{-5}
Sextupole with Skew Quad Trim	a4	-1.2145×10^{-1}
	a6	2.16×10^{-4}
	a8	4.96×10^{-4}
	a10	-2.29×10^{-5}
	a12	-1.0×10^{-5}
Wiggler	a1	2.88×10^{-4}

Table E.3: Multipoles used in `ring_ma2` studies of CesrTA lattice. Sextupole multipoles are systematic and therefore identical at all sextupoles, whereas the wiggler $a1$ multipole is random; the number quoted for wiggler $a1$ is therefore the RMS of the applied distribution.

Element	Error	Amplitude	Units
Quadrupole	x,y offset	25	[μm]
	Tilt	50	[μrad]
	k1	0.1%	[%]
Dipole	roll	50	[μrad]
Sextupole	x,y offset	25	[μm]
	tilt	25	[μrad]
	k2	1%	[%]
Wiggler	tilt	100	[μrad]
	y offset	100	[μm]
BPM	Diff. Resolution	1	[μm]
	Abs. Resolution	50	[μm]
	Tilt	10	[mrad]
	Button Gains	0.5%	[%]
	Button Timing	10	[ps]

Table E.4: Misalignments and errors introduced into the model ILC-DR lattice.

Element	Multipole	Systematic	Random
Dipole	b2	1.6×10^{-4}	8×10^{-5}
	b3	-1.6×10^{-5}	8×10^{-6}
	b4	7.6×10^{-5}	3.8×10^{-5}
Quadrupole	a2	-1.15×10^{-5}	7.25×10^{-5}
	a3	1.41×10^{-5}	1.27×10^{-4}
	a4	6.2×10^{-7}	1.62×10^{-5}
	a5	-4.93×10^{-5}	3.63×10^{-4}
	a6	-1.02×10^{-6}	6.6×10^{-6}
	a7	3.8×10^{-7}	6.6×10^{-6}
	a8	-2.8×10^{-7}	4.9×10^{-6}
	a9	-5.77×10^{-5}	2.33×10^{-4}
	a10	-3.8×10^{-7}	3.5×10^{-6}
	a11	-6.53×10^{-6}	3.66×10^{-5}
	a12	1.2×10^{-6}	8.6×10^{-6}
	a13	-7.4×10^{-7}	4.46×10^{-5}
	b2	-1.24×10^{-5}	7.61×10^{-5}
	b3	2.3×10^{-6}	1.32×10^{-4}
	b4	-4.3×10^{-6}	1.5×10^{-5}
	b5	3.4×10^{-4}	1.65×10^{-4}
	b6	3×10^{-7}	6.7×10^{-6}
	b7	6×10^{-7}	8.9×10^{-6}
	b8	6×10^{-7}	4.6×10^{-6}
	b9	-6.17×10^{-5}	2.46×10^{-4}
b10	-2×10^{-7}	4.2×10^{-6}	
b11	3.6×10^{-6}	3.48×10^{-5}	
b12	6×10^{-7}	9.2×10^{-6}	
b13	1×10^{-6}	4.76×10^{-5}	
Sextupole	b3	1×10^{-4}	1×10^{-4}
	b4	5×10^{-5}	3×10^{-5}
	b5	3.5×10^{-4}	1×10^{-4}
	b6	5×10^{-5}	3×10^{-5}
	b7	5×10^{-5}	3×10^{-5}
	b8	5×10^{-5}	3×10^{-5}
	b9	5×10^{-5}	3×10^{-5}
	b10	5×10^{-5}	3×10^{-5}
	b11	1.6×10^{-3}	1×10^{-4}
	b12	5×10^{-5}	3×10^{-5}
b13	5×10^{-5}	3×10^{-5}	

Table E.5: Nominal multipoles (systematic and random) introduced into the model lattice. Coefficients are taken from Y. Cai's multipole measurements at PEP-II [59].

APPENDIX F

ENERGY DEPENDENCE OF THE VERTICAL EMITTANCE

In this appendix, the energy dependence for contributions to the vertical emittance are derived. Since the magnetic field in the damping wigglers is constant, the beam rigidity (Eqn. 2.23) indicates that the bending radius $\rho_w \propto E_0$. Therefore, care must be taken to separate contributions from the dipoles and damping wigglers.

F.1 Energy Dependence of Radiation Integrals in Wigglers

As will become evident in subsequent sections, the dependence of the emittance on energy can be described through the dependencies of contributions to the radiation integrals. It is therefore convenient to preemptively discuss how the necessary radiation integrals ($I_2, I_3, I_{4,b}, I_{5,b}$) will vary with energy.

All radiation integrals are path integrals around the ring. The path integrals can be computed piecewise over elements j :

$$I_i = \oint_0^S f(s') ds' \quad (\text{F.1})$$

$$= \sum_j \oint_{s_{0,j}}^{S_j} f(s') ds' \quad (\text{F.2})$$

The sum can therefore be split into wiggler terms and non-wiggler terms:

$$I_i = \sum_w \oint_{s_{0,w}}^{S_w} f(s') ds' + \sum_d \oint_{s_{0,d}}^{S_d} f(s') ds' \quad (\text{F.3})$$

$$= I_i^W + I_i^D \quad (\text{F.4})$$

where the indices d, D imply that the vast majority of non-wiggler contributions to the radiation integrals are dipoles. The first sum will depend on energy, whereas (because the dipole strength determines the beam energy) the second sum will not.

It is trivial to show $I_2^W \propto 1/E_0^2$ and $I_3^W \propto 1/E_0^3$. However, the energy dependencies for $I_{4,b}^W$ and $I_{5,b}^W$ are not as immediately evident. Additionally, $I_{4,b}$ and $I_{5,b}$ will depend on the specific corrections in the lattice, whereas I_2 and I_3 are properties of the design lattice. Recall the definition of $I_{4,b}$ when integrating only over wiggler contributions:

$$I_{4,b}^W = \oint_{\text{wiggles}} (g_w^2 \mathbf{g}_w \cdot \boldsymbol{\eta}_b + \nabla g_w^2 \cdot \boldsymbol{\eta}_b) ds \quad (\text{F.5})$$

For the wigglers, $|g_w| = 1/\rho_w \propto 1/E$. Ideally, $\boldsymbol{\eta}_b$ would be zero, as the damping wigglers do not introduce b -mode dispersion. However, there will be vertical dispersion from misalignments and errors in the ring; from experience during machine tuning, the minimum vertical dispersion after optics corrections does not depend on energy. Therefore, $I_{4,b}^W \propto 1/E_0^2$.

Similarly, for $I_{5,b}^W$:

$$I_{5,b}^W = \oint_{\text{wiggles}} g_w^3 \mathcal{H}_b ds \quad (\text{F.6})$$

$$\mathcal{H}_b = \gamma_b \eta_b^2 + 2\alpha_b \eta_b \eta'_b + \beta_b \eta'^2_b \quad (\text{F.7})$$

Again, the vertical dispersion inside the wigglers will be dominated by misalignments and field errors which are independent of energy. Therefore, $I_{5,b}^W \propto 1/E^3$.

The radiation integrals are therefore normalized to have the following form:

$$I_2^{E_0} = I_2^{D, 2.085} + \left(\frac{2.085}{E_0}\right)^2 I_2^{W, 2.085} \quad (\text{F.8})$$

$$I_3^{E_0} = I_3^{D, 2.085} + \left(\frac{2.085}{E_0}\right)^3 I_3^{W, 2.085} \quad (\text{F.9})$$

$$I_{4,b}^{E_0} = I_{4,b}^{D, 2.085} + \left(\frac{2.085}{E_0}\right)^2 I_{4,b}^{W, 2.085} \quad (\text{F.10})$$

$$I_{5,b}^{E_0} = I_{5,b}^{D, 2.085} + \left(\frac{2.085}{E_0}\right)^3 I_{5,b}^{W, 2.085} \quad (\text{F.11})$$

where $I_i^{(D,W), 2.085}$ are constants, computed at the fixed energy of 2.085 GeV to simplify calculations. In order to accurately portray machine conditions (such that $\eta_b \neq 0$), the model lattice used for determining the constants was fit to machine data from 2.085 GeV low-emittance conditions. The computed constants are summarized in Table F.1.

Integral	D-Term	W-Term
$I_2^{2.085}$	9.5943×10^{-2}	6.1510×10^{-1}
$I_3^{2.085}$	1.7896×10^{-3}	1.4545×10^{-1}
$I_{4,b}^{2.085}$	-3.9491×10^{-4}	-8.6640×10^{-4}
$I_{5,b}^{2.085}$	8.0589×10^{-9}	5.3791×10^{-7}

Table F.1: Contributions from dipoles and damping wigglers to the radiation integrals for model CesrTA lattice at 2.085 GeV which has been fit to machine data. Recall that the “D” term includes all non-wiggler contributions.

In order to verify the model for energy dependence of the radiation integrals on beam energy, the integrals can be computed exactly using `Bmad` for lattices at

the three energies where measurements were made. Once again, the model lattices were fit to data such that the $I_{4,b}$ and $I_{5,b}$ terms were nonzero. These “exact” values are then compared with approximate “scaled” values as determined by the energy scaling discussed here, and using the values in Table F.1. The results of this comparison are summarized in Table F.2.

Integral	Method	2.085 GeV	2.3 GeV	2.5 GeV
I_2	Exact	7.1104×10^{-1}	6.0136×10^{-1}	5.2375×10^{-1}
	Scaled	7.1104×10^{-1}	6.01421×10^{-1}	5.23779×10^{-1}
	Δ [%]	0%	-0.01%	-0.005%
I_3	Exact	1.4724×10^{-1}	1.1015×10^{-1}	8.6180×10^{-2}
	Scaled	1.4724×10^{-1}	1.10144×10^{-1}	8.61642×10^{-2}
	Δ [%]	0%	0.005%	0.02%
$I_{4,b}$	Exact	-1.2613×10^{-3}	-6.2666×10^{-4}	-4.4388×10^{-4}
	Scaled	-1.2613×10^{-3}	-11.069×10^{-4}	9.9754×10^{-4}
	Δ [%]	0%	-76.6%	-124.7%
$I_{5,b}$	Exact	5.4596×10^{-7}	1.3347×10^{-7}	4.1395×10^{-8}
	Scaled	5.4596×10^{-7}	4.08782×10^{-7}	3.20097×10^{-7}
	Δ [%]	0%	-206.3%	-673.3%

Table F.2: Evaluation of the accuracy of the model for energy-dependence of the radiation integrals.

The discrepancies in $I_{4,b}$ and $I_{5,b}$ imply that the differences in the corrections applied at each energy are nontrivial. However, these terms will depend strongly on the specific set of corrections in the machine, therefore the discrepancy is not surprising, and should not affect the resulting energy dependence argument.

F.2 Contributions to the Emittance

The vertical emittance is assumed to have contributions from three sources: from the finite opening angle of radiation (OA); from misalignments and errors, where the emittance growth arises from quantum excitation (QE); and from time-varying sources (TV), such as modulating power supplies and voltage jitter from the RF system. Starting from the statement of the emittance in Eqn. 2.93:

$$\left. \frac{d\epsilon_b}{dt} \right|_{damping} + \left. \frac{d\epsilon_b}{dt} \right|_{OA} + \left. \frac{d\epsilon_b}{dt} \right|_{QE} + \sum_i \left. \frac{d\epsilon_b}{dt} \right|_{TV,i} = 0 \quad (\text{F.12})$$

Recall that the damping term has the form:

$$\left. \frac{d\epsilon_b}{dt} \right|_{damping} = -2\alpha_b \epsilon_b \quad (\text{F.13})$$

The equilibrium emittance is therefore:

$$\epsilon_b = \frac{1}{2\alpha_b} \left(\left. \frac{d\epsilon_b}{dt} \right|_{OA} + \left. \frac{d\epsilon_b}{dt} \right|_{QE} + \left. \frac{d\epsilon_b}{dt} \right|_{RF} + \left. \frac{d\epsilon_b}{dt} \right|_{\theta,s} + \left. \frac{d\epsilon_b}{dt} \right|_{\theta,c} \right) \quad (\text{F.14})$$

$$= \epsilon_b^{OA} + \epsilon_b^{QE} + \epsilon_b^{RF} + \epsilon_b^{\theta,s} + \epsilon_b^{\theta,c} \quad (\text{F.15})$$

There are two terms for time-varying dipole kicks, as the kick may scale with energy (θ, s) or remain constant (θ, c). The naming convention is slightly inconvenient: note that if a time-varying dipole kick arises from a power supply whose current jitter scales with energy, the resulting kick itself will remain constant with energy.

The individual terms in this sum are now derived. The results are in Eqns. F.30, F.36, F.40, and F.44.

F.3 Energy Dependence of α_b

The damping decrement α_b is defined to be:

$$\alpha_b = \frac{U_0}{2E_0T_0} J_b \quad (\text{F.16})$$

$$U_0 = \frac{C_\gamma E^4}{2\pi} I_2 \quad (\text{F.17})$$

$$J_b = 1 - \frac{I_{4b}}{I_2} \quad (\text{F.18})$$

$$C_\gamma = \frac{4\pi}{3} \frac{r_e}{(m_e c^2)^3} \quad (\text{F.19})$$

Note from Table F.1 that $I_{4,b}/I_2 \ll 1$, therefore $J_b \approx 1$, and the energy dependence of J_b may be neglected for this study.

Recall that the dipole and wiggler contributions to the radiation integrals are separable. Therefore:

$$\alpha_b = \frac{C_\gamma E^4}{2\pi} \frac{(I_2^D + I_2^W)}{2E_0T_0} J_b \quad (\text{F.20})$$

This term will be common among all three contributions to the equilibrium vertical emittance.

F.4 “Opening Angle” Term

In practice, $\epsilon_b|_{OA}$ only varies from 0.22 pm to 0.18 pm when the energy varies from 2.085 GeV to 2.553 GeV. This term is therefore treated as a constant of value $\epsilon_b|_{OA} = 0.2$ pm. The derivation of the energy dependence of this term is shown here for completeness.

From Eqn. 2.66:

$$\left. \frac{d\epsilon_b}{dt} \right|_{OA} = \frac{\langle \mathcal{N} \langle u^2 \rangle \beta_b \rangle}{4\gamma^2 E_0^2} \quad (\text{F.21})$$

where $\langle u^2 \rangle$ is the mean square energy per photon emitted, and \mathcal{N} is the average photon emission rate around the entire lattice (in units of γ/s). In further detail:

$$\mathcal{N} \langle u^2 \rangle = \frac{55}{24\sqrt{3}} P_\gamma \hbar \omega_c \quad (\text{F.22})$$

$$P_\gamma = \frac{2}{3} r_e m c^2 \frac{c \beta^4 \gamma^4}{\rho^2} \quad (\text{F.23})$$

$$\omega_c = \frac{3}{2} \frac{c \gamma^3}{\rho} \quad (\text{F.24})$$

with P_γ the power emitted, ω_c the critical frequency of emitted radiation, and ρ the bending radius.

Fleshing out Eqn. F.21:

$$\left. \frac{d\epsilon_b}{dt} \right|_{OA} = \frac{\left\langle \left(\frac{55}{24\sqrt{3}} P_\gamma \hbar \omega_c \right) \beta_b \right\rangle}{4\gamma^2 E_0^2} \quad (\text{F.25})$$

$$= \frac{\left\langle \left(\frac{55}{24\sqrt{3}} \left(\frac{2}{3} r_e m c^2 \frac{c\beta^4\gamma^4}{\rho^2} \right) \hbar \left(\frac{3}{2} \frac{c\gamma^3}{\rho} \right) \right) \beta_b \right\rangle}{4\gamma^2 E_0^2} \quad (\text{F.26})$$

$$= \frac{55}{96\sqrt{3}} \frac{r_e \hbar c^2 \beta^4 \gamma^3}{m c^2} \left\langle \frac{1}{\rho^3} \beta_b \right\rangle \quad (\text{F.27})$$

Combining with Eqn. F.20 to determine the contribution to the emittance:

$$\epsilon_b|_{OA} = \frac{1}{2\alpha_b} \left. \frac{d\epsilon_b}{dt} \right|_{OA} \quad (\text{F.28})$$

$$= \frac{1}{2} \left(\frac{2\pi}{C_\gamma E^4} \frac{2E_0 T_0}{(I_2^D + I_2^W)} \frac{1}{\left(1 - \frac{(I_{4b}^D + I_{4b}^W)}{(I_2^D + I_2^W)} \right)} \right) \times \left(\frac{55}{96\sqrt{3}} \frac{r_e \hbar c^2 \beta^4 \gamma^3}{m c^2} \left\langle \frac{1}{\rho^3} \beta_b \right\rangle \right) \quad (\text{F.29})$$

After simplification, and assuming $\beta \approx 1$:

$$\epsilon_b|_{OA} = C_q \frac{(I_3^D + I_3^W) \langle \beta_b \rangle}{(I_2^D + I_2^W) J_b} \quad (\text{F.30})$$

where the dependence of wiggler radiation integrals I_i^W is discussed in Sec. F.1.

F.5 “Quantum Excitation” Term

From Eqn. 2.65:

$$\left. \frac{d\epsilon_v}{dt} \right|_{QE} = \frac{\langle \mathcal{N} \langle u^2 \rangle \mathcal{H}_b \rangle}{2E_0} \quad (\text{F.31})$$

The derivation is therefore similar to that for the “opening angle” term:

$$\left. \frac{d\epsilon_b}{dt} \right|_{QE} = \frac{\left\langle \left(\frac{55}{24\sqrt{3}} \left(\frac{2}{3} r_e m c^2 \frac{\beta^4 \gamma^4}{\rho^2} \right) \hbar \left(\frac{3}{2} \frac{c\gamma^3}{\rho} \right) \right) \mathcal{H}_b \right\rangle}{2E_0} \quad (\text{F.32})$$

$$= \frac{55}{48\sqrt{3}} \hbar r_e c^2 \beta^4 \gamma^6 \left\langle \frac{\mathcal{H}_b}{\rho^3} \right\rangle \quad (\text{F.33})$$

Computing the contribution to the vertical emittance:

$$\epsilon_b|_{QE} = \frac{1}{2\alpha_b} \left. \frac{d\epsilon_b}{dt} \right|_{QE} \quad (\text{F.34})$$

$$= \frac{1}{2} \left(\frac{2\pi}{C_\gamma E^4} \frac{2E_0 T_0}{(I_2^D + I_2^W)} \frac{1}{\left(1 - \frac{(I_{4b}^D + I_{4b}^W)}{(I_2^D + I_2^W)} \right)} \right) \times \frac{55}{48\sqrt{3}} \hbar r_e c^2 \beta^4 \gamma^6 \left\langle \frac{\mathcal{H}_b}{\rho^3} \right\rangle \quad (\text{F.35})$$

Again, after some simplification:

$$\epsilon_b|_{QE} = C_q \frac{\gamma^2}{J_b} \frac{I_{5,b}^D + I_{5,b}^W}{I_2^D + I_2^W} \quad (\text{F.36})$$

where again the dependence of the radiation integrals is shown in Sec. F.1.

F.6 “Time-Varying” Terms

The two classes of time-varying sources considered are RF voltage jitter and dipole kicks which vary turn-by-turn.

F.6.1 RF Voltage Jitter

The emittance growth from voltage jitter in the RF is given by Eqn. 2.96, reprinted here:

$$\left. \frac{d\epsilon_b}{dt} \right|_{RF} = \frac{1}{2} f_0 \langle \mathcal{H}_b \rangle \frac{e^2 V_{RMS}^2}{E_0^2} \quad (\text{F.37})$$

This produces a contribution to the vertical emittance:

$$\epsilon_b^{RF} = \frac{1}{2\alpha_b} \left. \frac{d\epsilon_b}{dt} \right|_{RF} \quad (\text{F.38})$$

$$= \frac{1}{2} \left(\frac{2\pi}{C_\gamma E^4} \frac{2E_0 T_0}{(I_2^D + I_2^W)} \frac{1}{J_b} \right) \times \left(\frac{1}{2} f_0 \langle \mathcal{H} \rangle \frac{e^2 V_{RMS}^2}{E_0^2} \right) \quad (\text{F.39})$$

$$= \frac{\pi e^2}{C_\gamma} \frac{1}{E^5} \frac{\langle \mathcal{H} \rangle V_{RMS}^2}{(I_2^D + I_2^W) J_b} \quad (\text{F.40})$$

Since the cavity voltage is independent of energy, the amplitude of voltage jitter will remain constant as well.

F.6.2 Time-Varying Dipole Kick

The emittance growth rate for a time-varying dipole kick is given by Eqn. 2.95, reprinted here:

$$\left. \frac{d\epsilon_b}{dt} \right|_\theta = \frac{1}{2} f_0 \beta_b \theta_{RMS}^2 \quad (\text{F.41})$$

Once again following the same procedure as the previous three scenarios, the contribution to the vertical emittance is:

$$\epsilon_b^\theta = \frac{1}{2\alpha_b} \left. \frac{d\epsilon_b}{dt} \right|_\theta \quad (\text{F.42})$$

$$= \frac{1}{2} \left(\frac{2\pi}{C_\gamma E^4} \frac{2E_0 T_0}{(I_2^D + I_2^W)} \frac{1}{J_b} \right) \times \frac{1}{2} f_0 \beta_b \theta_{RMS}^2 \quad (\text{F.43})$$

$$= \frac{\pi \beta_b}{C_\gamma} \frac{1}{E^3} \frac{\theta_{RMS}^2}{(I_2^D + I_2^W) J_b} \quad (\text{F.44})$$

There are two possibilities for energy dependence, depending on the source of the kick. If the kick arises from current jitter in a magnet power supply, the amplitude of current jitter will increase proportionally with energy, $\theta_{RMS} \propto I/E_0$ will remain constant with energy, and Eqn. F.44 properly displays all energy dependencies.

However, it is also possible that a kick may arise from an element which does not scale with energy (e.g., feedback modulator noise). For kicks of this nature there is an additional factor of $1/E_0^2$ for Eqn. F.44 to display the correct energy dependence. This yields the same energy dependence as for RF voltage jitter (Eqn. F.40), and will therefore be folded into that term when fitting machine data.

BIBLIOGRAPHY

- [1] "The International Linear Collider Technical Design Report," ILC Global Design Effort, Tech. Rep., 2013. [Online]. Available: <http://www.linearcollider.org/ILC/Publications/Technical-Design-Report>
- [2] M. A. Palmer *et al.*, "The Conversion and Operation of the Cornell Electron Storage Ring as a Test Accelerator (CesrTA) for Damping Rings Research and Development," in *Proceedings of the 2009 Particle Accelerator Conference, Vancouver, BC, 2009*, pp. 4200–4204. [Online]. Available: <http://accelconf.web.cern.ch/AccelConf/PAC2009/papers/fr1rai02.pdf>
- [3] G. F. Dugan, M. A. Palmer, and D. L. Rubin, "ILC Damping Rings R&D at CesrTA," in *ICFA Beam Dynamics Newsletter*, J. Urakawa, Ed. International Committee on Future Accelerators, Dec. 2009, no. No. 50, pp. 11–33. [Online]. Available: <http://www-bd.fnal.gov/icfabd/Newsletter50.pdf>
- [4] D. Rubin, D. Sagan, and J. Shanks, "CesrTA Layout and Optics," in *Proceedings of the 2009 Particle Accelerator Conference, Vancouver, BC, 2009*, pp. 2751–2753. [Online]. Available: <http://accelconf.web.cern.ch/AccelConf/PAC2009/papers/we6pfp103.pdf>
- [5] M. Palmer, M. Billing, G. Dugan, M. Furman, and D. Rubin, "The CESR Test Accelerator Electron Cloud Research Program Phase I Report," CLASSE, Tech. Rep., 2013. [Online]. Available: <http://www.lns.cornell.edu/public/CLNS/2012/CLNS12-2084/clns-12-2084.pdf>
- [6] J. L. Smith, R. F. Fischetti, and M. Yamamoto, "Micro-Crystallography Comes Of Age," *Current Opinion in Structural Biology*, vol. 22, no. 5, pp. 602 – 612, 2012.
- [7] Y. Ohnishi *et al.*, "Accelerator design at SuperKEKB," *Prog. Theor. Exp. Phys.*, 2013.
- [8] M. I. D. Team, "MAX IV Accelerators," MAXLAB, Tech. Rep., 2013. [Online]. Available: <https://www.maxlab.lu.se/node/206>
- [9] N.-I. D. Team, "NSLS-II Conceptual Design Report," BNL, Tech. Rep., 2006. [Online]. Available: <http://www.bnl.gov/nsls2/design.asp>
- [10] "Advanced Photon Source Upgrade Project Preliminary Design Report,"

- Argonne, Tech. Rep., 2012. [Online]. Available: http://www.aps.anl.gov/Upgrade/FlexPaper_PDR/PDR.pdf
- [11] R. Dowd, M. Boland, G. LeBlanc, and Y.-R. E. Tan, "Achievement of Ultralow Emittance Coupling in the Australian Synchrotron Storage Ring," *Phys. Rev. ST Accel. Beams*, vol. 14.
- [12] G. LeBlanc, M. Boland, and E. Tan, "ASP Storage Ring Beam Sizes at the Beamline Source Points," ASLS, Tech. Rep., 2003.
- [13] G. Rehm, "Achieving and Measuring Sub-Micrometer Beam Stability at 3rd Generation Light Sources," in *Proceedings of the 11th International Conference on Synch. Rad. Instr.*, 2013.
- [14] M. Aiba, M. Boge, N. Milas, and A. Streun, "Ultra low vertical emittance at SLS through systematic and random optimization," *Nucl. Instrum. Methods Phys. Res. A*, vol. 694.
- [15] G. Hoffstaetter, S. Gruner, and M. Tigner, "Cornell Energy Recovery Linac Project Definition Design Report," CLASSE, Tech. Rep., 2012. [Online]. Available: <http://erl.chess.cornell.edu/PDDR/PDDR.pdf>
- [16] "LHC Design Report," CERN, Tech. Rep., 2004.
- [17] H. Wiedemann, *Particle Accelerator Physics*, 3rd ed. Springer, 2007.
- [18] S. Lee, *Accelerator Physics*, 2nd ed. World Scientific, 2007.
- [19] A. Chao and M. Tigner, Eds., *Handbook of Accelerator Physics and Engineering*, 1st ed. World Scientific, 1999.
- [20] M. Palmer, "Low-Emittance Ring Design," in *Fifth International Accelerator School for Linear Colliders*, 2010.
- [21] D. Sagan and D. Rubin, "Linear Analysis of Coupled Lattices," *Phys. Rev. ST Accel. Beams*, vol. 2, Jul. 1999.
- [22] D. Sagan, "The Bmad Reference Manual," CLASSE, Tech. Rep., 2013. [Online]. Available: <http://www.lepp.cornell.edu/~dcs/bmad/>
- [23] J. A. Crittenden, A. Mikhailichenko, and A. Temnykh, "Design Considerations for the CESR-c Wiggler Magnets," in *Proceedings of the*

2003 Particle Accelerator Conference, Portland, OR, J. Chew, P. Lucas, and S. Webber, Eds., 2003, pp. 1954–1956. [Online]. Available: <http://accelconf.web.cern.ch/AccelConf/p03/PAPERS/WPAE009.PDF>

- [24] M. Palmer, “CESR-c Wiggler Experience,” in *Second ILC Accelerator Workshop*, 2005.
- [25] S. Temnykh, “Wiggler Optimization for Emittance Control: Experience at CESR-c,” in *WIGGLE 05 Workshop*, 2005.
- [26] J. R. Calvey, J. Makita, M. A. Palmer, R. M. Schwartz, C. R. Strohman, S. Calatroni, G. Rumolo, K. Kanazawa, Y. Suetsugu, M. Pivi, and L. Wang, “Electron Cloud Mitigation Investigations at CESR-TA,” in *Proceedings of ECLLOUD 2010: 49th ICFA Advanced Beam Dynamics Workshop on Electron Cloud Physics*, Ithaca, NY, K. Smolenski, Ed., no. Paper MIT01, in press.
- [27] M. Ehrlichman, “Normal Mode Analysis of Single Bunch, Charge Density Dependent Behavior in Electron/Positron Beams,” Ph.D. dissertation, Cornell University, Ithaca, New York, May 2013.
- [28] M. A. Palmer *et al.*, “CESR Beam Position Monitor System Upgrade for CesrTA and CHESS Operations,” in *Proceedings of the 2010 International Particle Accelerator Conference, Kyoto, Japan, 2010*, pp. 1191–1193. [Online]. Available: <http://accelconf.web.cern.ch/AccelConf/IPAC10/papers/mope089.pdf>
- [29] R. E. Meller and M. A. Palmer, “Digital Tune Tracker for CESR,” in *Proceedings of the 2011 Particle Accelerator Conference, New York, NY, 2011*, pp. 504–506. [Online]. Available: <http://accelconf.web.cern.ch/AccelConf/PAC2011/papers/mop215.pdf>
- [30] N. T. Rider, J. P. Alexander, J. A. Dobbins, M. G. Billing, R. E. Meller, M. A. Palmer, D. P. Peterson, C. R. Strohman, and J. W. Flanagan, “Development of an X-Ray Beam Size Monitor with Single Pass Measurement Capability for CesrTA,” in *Proceedings of the 2011 Particle Accelerator Conference, New York, NY, 2011*, pp. 687–689. [Online]. Available: <http://accelconf.web.cern.ch/AccelConf/PAC2011/papers/mop304.pdf>
- [31] N. T. Rider *et al.*, “Operation of a Single Pass, Bunch-by-bunch x-ray Beam Size Monitor for the CESR Test Accelerator Research Program,” in *Proceedings of IBIC 2012: International Beam Instrumentation Conference, Tsukuba, Japan*, no. Paper WECD01, in press. [Online]. Available: <http://ibic12.kek.jp/prepress/papers/wecd01.pdf>

- [32] E. Hecht, *Optics*, 4th ed. Addison-Wesley, 2001.
- [33] R. W. Helms and G. H. Hoffstaetter, "Orbit and Optics Improvement by Evaluating the Nonlinear Beam Position Monitor Response in the Cornell Electron Storage Ring," *Phys. Rev. ST Accel. Beams*, vol. 8, Jun. 2005.
- [34] D. Sagan, R. Meller, R. Littauer, and D. Rubin, "Betatron Phase and Coupling Measurements at the Cornell Electron/Positron Storage Ring," *Phys. Rev. ST Accel. Beams*, vol. 3, Sep. 2000.
- [35] D. L. Rubin *et al.*, "Beam Based Measurement of Beam Position Monitor Electrode Gains," *Phys. Rev. ST Accel. Beams*, vol. 13, Sep. 2010.
- [36] J. P. Shanks, D. Rubin, and D. Sagan, "Cesrta low emittance tuning," in *Proceedings of the 2010 International Particle Accelerator Conference, Kyoto, Japan, 2010*, pp. 4620–4622. [Online]. Available: <http://accelconf.web.cern.ch/AccelConf/IPAC10/papers/thpe046.pdf>
- [37] J. Safranek, G. Portmann, A. Terebilo, and C. Steier, "MATLAB-Based LOCO," SSRL/SLAC and LBNL, Tech. Rep., 2002. [Online]. Available: <http://www.slac.stanford.edu/cgi-wrap/getdoc/slac-pub-9464.pdf>
- [38] A. Terebilo, "Accelerator Toolbox for MATLAB," SSRL/SLAC, Tech. Rep., 2001. [Online]. Available: <http://www.slac.stanford.edu/cgi-wrap/getdoc/slac-pub-8732.pdf>
- [39] L. S. Nadolski, "LOCO Fitting Challenges and Results for SOLEIL," in *ICFA Beam Dynamics Newsletter*, A. Ghodke and W. Chou, Eds. International Committee on Future Accelerators, Dec. 2007, no. 44.
- [40] M. Spencer, "LOCO at the Australian Synchrotron," in *ICFA Beam Dynamics Newsletter*, A. Ghodke and W. Chou, Eds. International Committee on Future Accelerators, Dec. 2007, no. 44.
- [41] C. Steier, "Linear Lattice Calibration for Frequency Map Analysis and Low Emittance Tuning using Orbit Response Matrix Analysis at the ALS," in *ICFA Beam Dynamics Newsletter*, A. Ghodke and W. Chou, Eds. International Committee on Future Accelerators, Dec. 2007, no. 44.
- [42] V. Sajaev, "Transverse Impedance Distribution Measurements using the Response Matrix Fit Method at APS," in *ICFA Beam Dynamics Newsletter*,

A. Ghodke and W. Chou, Eds. International Committee on Future Accelerators, Dec. 2007, no. 44.

- [43] E. Huttel, J. Tanabe, A. Jackson, B. Barg, and G. LeBlanc, "The Storage Ring Magnets of the Australian Synchrotron," ASLS, Tech. Rep., 2004. [Online]. Available: <http://www.slac.stanford.edu/cgi-wrap/getdoc/slac-pub-11151.pdf>
- [44] W. Press, S. Teukolsky, W. Vetterling, and B. Flannery, *Numerical Recipes: The Art of Scientific Computing*, 3rd ed. Cambridge University Press, 2007.
- [45] J. Shanks *et al.*, "Status of Low Emittance Tuning at CesrTA," in *Proceedings of the 2011 Particle Accelerator Conference, New York, NY, 2011*, pp. 1540–1542. [Online]. Available: <http://accelconf.web.cern.ch/AccelConf/PAC2011/papers/wep022.pdf>
- [46] P. Bevington, *Data Reduction and Error Analysis for the Physical Sciences*, 3rd ed. McGraw-Hill, 2002.
- [47] J. P. Shanks *et al.*, "CesrTA Low-Emittance Tuning—First Results," in *Proceedings of the 2009 Particle Accelerator Conference, Vancouver, BC, 2009*, pp. 2754–2756. [Online]. Available: <http://accelconf.web.cern.ch/AccelConf/PAC2009/papers/we6pfp104.pdf>
- [48] A. Wolski, D. Rubin, D. Sagan, and J. Shanks, "Low-Emittance Tuning of Storage Rings using Normal Mode Beam Position Monitor Calibration," *Phys. Rev. ST Accel. Beams*, vol. 14, Jul. 2011.
- [49] D. Sagan, "Bmad: A Relativistic Charged Particle Simulation Library," *Nucl. Instrum. Methods Phys. Res.*, vol. A558, pp. 356–359, Mar. 2006.
- [50] K. Hirata and K. Yokoya, "Non-Gaussian Distribution of Electron Beams due to Incoherent Stochastic Processes," *Particle Accelerators*, 1992. [Online]. Available: <http://cds.cern.ch/record/1108257/files/p147.pdf>
- [51] M. Billing *et al.*, "Dependence of Vertical Beam Dynamics Influenced by Electron Clouds at CesrTA on Variations in Bunch Spacing and Vertical Chromaticity," in *Proceedings of the 2013 International Particle Accelerator Conference*. [Online]. Available: <http://accelconf.web.cern.ch/AccelConf/IPAC2013/papers/tupwa063.pdf>
- [52] M. P. Ehrlichman *et al.*, "Intrabeam Scattering Studies at CesrTA," in

Proceedings of the 2012 International Particle Accelerator Conference, New Orleans, LA, 2012, pp. 2970–2972. [Online]. Available: <http://accelconf.web.cern.ch/accelconf/IPAC2012/papers/weppr015.pdf>

- [53] S. Myers, “The LEP Collider: From Design to Approval and Commissioning,” CERN, Tech. Rep., 1990. [Online]. Available: http://sl-div.web.cern.ch/sl-div/history/lep_doc.html
- [54] J. Shanks and D. Rubin, “ILC Damping Ring Lattice Error Tolerances,” in *2012 International Workshop on Future Linear Colliders, Arlington, TX, 2012*. [Online]. Available: <https://ilcagenda.linearcollider.org/getFile.py/access?contribId=230&sessionId=22&resId=0&materialId=slides&confId=5468>
- [55] M. Korostelev and A. Wolski, “DCO4 Lattice Design for 6.4 km ILC Damping Rings,” in *Proceedings of the 2010 International Particle Accelerator Conference, Kyoto, Japan, 2010*, pp. 3575–3577. [Online]. Available: <http://accelconf.web.cern.ch/AccelConf/IPAC10/papers/wepe096.pdf>
- [56] J. A. Crittenden, A. Mikhailichenko, E. Smith, K. Smolenski, and A. Temnykh, “Field Modeling for the CESR-C Superconducting Wiggler Magnets,” in *Proceedings of the 2005 Particle Accelerator Conference, Knoxville, TN, 2005*, pp. 2336–2338.
- [57] J. A. Crittenden, M. A. Palmer, and D. L. Rubin, “Wiggler Magnet Design Development for the ILC Damping Rings,” in *Proceedings of the 2012 International Particle Accelerator Conference, New Orleans, LA, 2012*, pp. 1969–1971. [Online]. Available: <http://accelconf.web.cern.ch/accelconf/IPAC2012/papers/tuppr065.pdf>
- [58] D. Sagan, J. A. Crittenden, D. Rubin, and E. Forest, “A Magnetic Field Model for Wigglers and Undulators,” in *ICFA Beam Dynamics Newsletter*, Y. Funakoshi, Ed. International Committee on Future Accelerators, Aug. 2003, no. No. 31, pp. 48–51. [Online]. Available: <http://www-bd.fnal.gov/icfabd/Newsletter31.pdf>
- [59] Y. Cai, “Measured Multipole Errors in PEP-II and SPEAR3 Magnets,” SLAC, Tech. Rep., 2005. [Online]. Available: https://wiki.lepp.cornell.edu/ilc/pub/Public/DampingRings/MagDocs/Cai_MutipoleErrors.pdf
- [60] Grid Engine. [Online]. Available: <https://wiki.classe.cornell.edu/Computing/GridEngine>